

JAERI - M
93-174

JAERI TANDEM & V.D.G.

ANNUAL REPORT

1992

April 1, 1992 — March 31, 1993

September 1993

Department of Reactor Engineering

日 本 原 子 力 研 究 所
Japan Atomic Energy Research Institute

JAERI-Mレポートは、日本原子力研究所が不定期に公刊している研究報告書です。
入手の問合わせは、日本原子力研究所技術情報部情報資料課（〒319-11茨城県那珂郡東海村）あて、お申しこしてください。なお、このほかに財団法人原子力弘済会資料センター（〒319-11 茨城県那珂郡東海村日本原子力研究所内）で複写による実費頒布をおこなっております。

JAERI-M reports are issued irregularly.

Inquiries about availability of the reports should be addressed to Information Division
Department of Technical Information, Japan Atomic Energy Research Institute, Tokai-mura, Naka-gun, Ibaraki-ken 319-11, Japan.

©Japan Atomic Energy Research Institute, 1993

編集兼発行	日本原子力研究所
印 刷	いばらき印刷(株)

JAERI TANDEM & V.D.G.

Annual Report

1992

April 1, 1992 - March 31, 1993

Department of Reactor Engineering

Tokai Research Establishment

Japan Atomic Energy Research Institute

Tokai-mura, Naka-gun, Ibaraki-ken

(Received August 13, 1993)

This annual report describes research activities which have been performed with the JAERI tandem accelerator and the Van de Graaff accelerator from April 1, 1992 to March 31, 1993. Summary reports of 41 papers, and list of publications, personnel and cooperative researches with universities are contained.

Keywords: JAERI TANDEM, V.D.G., Atomic Physics, Solid State Physics, Radiation Effects in Materials, Nuclear Chemistry, Nuclear Physics, Neutron Physics, Progress Report

Editors : Toru Hiraoka, Satoshi Chiba, Akira Iwamoto, Yukio Kazumata,
Yuichiro Nagame, Kenji Noda, Michihiro Shibata, Nobuaki Ogino

原研タンデム，バンデグラフ加速器
1992年度年次報告

日本原子力研究所東海研究所
原子炉工学部

(1993年 8 月13日受理)

本年次報告は，原研タンデム及びバンデグラフ加速器で，1992年 4 月 1 日から1993年 3 月31までの間に東海研で行われた研究活動を取りまとめたものである。

1) 加速器運転と開発研究 2) 原子分子物理，固体物理及び材料の放射線効果 3) 核化学
4) 軽イオン核物理 5) 重イオン核物理の 5 部門にまたがる41編の研究報告，公表された文献，
関与した職員及び大学等との協力研究のリストを収録している。

東海研究所：〒319-11 茨城県那珂郡東海村白方字白根 2-4

(編集者) 平岡 徹，千葉 敏，岩本 昭，数又幸生，永目諭一郎，野田健治，柴田理尋
荻野伸明

PREFACE

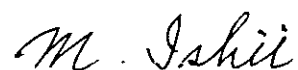
This report covers research and development activities during the period April 1, 1992 until March 31, 1993 at the 20 UR tandem accelerator facility at JAERI, Tokai.

During that period the tandem accelerator was operated over 4000 hours and supplied stable beams to experiments in the fields of : (1) Atomic Physics, Solid State Physics and Radiation Effects in Materials, (2) Nuclear Chemistry, (3) Light-Ion Nuclear Physics and (4) Heavy-Ion Nuclear Physics. Forty one research programs have been carried out by the JAERI staff and collaborators from universities and national laboratories.

The JAERI superconducting booster for the tandem accelerator is at the final stage of construction. The booster with the helium refrigerators has succeeded in the cooling and RF tests but a few superconducting resonators suffered a light "Q disease". After a minor readjustment of the resonators and others the test with ion beams from the tandem accelerator will start in October 1993.

A recoil mass spectrometer for the booster was designed which was of a type : $Q_1Q_2EMEQ_3Q_4O$. The spectrometer will be completed in the middle of 1994 and will be used for experiments at its end.

Reformation of the research divisions at JAERI has been undertaken and Department of Physics was decided to be extinct on March 31, 1993. After that the Department of Reactor Engineering will take charge of the activities at the tandem accelerator.



Mitsuhiko Ishii
Director
Department of Physics

Contents

I. ACCELERATOR OPERATION AND DEVELOPMENT	1
1.1 Tandem Accelerator Operation	3
1.2 New Control System for the JAERI Tandem Accelerator	5
1.3 Superconducting Booster	9
1.4 Off-line Tests for Superconducting Resonators of the Tandem Booster	11
II. ATOMIC PHYSICS, SOLID STATE PHYSICS AND RADIATION EFFECTS IN MATERIALS	13
2.1 Charge Exchange Cross Sections for 50 and 100 keV/amu C^{q+} ($q=1\sim5$) Ions on Neon Target	15
2.2 Binary Peak Electrons Observed at 0° for 2-4 MeV/u Si^{q+} and Ni^{q+} Ions in Collisions with He Target	19
2.3 PKA Energy Spectrum Dependence of Defect Cluster Formation in Gold by High Energy Self-ion Irradiation	23
2.4 Electrical and Structural Properties of Li-ion Irradiated β -LiAl	27
2.5 Effect of 180MeV Cu^{11+} and Br^{11+} Irradiation on Textured $Bi_2Sr_2CaCu_2O_x$	31
2.6 High Energy Au Ion Irradiation to $EuBa_2Cu_3O_x$ Thin Films	35
2.7 Effect of Au Ion Irradiation on Lattice Parameter in $EuBa_2Cu_3O_y$ Thin Film	39
2.8 Irradiation Effect on Thermal Expansion of Synthetic Single Crystal Diamond	43
2.9 X-ray Study of Strain Distribution Produced by MeV Energy Ion Implantation	47
2.10 XDT-observation of Dislocations Induced in Si Single Crystal by High Dose Irradiation of Energetic Heavy Ions	51
2.11 Photoacoustic Spectroscopic Studies on Radiation Damage of Li_4SiO_4 and $Li_{3.7}Al_{0.1}SiO_4$	55
2.12 Change of Surface Morphology in ThO_2 and $(Th,U)O_2$ Irradiated with 100 MeV Iodine Ions	59
2.13 Radiation Damage of UO_2 by 100 MeV Iodine, Nickel and Chlorine Ions	63
2.14 Elution of Injected Ions in Etched Polyimide	67
2.15 Mechanism of Single Event Effect in Power MOSFETs and CMOS ICs	71

III. NUCLEAR CHEMISTRY	75
3.1 Tests of a Gas-jet Coupled Ion Source for On-line Isotope Separator	77
3.2 Measurement of Hyperfine Structure in Radioactive Nuclide, ^{143}Pr ($T_{1/2} = 13.6 \text{ D}$), by Collinear Laser-ion-beam Spectroscopy	81
3.3 Level Scheme of ^{127}La Fed by the ^{127}Ce Decay	84
3.4 Decay Properties of ^{245}Cf	86
3.5 A Research for the Production of Transuranium Elements	89
3.6 Fast Separation of Iodine Produced from Heavy Ion-induced Fissions of Actinides	90
3.7 Fission of the $^{238}\text{U} + p$ System in the Giant Dipole Resonance Region	91
3.8 Angular Distribution of Fission Fragments in Proton-induced Fission of ^{232}Th and ^{244}Pu	93
3.9 Isotopic Distributions of Fission Products from Neutron Deficient Nuclei in Light Actinide Region	96
3.10 Fragment Mass and Kinetic Energy Distributions in Heavy Ion Induced Fission at Sub-barrier Energy Region	99
IV. LIGHT ION NUCLEAR PHYSICS	101
4.1 Measurement of Double Differential Charged-particle Emission Cross Sections for Reactions Induced by 26 MeV Protons	103
4.2 Measurement of Double-differential α -production Cross Section of Fe and Ni for 7.9 - 10.6 MeV Neutrons	107
4.3 Measurement of Neutron Activation Cross Sections at 9.1, 10.1, 11.1 and 11.8 MeV Using $^1\text{H}(^{11}\text{B},n)^{11}\text{C}$ Neutron Source at TANDEM Facility at JAERI	111
V. HEAVY ION NUCLEAR PHYSICS	115
5.1 Scattering of 115MeV ^{12}C from ^{52}Cr and ^{58}Ni	117
5.2 Observation of Airy Oscillation for the $^{16}\text{O}+^{16}\text{O}$ System at $E_{\text{lab}}=145\text{MeV}$	120
5.3 Study of ^{164}Dy with Multiple Coulomb Excitation	125
5.4 Magnetic Substate Population of Excited $^{12}\text{C}(2^+)$ Nuclei Following Resonant $^{12}\text{C}+^{16}\text{O}$ Inelastic Scattering	129
5.5 Double- γ Vibrational States in ^{168}Er and ^{192}Os	133
5.6 In-beam Study of ^{109}Sb	138

5.7	Level Position Correlations and Partial Radiative Widths for the U-238 Neutron Resonances	140
5.8	Measurements of Charged Particle Multiplicities in the Fission Process of ^{178}W	142
5.9	Light Charged Particle Identification with CsI(Tl) Scintillators for Heavy Ion and Fission Reactions	144
VI.	PUBLICATION IN JOURNALS AND PROCEEDINGS	147
VII.	PERSONNEL AND COMMITTEES	161
	(April 1992-March 1993)	
VIII.	CO-OPERATIVE RESEARCHES	167

I . ACCELERATOR OPERATION AND DEVELOPMENT

1.1 Tandem Accelerator Operation

Tandem Accelerator Group

Department of physics, JAERI

Accelerator operation

The scheduled operation for experiments was performed through the past one year containing two short periods for the scheduled maintenance. Throughout the year, the accelerator ran with no trouble. The accelerator running time was 4003.4 hours. The following are summary of the operation from April 1, 1992 to March 31, 1993. A month of the accelerator stop was scheduled for a renewal of the control computer system and miscellaneous work for the tandem booster.

1) Time distribution by terminal voltage

>16 MV	41 days	22.3 %		11-12 MV	9 days	4.9 %
15-16	69	37.5		10-11	5	2.7
14-15	9	5.0		9-10	0	0.0
13-14	29	15.8		8- 9	0	0.0
12-13	14	7.6		< 8	8	4.3

2) Time distribution by projectile

^1H	15 days	8.2 %		^{45}Sc	2 days	1.1 %
$^2\text{H}_2$	4	2.2		^{54}Fe	3	1.6
^7Li	8	4.3		^{56}Fe	3	1.6
^{11}B	4	2.2		^{58}Ni	14	7.6
^{12}C	14	7.6		^{63}Cu	6	3.3
^{16}O	46	25.0		^{74}Ge	5	2.7
^{18}O	7	3.8		^{79}Br	2	1.1
^{19}F	7	3.8		^{107}Ag	6	3.3
^{31}P	1	0.5		^{127}I	7	3.8
^{32}S	3	1.6		^{197}Au	15	8.1
^{35}Cl	9	4.9				
^{37}Cl	3	1.6				

3) Time distribution by activity

Operation for research	184 days
Atomic and solid state physics (35 days)	
Radiation effects in materials (26)	
Nuclear chemistry (39)	
Nuclear physics (64)	
Fast neutron physics (13)	
Radiation chemistry (6)	
Detector development (1)	
Voltage conditioning	4
Operation training	2
Scheduled maintenance (2 tank openings)	70
Machine time cancel due to	
experimental equipment trouble	5
Scheduled operation suspension	
for the accelerator development	30
Holidays and vacation	70

Improvement and development

Development of a new computer system for the tandem accelerator control, which utilizes parallel processing method using Transputer technology has succeeded. The new computer system was in practical use from September 1992 instead of the old computer.

The construction of the tandem booster is final stage. About 90 % of the installation and assembling work has finished. The performance test of the helium cooling systems were succeeded. The beam acceleration test will be started in the fall of 1993. Those two items will be reported in later paragraphs.

1.2 New Control System for the JAERI Tandem Accelerator

Susumu HANASHIMA, Tokio SHOZI and Katuzou HORIE

Department of Physics, JAERI

Introduction

In recent 5 years, we have been developing a new control system for the tandem accellar. The system is based on the concept of concurrent processing technology. Originally, the control system was based on a mini-computer and CAMAC serial highway system for I/O interface^{1,2)}. But, It has grown difficult to stay on the old base. One of the reasons is the difficulty in maintenance of the old-fashioned computer. Another is shortage of the computing power against the needed expansion of the system. Here we say the expansion as both expansion of functions of the control system and the expansion of the data points following enlargement of the accelerator system. To cope with the situation, we decided to construct a new control system^{3,4)}, utilizing a multi-micro-processor system and concurrent processing technology. We call the new system Accell.

In the system, we use transputers⁵⁾. The transputer is a high performance, 32-bit, micro processor which supports parallelism at the hardware level. It has communication links to other transputers. These features enable us to construct a multiprocessor system and to get large computing power easily with small costs. The performance of the control system can be extended by increasing the number of the processing elements to meet the expansion of the accelerator system.

The concurrent processing and the accelerator control

In logical terms, a control system of an accelerator is a set of various processes controlling and/or monitoring many control objects, accelerator devices. It is one of the most important role of the control system to give us an integrated environment where all of the elements of the accelerator system can be handled smoothly. However some of the activities in the system are not strongly coupled each other. In other words, the control system of an accelerator has natural concurrency. For example, a monitoring of vacuum pumping system is independent from tuning beam transport. The system can be described by a model of concurrent processes communicating with message transfer, naturally.

Data point concept

The control system is an environment to manipulate accelerator devices. From

this point of view, it is very important to formalize a method of access to the accelerator device, the accelerator data point. The system must enable the operator to select arbitrary data points and to control or monitor them smoothly. For a programmer, the access method to the data point must be generalized in a simple way, to ease programming of high level functions. Data points all have its symbolic names and they are accessed with its name and logical value of the data. The programmer need not know about CAMAC address nor raw data format of the data points.

We extended the concept of the data point to variables which have no I/O points directly. We call them virtual data points. The category includes the upper or the lower limit value for software range checking of some data point's value. It also includes control parameters for linked control of multiple data points. Many of the control functions of the accelerator can be established as manipulations of the data points.

To adapt the above philosophy to the concurrent programming system, we take a simple architecture so that a process sends a message for every data point access, one by one. Figure 1 shows an example of using virtual data points for linked control in this architecture and it's data flow scheme in the message passing system. Many data points must be tuned to change the final energy of the accelerated particle. Usually, the tuning are made by the operator one by one. The virtual data point named Ef (final energy) and its control process (Scaling rule⁶⁾ process) are introduced. The Ef has no directly associated I/O point, but the change on it is reflected to several data points

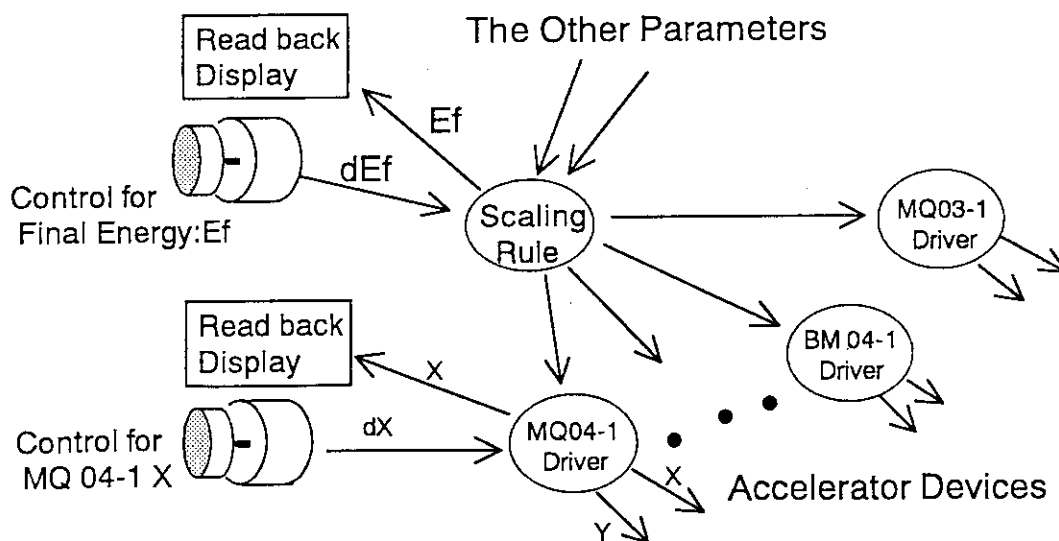


Figure 1: Control with a virtual data point, Final Energy of particle (Ef). MQ 04-1, BM04-1 and MQ03-1 are accelerator devices which affect the final energy. MQ 04-1 X is one of the data points of MQ 04-1. Control from the valuator are given as deviations from the old values of the data points.

by the scaling rule process, in a manner where beam transport of the accelerated particle is maintained and the final energy is equal to the setting value of E_f . This mechanism is applied not only to a step of the change but also to the continuous change of the virtual data point. The operator can scan the final energy, turning a dial assigned to the virtual data point E_f .

The hardware architecture of the system

The new system is divided into 1) a host system using a workstation, 2) the central

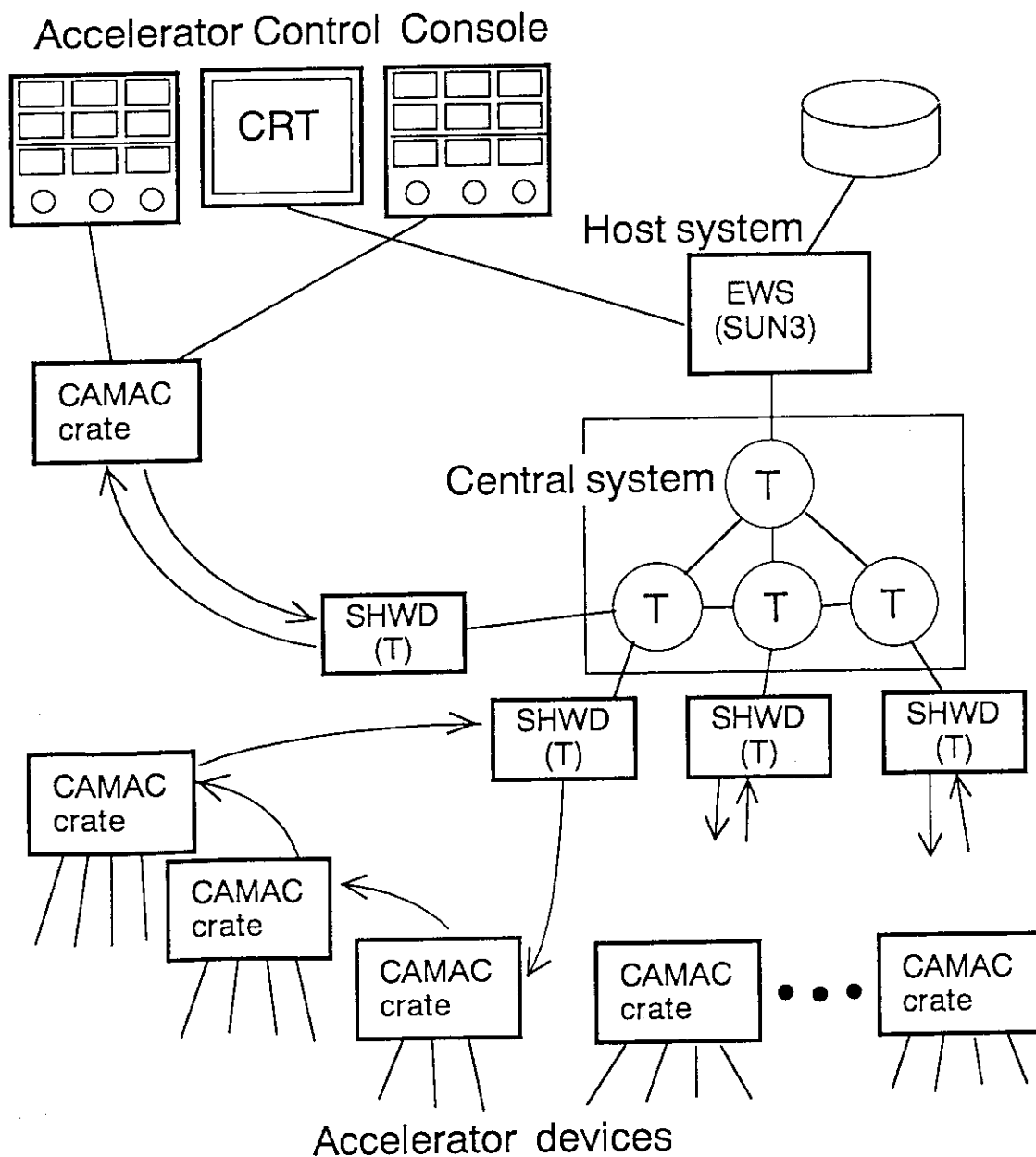


Figure 2: Image Sketch of the New Control System.

system, 3) the serial high way drivers and 4) CAMAC serial highway system. Figure 2 shows an image sketch of the system. The main roles of the host system are to support execution of the central system and to work as a part of man-machine interface. Data needed to control the accelerator are extracted from a data base on the host system and sent to the central system at start up time. A bit map display of the host is embedded in the operator console of the accelerator. A X-window⁷⁾ based program is used on the display. The central system is a multiprocessor (of four T800⁵⁾ transputers with 1Mbyte local memory now). It works as a main element of data processing. The serial highway drivers are front end processors of the central system to CAMAC system. They have charge of low level control of the CAMAC serial highway. They also do several kinds of event detection and data format conversion to make the load of the central system light. The CAMAC serial highway system is almost the same as the old system. Sixteen CAMAC crates are distributed on the 4 serial highways. Two of them on a highway are for the control console. The control console has assignable valuator (we call them shaft encoders), assignable and dedicated meters etc. for controlling and monitoring data points.

Experience of the system operation

The system has been working from September 1992. The reliability of the system has been good enough. On the other hand, the system doesn't achieve the level of performance which we have desired. The reason is mainly due to performance of the message transfer between application processes. Messages between processes are relayed by special system processes, called monitors. In our analysis, it appears that the poor throughputs of the monitors are degrading the performance of the system. And we are working on improving the monitor.

References

- 1) IEEE Inc., Modular Instrumentation and Digital Interface System (CAMAC), IEEE Std 583-1975.
- 2) IEEE Inc., Serial Highway System (CAMAC), IEEE std 595-1976.
- 3) S. Hanashima: Proceedings of the First Workshop on Control Systems, KEK Report 87-25 (1988) pp. 104-105.
- 4) S. Hanashima etc.: Proceedings of the International Conference on Accelerator and Large experimental Physics Control Systems, KEK Proceedings 92-15 (1992) pp. 333-335.
- 5) INMOS Limited: The Transputer Data book 2nd Edition, Prentice Hall Inc. (1989).
- 6) S. Hanashima and E. Minehara: Rev. Sci. Instrum. 57(5) (1986) pp. 787-788.
- 7) O. Jones: Introduction to the X Window System, Prentice Hall Inc. (1989).

1.3 Superconducting Booster

Booster Project Group

Department of Physics

1. Summary

The project of the Tandem-Booster entered the final stage of its construction in the fiscal year of 1992. By the end of the last fiscal year, four linac units, a buncher unit, a sub-buncher unit, a de-buncher unit and two refrigerators had been installed. In this fiscal year, the rest six linac units were set on the linac line. The liquid helium transfer lines with valve boxes were installed and connected to all the units. The performance test of the refrigeration system was carried out in August. After the system was accepted by JAERI, the 24 superconducting resonators in the six units were once disassembled, given final surface treatments and reassembled with tuners, input couplers, thermometers and so on. Installing various components, such as beam line components, safety interlock systems, resonator control modules, rf power amplifiers, rf cables, control cables and others started at the end of the fiscal year.

2. Resonators and cryostats

Twenty-four resonators were temporarily assembled into six cryostats (No.5 to No. 10 units) in April without surface treatments, tuners or couplers in order to pave the way for the completion and performance tests of the refrigeration system. After the performance tests were finished, the resonators were taken out of the cryostats, given by final surface treatments, reassembled in their cryostats, equipped with tuners, couplers, pick-up probes and thermometers and tuned in frequency. At least one out of four resonators of each unit was given an off-line cryogenic test and had a comfortable performance. The work was accomplished in January and followed by wiring the cryostats and the rf control units with rf cables and control cables.

3. Helium Refrigeration Systems

The liquid helium transfer lines with the valve boxes were installed in June so that the refrigerators and the cryostats were connected to form closed loops. The refrigeration systems with cryostats and resonators were inspected by the prefectural government and approved on 23rd of July as a refrigerator under the refrigerator security regulations in the high pressure gas law.

The performance test of the refrigerators without cryostats was done first in August. The two refrigerators A and B were found to have refrigeration power of 273 watts and 277 watts for the liquid helium loops, respectively and 1,580 watts and

1,563 watts for the 80K gas loops, respectively, so that the specification for the refrigerators was confirmed.

The performance test with the cryostats was carried out second in August. It took about 48 hours for both systems to cool down the radiation shields and the resonators from the room temperature to the beginning of transferring liquid helium into a cryostat liquid vessel and 12 - 15 hours to fill all the vessels. Sequence of filling was not predictable because of parallel liquid feeding. Several parameters in the automatic control program were adjusted to make the systems work stable. The both systems were tested with turning on and off a heat load of 80 watts into the liquid vessels and 200 watts into the radiation shields. They were stable against it. The performance tests finished satisfactorily at the very beginning of September.

Some minor problems were found in the tests, such as bad transfer tubes between valve boxes and cryostats. They were fixed in the next several months. We decided to equip all the transfer tubes with flexible vacuum tubes to keep pumping together with the valve boxes and transfer lines in order to improve heat insulation.

4. Others

Two quadrupole triplet lenses, an analyzing magnet with a mass energy product of 400 and beam line stands for beam diagnostic components, vacuum pumps and vacuum tubes were installed.

Radiation monitors were installed in the accelerator room, the target room and the rf (local control) room. An x-ray protection fence was placed between the accelerator room and the target room in order to prevent a man from entering the accelerator room when any resonators are turned on.

The installation and use of the booster was registered to the Mito Labor Standard Supervisory Office in prior to the resonator rf tests. An application form to the Science and Technology Agency was prepared for use of a radioactive-ray generator.

5. Schedule to the first beam

We run the refrigerators to get skilled in operating them with the help of manufacturer's engineers, first. Then, we check the resonators on line. As we repeat operating the refrigerators, we intend to improve the cooldown rate between 130K and 90K from -10K/h , which was obtained at the performance test, toward -20K/h by optimizing the control parameters of the refrigeration system, because the cooldown rate is very critical against degradation of resonator Q-factors. The booster will be completed by the fall of 1993 by finishing the beam line and its control system. We will, then, start a series of beam acceleration tests.

1.4 Off-line Tests for Superconducting Resonators of the Tandem Booster

Michihiro SHIBATA, Tetsuro ISHII and Suehiro TAKEUCHI

Accelerators Division, Japan Atomic Energy Research Institute

The tandem booster linac consists of 44 superconducting quarter wave resonators with resonant frequency of 130 MHz. The 20 resonators had been already made off-line tests, assembled in cryostats and set on the beam line.¹⁾ We made final surface treatments for newly delivered 24 resonators and made off-line tests for eight of them at a temperature of 4.2 K.

The surfaces of resonators were electropolished about 10 μm . In this time, in order to decrease hydrogen absorption into Nb metal, bubbling of nitrogen gas was adopted in electropolishing. They were rinsed with 15% HF and were cleaned by ultrasonic power with 10% H_2O_2 for about 30 minutes and with de-ionized water of 18 M $\Omega\cdot\text{cm}$ for about 60 minutes. In a clean room, they were rinsed with de-ionized water and methanol, and dried at a temperature of 35–40°C.

In off-line tests, the resonators were set in a cryostat for off-line test. While the cryostat was evacuated, they were baked at a temperature around 70°C for a few days. Then they were cooled down as fast as possible, particularly, around a temperature of 120 K, in order to avoid a Q-degradation.²⁾ It takes about 5 hours from room temperature to 4.2 K. Multipactoring barriers at low electric fields were removed in about one hour by cw conditioning with an rf amplifier of 100 W.

Typical Q - E_{acc} curves obtained from the off-line tests are shown in Fig.1, where E_{acc} indicates the accelerating electric field gradient. The Q value for most of resonators at low fields were over 1.0×10^9 . A maximum field level of 12.7 MV/m was obtained. Some resonators needed high power pulse conditioning to reach the maximum field levels, but, did not need helium processing.

In Fig.2(a) and 2(b), the distributions of maximum field levels and E_{acc} at an rf input of 4 W are shown, respectively including the 20 resonators which had been already reported last year. The $E_{\text{acc}}(P_{\text{in}}=4\text{W})$ values of eight resonators exceed the design value of 5.0 MV/m. The Q values and the $E_{\text{acc}}(P_{\text{in}}=4\text{W})$ values are higher than those of 20 resonators. The averaged value of $E_{\text{acc}}(P_{\text{in}}=4\text{W})$ is about 7.0 MV/m. It means that the total accelerating voltage of the linac is over 40 MV.

References

1. S.Takeuchi, T.Ishii, B.J.Min, and M.Shibata, Proc. of 5th Workshop on RF superconductivity 1991, Hamburg.
2. B.Aune, B.Bonin, J.M.Cavedon, M.Juillard, A.Godin, C.Henriot, Ph.Leconte, H.Safa, A.Veyssi re and C.Zylberajch, Proc. of 1990 Linear Acc. Conf. Albuquerque.

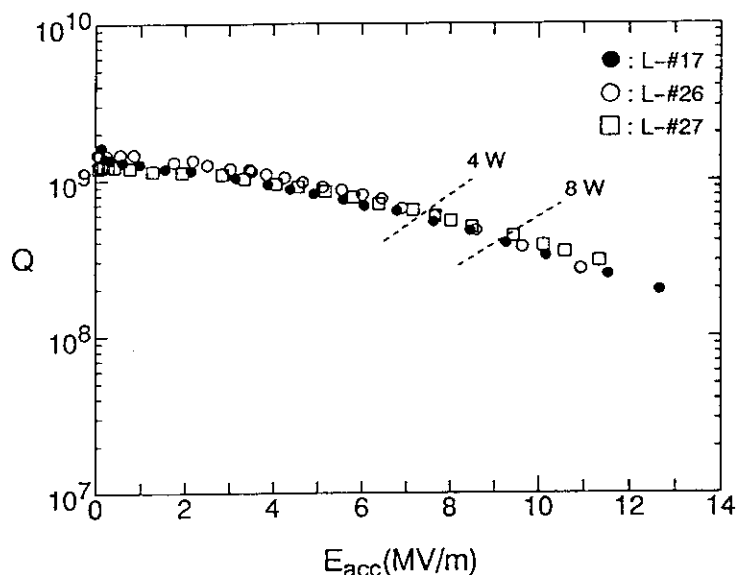


Fig.1 Q - E_{acc} curves for quarter wave resonators of nos.17, 26 and 27.

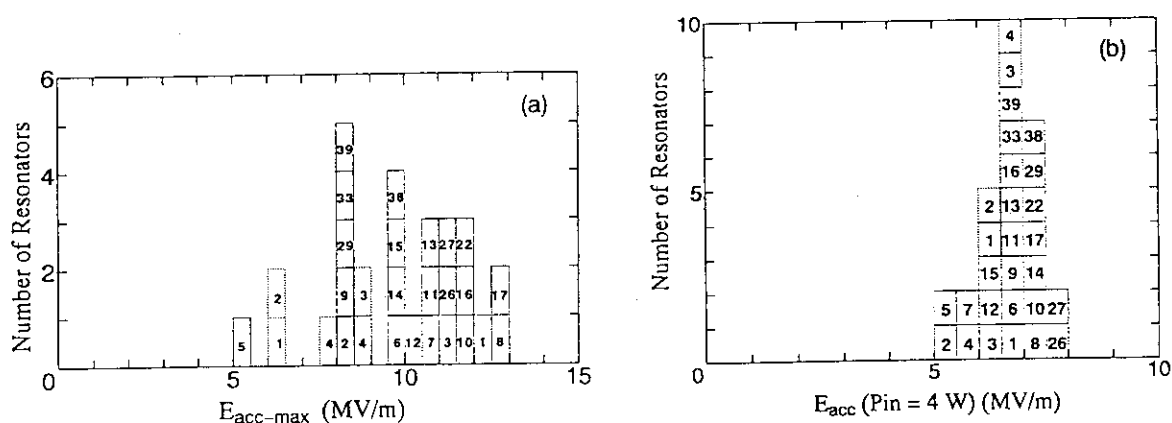


Fig.2 Resonator performances at 4.2 K.

(a) Maximum electric field levels. (b) Accelerating field levels at an rf input of 4 W. Numbers in the counts are resonator identification numbers. Resonators enclosed with dotted lines are those for the number of the buncher and de-buncher.

II. ATOMIC PHYSICS, SOLID STATE PHYSICS AND RADIATION EFFECTS IN MATERIALS

2.1 Charge Exchange Cross Sections for 50 and 100 keV/amu C^{q+} ($q=1\sim5$) Ions on Neon Target

Makoto IMAI and Masao SATAKA

Department of Physics, JAERI

Introduction

Charge exchange phenomenon is one of the most essential features in atomic collision physics field and forms bases for various fields such as plasma physics, astrophysics, radiation damage, accelerator technology and so on. Many notable works have been made, but it still does not seem we can finish studying the phenomenon, particularly in very low collision energy region and for highly charged ions. For carbon ion collisions, a few data are available for collisions with H, H_2 and He targets, and datum for collisions with targets that have more electrons is scarce especially for highly charged projectiles.

It is known that when energetic projectile penetrates through target material, its charge state is changed statistically via electron capture and loss processes until it reaches equilibrium. The mean value of the equilibrium charge state distribution varies with collision energy and target material. It is not simply a result of the collision energy and the binding energy of target electrons but electrons that participate in the collision play a distinctive role. In the present work, absolute charge exchange cross sections for C^{q+} ($q=1\sim5$) projectiles on Neon target were measured at energies of 50 and 100keV/amu and the mean charges for each projectile energy were derived. Because the velocities of 2s and 2p electrons of neon atom are just around the velocities of 100keV/amu and 50keV/amu carbon ion, respectively, it makes a good test of an effect of velocity-matching for highly charged heavy ions.

Experiment

The present experiment was performed using the 2MV VdG accelerator. A singly charged carbon ion was accelerated by the accelerator and analyzed by its energy with 90° analyzing magnet. The charge state of the incident ion was changed by a combination of a gas cell and an analyzing magnet. Projectile prepared in this manner was led to another gas cell, whose effective length was 80.1mm, filled with neon target. Collimators upstream the gas cell, the gas cell itself, and apertures downstream the gas cell were set carefully utilizing a laser beam. After the collision, projectile was deflected by an electrostatic field and detected by a solid-state detector. As the detector we used for 100keV/amu

projectiles (ORTEC position-sensitive detector; PSD) is not suitable for detecting particles below 1 MeV in energy, a set of two surface barrier detectors (SSD) was used for 50 keV/amu projectiles. The target gas pressure was kept constant automatically and was measured using MKS spinning-rotor absolute pressure gauge. Measurements were repeated varying the target gas pressure from 1×10^{-4} to 2×10^{-3} Torr to guarantee the single collision for each projectile charge state and energy. During operation of the target gas cell, vacuum chambers downstream the final bending magnet were kept below 5×10^{-8} Torr except the one that contains the gas cell, which was kept below 5×10^{-7} Torr. Effects of the charge changing collisions with residual gases before and after the collision were small enough to be regarded as a constant and cut down by least-squares fitting.

Results and discussion

Results for the present measurements are listed in table 1. The uncertainties were derived from statistical errors only. In the table 1 and in this section, charge exchange cross sections are represented in a form of σ_{if} , where i and f denote initial and final charge state, respectively.

The measured electron capture and loss cross sections respectively show descending and ascending dependence on projectile energy except for σ_{42} , which shows the reverse dependence. At each projectile energy, single electron capture cross section (ECCS) $\sigma_{i,i-1}$ ($i = 1 \sim 3$ for 50 keV/amu, $i = 1 \sim 5$ for 100 keV/amu), double ECCS $\sigma_{i,i-2}$ ($i = 2 \sim 4$ for 50 keV/amu, $i = 2 \sim 5$ for 100 keV/amu) and triple ECCS $\sigma_{i,i-3}$ ($i = 3 \sim 5$ for 100 keV/amu) decrease when initial charge state i counts down, except for σ_{42} at 100 keV/amu, which is a bit larger than σ_{53} . As for electron loss cross sections (ELCSs), single ELCS $\sigma_{i,i+1}$ ($i = 1 \sim 3$ for 50 keV/amu, $i = 1 \sim 4$ for 100 keV/amu) and double ELCS $\sigma_{i,i+2}$ ($i = 1 \sim 2$ for 50 keV/amu, $i = 1 \sim 3$ for 100 keV/amu) decrease as i counts up, except for σ_{45} at 100 keV/amu, which is larger than σ_{34} . Because both 4+ and 2+ charge states have meta-stable states with long life time and meta-stable ions generally have more reactivity than ground-state ions, these exceptions may be caused by a difference of meta-stable ions' fractions in the projectile beam.

Whenever one wants to know the equilibrium charge state distribution or the mean value of it, a complete set of charge exchange cross sections is required. As for the carbon projectile in the present energy region, 1-, 5+ and 6+ charge state components are small enough to be neglected, and cross sections σ_{if} ($i = 0 \sim 4$, $f = i - 2 \sim i + 2$; $f \neq i$) are needed to obtain the mean charge. For the present measurements, however, cross sections σ_{0f} for both projectile energy and cross section σ_{43} for 50 keV/amu projectile energy are still lacking. Neglecting 1-, 0, 4+ and higher charge state components for 50 keV/amu

case and 1-, 0 and 6+ charge state components for 100keV/amu case, we tentatively calculated the equilibrium charge state distributions for the present collision system. As we are going to present the details of the calculation elsewhere, it is not farther described here. The calculated distributions are shown in the figure and the mean values of them are tabulated in table 2. Because the neutral charge state component was neglected, the present mean charges must overestimate the real values. The differences between the real and the present mean charges are appraised to be at most 30%.

Table 1. Measured cross sections of carbon ions on neon in 10^{-16}cm^2 .

Cross section	Projectile energy	
	50keV/amu	100keV/amu
σ_{10}	0.41 ± 0.01	0.17 ± 0.01
σ_{12}	0.68 ± 0.01	0.81 ± 0.02
σ_{13}	0.019 ± 0.001	0.11 ± 0.01
σ_{20}	0.029 ± 0.002	0.015 ± 0.001
σ_{21}	1.2 ± 0.1	0.56 ± 0.01
σ_{23}	0.18 ± 0.01	0.30 ± 0.01
σ_{24}	0.00098 ± 0.00006	0.012 ± 0.001
σ_{30}	—	0.0046 ± 0.0005
σ_{31}	0.18 ± 0.01	0.13 ± 0.01
σ_{32}	2.3 ± 0.1	1.2 ± 0.1
σ_{34}	0.011 ± 0.005	0.055 ± 0.001
σ_{35}	—	0.0008 ± 0.0002
σ_{41}	0.054 ± 0.002	0.033 ± 0.001
σ_{42}	0.27 ± 0.01	0.43 ± 0.01
σ_{43}	—	1.7 ± 0.1
σ_{45}	—	0.088 ± 0.001
σ_{52}	—	0.041 ± 0.002
σ_{53}	—	0.34 ± 0.01
σ_{54}	—	2.4 ± 0.1

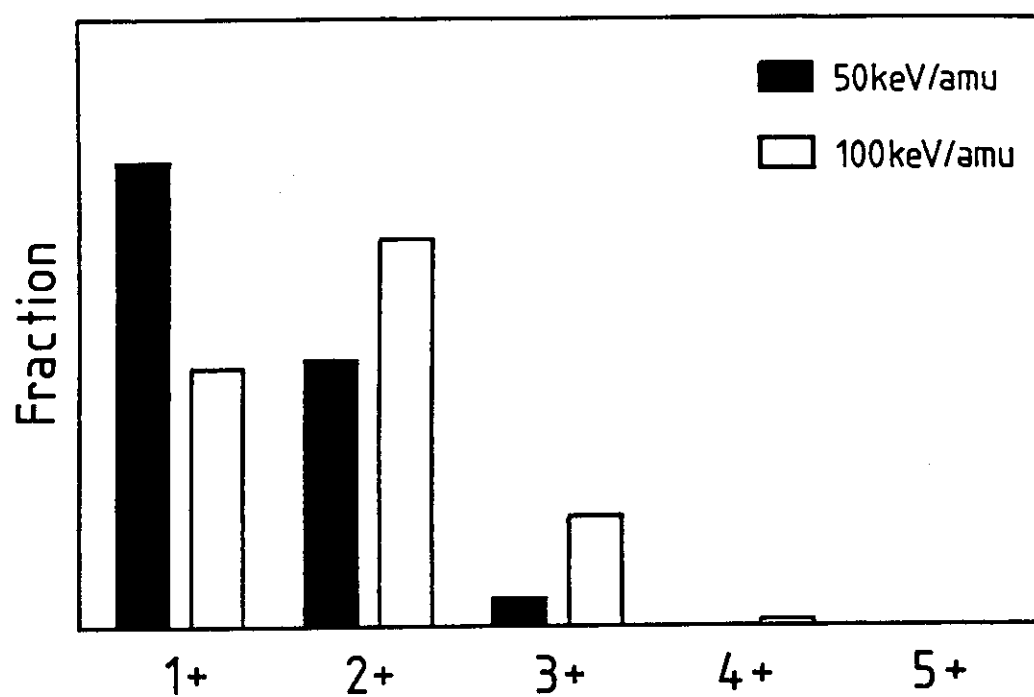


Figure. Calculated equilibrium charge state distributions for 50 and 100 keV/amu carbon ions on neon. (in linear scale)

Table 2. Mean values of the calculated equilibrium charge state distributions.

50keV/amu	100keV/amu
1.42	1.82

2.2 Binary Peak Electrons Observed at 0° for 2-4 MeV/u Si^{q+} and Ni^{q+} Ions in Collisions with He Target

Masao SATAKA, Makoto IMAI, Yasunori YAMAZAKI*,
 Ken-ichiro KOMAKI*, Kiyoshi KAWATSURA**, Yasuyuki KANAI*** and
 Hiroyuki TAWARA****

Department of Physics, JAERI, *College of Arts and Sciences,
 University of Tokyo, **Faculty of Engineering and Design,
 Kyoto Institute of Technology, ***The Institute of Physical
 and Chemical Research(RIKEN), ****National Institute for
 Fusion Science

Binary encounter (BE) electron peak is a prominent feature in electron spectra originating from collisions between fast charged particles and atoms.¹⁾

The dependence of the binary encounter peak on the projectile charge states for partially stripped ions was investigated by Richard et al. for fluorine ions with energies of 1 and 1.5 MeV/u and charge states from 3 to 9 (fully stripped).²⁾ They observed that for the partially stripped ions the cross section increased for decreasing charge state, a dependence which is in strong contrast to the behavior for fully stripped ions, where the cross section is proportional to Z_p^2 . This "surprising" charge-state dependence of the binary encounter production cross section has been treated in several theoretical papers by applying various models for electron scattering on ions³⁻⁶⁾, in which outer screening effect is thought to be important. González et al. have also experimentally confirmed the dependence for the collisions of C^{q+} , N^{q+} and O^{q+} impact on H_2 at the energy region between 0.5 and 1 MeV/u.⁷⁾

We have measured the binary encounter peaks for 0° electrons in collisions between 2 MeV/u Si^{q+} and He⁸⁾. Like the earlier measurement of Richard et al.²⁾, we have found that the binary-encounter electron production increased for decreasing the projectile charge states. We have also found that the peak energy of the binary peaks was systematically shifted from the expected value E_b with increasing the projectile charge states [9]. In the present work, measurements have been performed of zero-degree binary encounter electron spectra for 2 MeV/amu F^{q+} , 4 MeV/u Si^{q+} and Ni^{q+} ion

impacts on He. In order to study the charge state dependence of binary electron production on impact energies and Projectile Z_p , we have extended the projectile energy to higher region and made the projectile Z higher than those of the measurements of Richard et al[3] and González et al[8].

The experimental arrangement has already been described recently[10]. Projectiles Si^{6+} and Ni^{14+} were provided by the tandem accelerator at Japan Atomic Energy Research Institute. To make the charge states high, the initial ions passed through the C post stripper foil ($\sim 10 \mu\text{g}/\text{cm}^2$) and were selected by a magnet. The ejected electrons were measured by a tandem type electron spectrometer with two 45° parallel-plate electrostatic analyzers.

The binary encounter electron spectra at zero degree were measured for in the electron energy region between 5 and 12 keV. The peak height of the binary encounter spectra was derived after subtracting background spectra obtained without gas in the target cell. Figure 1 shows the ratios of the peak heights for 4 MeV/u Si^{q+} ($q=7, 11, 12$ and 13) impacts on He to that of Si^{14+} (fully stripped). The BE intensity increases as ionic charge q decreases, same as fluorine ion impact on He.

As the BE collision is just a large angle scattering of a target electron in the projectile frame, the observations are understood as follows: a collision diameter defined by Z_p/ϵ gives a kind of critical distance, inside which the incident energy of the electron no longer characterizes the collision, where Z_p is the nuclear charge of the ion and $\epsilon=(1/2)m_e v^2$ the kinetic energy of the target electron in the projectile frame. If the screening radius of the ion is smaller than the collision diameter, the collision occurs outside the ion core, and the effective charge of this collision will have positive correlation with q . On the other hand, if the screening radius is larger than the collision diameter, the effective charge for the scattering electron will be close to Z_p . In this case, the effective potential of the ion of charge state q is written,

$$V_q(r) = \frac{q}{r} + \frac{(Z_p - q)}{r} \exp\left(-\frac{r}{r_0}\right) \quad (1)$$

$$\rightarrow Z_p/r - (Z_p - q)/r_0 \quad (r \rightarrow 0) \quad (2)$$

where r_0 is the screening radius of the ion. Equation (1) shows that the energy of an electron colliding with an ion of charge state q is effectively reduced by $(Z_p - q)/r_0$ compared with that colliding with a fully stripped ion due to the potential shift. As the scattering cross section is larger for

lower impact energy, we may expect a larger cross section for lower q . Assuming the Rutherford cross section to be valid, we get,

$$I(q) \propto [\epsilon - (Z_p - q)/r_0]^{-2}, \quad (3)$$

as the intensity of BE electrons produced by an ion with charge state q . In the case of 4 MeV/u Ni^{q+} on He, the collision diameter is ~ 0.3 , which is comparable to the screening radius. Figure 2 shows the ratios of the peak heights for 4 MeV/u Ni^{q+} ($q=14, 20, 22, 24$ and 26) impacts on He to that of Ni^{25+} . The solid line in Fig.2 gives a prediction of eq.(3) assuming $\epsilon r_0 \sim 50$. Although the above discussion is fairly crude, over all features of the experiment are well reproduced. Finally, it is worth remembering that the potential shift, a key quantity to understand the q -dependence of the BE intensity, also plays an essential role in describing the Barkas effect in Stopping power[12].

References

- 1) N.Stolterfoht, *Structure and Collisions of Ions and Atoms*, Ed. I.A.Salin (Springer-Verlag, Berlin, 1978) p.155.
- 2) P.Richard, D.H.Lee, T.J.M.Zourous, and J.L.Shinpaugh, J.Phys.B23(1990)L213.
- 3) R.E.Olson, C.O.Reinhold and D.R.Schultz, J.Phys.B23(1990)L455.
- 4) C.O.Reinhold, D.R.Schultz and R.E.Olson, J.Phys.B23(1990)L591.
- 5) R.Shingal, Z.Chen, K.R.Karim, C.D.Lin and C.P.Bhalla, J.Phys.B23(1990)L637.
- 6) K.Taulbjerg, J.Phys.B24(1990)L762.
- 7) A.D.González, P.Hvelplund, A.G.Petersen and K. Taulbjerg, J.Phys.B25(1992)L57.
- 8) P.Hvelplund, H.Tawara, K.Komaki, Y.Yamazaki, K.Kuroki, H.Watanabe, K.Kawatsura, M.Sataka, M.Imai, Y.Kanai, T.Kambara and Y.Awaya, J.Phys.Soc.Jpn,60(1991)3675.
- 9) L.H.Anderson, Phys.Rev.Lett.62(1989)1731.

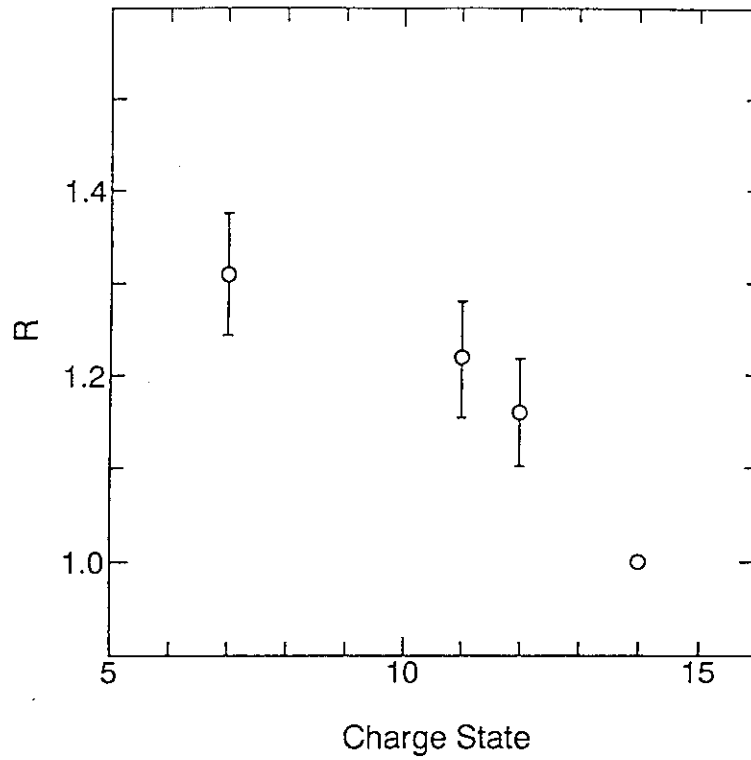


Fig. 1. Ratios of the binary encounter peak heights for 4 MeV/u Si^{q+} ($q=7,11,12$ and 13) on He to that of Si^{14+} . Estimated errors are less than 5%.

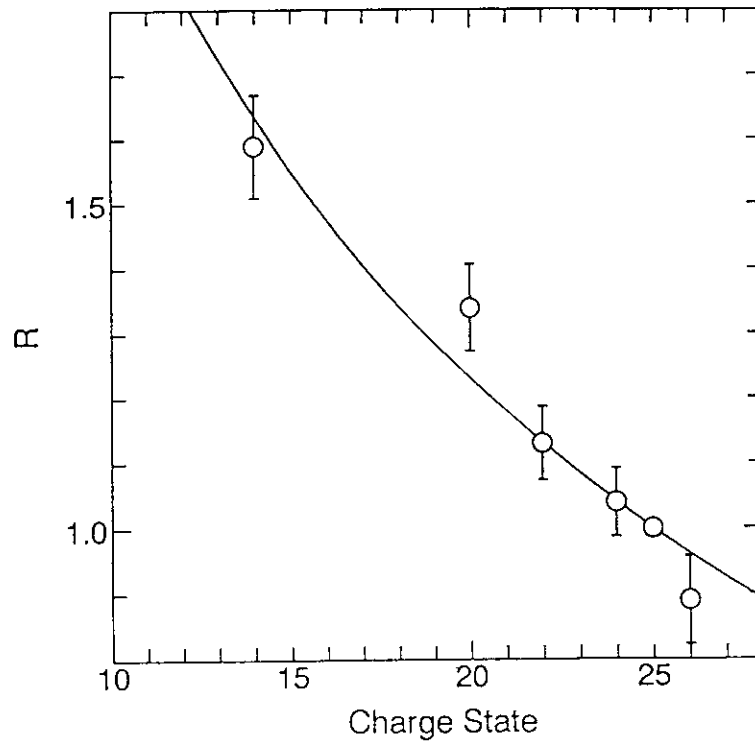


Fig. 2. Ratios of the binary encounter peak heights for 4 MeV/u Ni^{q+} ($q=14,20,22,24$ and 26) on He, which is normalized to that of Ni^{25+} . Estimated errors are less than 5%, except for $26+$ (7.5%). (Open circle: experiment, Solid line: the prediction from eq.(3).)

2.3 PKA Energy Spectrum Dependence of Defect Cluster Formation in Gold by High Energy Self-ion Irradiation

Shiori ISHINO, Naoto SEKIMURA*, Yurugi KANZAKI,
Seiji OKADA and Takahiro MASUDA

Department of Quantum Engineering and System Science,
*Nuclear Engineering Research Laboratory,
Faculty of Engineering, University of Tokyo

1. Introduction

The structure of cascade damage in metals produced by high energy particles is dependent on energy of PKA (Primary Knock-on Atoms). To establish correlations between various irradiation data, microstructural changes in irradiated materials should be analyzed based on the PKA energy spectrum¹⁻²⁾. In the present study, thin foils of gold were irradiated with 170 MeV self-ions to examine PKA energy spectrum dependence of defect cluster formation and cascade damage structure.

2. Experimental

Irradiations were carried out at room temperature using a 20 MV tandem accelerator at the Japan Atomic Energy Research Institute. By placing gold foils of 1.1, 3.0, 4.3, 6.3 and 7.2 μm in thickness in front of the TEM specimens, we can change the PKA energy spectrum in the specimens.

Figure 1 shows the PKA energy spectrum calculated by the TRIM 89 code. PKA production cross section decreases monotonically with PKA energy in all the cases. Total PKA production cross section and high energy component of PKA increase with the thickness of gold foils up to the range of 170 MeV self-ions that is 6.5 μm from the ion incident surface. Ion fluence was 1.0×10^{14} and 1.0×10^{15} ions/ m^2 to avoid cascade overlapping. Irradiated samples were observed by a 200 keV transmission electron microscope.

Irradiation experiments using a 400 keV accelerator in the University of Tokyo were also performed to compare the cascade damage structure produced by the single energy cascade damage.

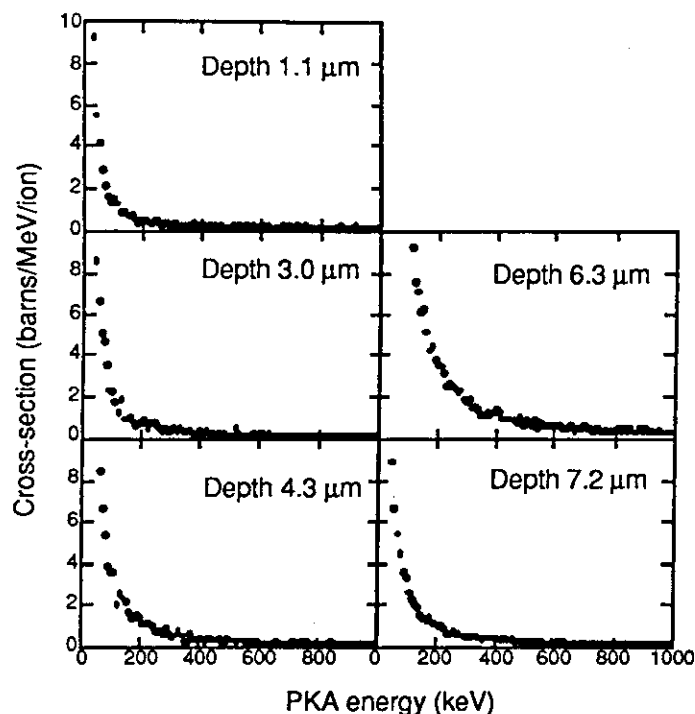


Fig. 1 Calculated PKA energy spectrum in gold irradiated with 170 MeV self-ions.

3. Results and Discussion

Groups of defect clusters which reflect subcascade structure produced by PKA are observed in the TEM foils of gold. All the clusters are found to be of vacancy type because of the high mobility of interstitials. Number of defect clusters in the group and their sizes are shown in Figures 2 and 3, respectively. In all the specimens, density of cluster groups monotonically decreases with the number of defect clusters in a group.

These results are compared with the data from 20-400 keV self-ion irradiation experiments, in which injected ions are regarded as monoenergetic PKA. Density of defect groups per incident ion is estimated as functions of number of clusters in the group and ion energy. Figure 4 shows fraction of defect groups which consist of n clusters as a function of PKA energy, E_p . Using this function, $P(n, E_p)$, and the PKA energy spectrum, $W(E_p)$, we can evaluate distribution of defect clusters under the high energy particle irradiation conditions by the following equation.

$$\int_0^{\infty} W(E_p) P(n, E_p) dE_p \quad (n=1, 2, 3, \dots)$$

Figure 5 compares measured and predicted number of clusters in a

groups. From this results, it is quantitatively shown that small fraction of high energy component of PKA affects the formation of cluster groups which have large number of clusters. A model to predict defect cluster formation under any PKA spectrum is being proposed from the extrapolation of defect cluster formation by PKA over 400 keV.

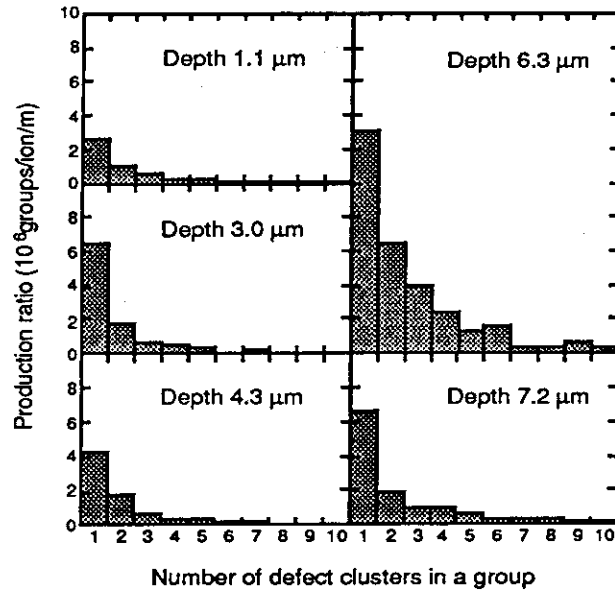


Fig. 2 Number of defect clusters in defect groups in gold irradiated with 170 MeV self-ions to 1.0×10^{14} ions/m² at room temperature.

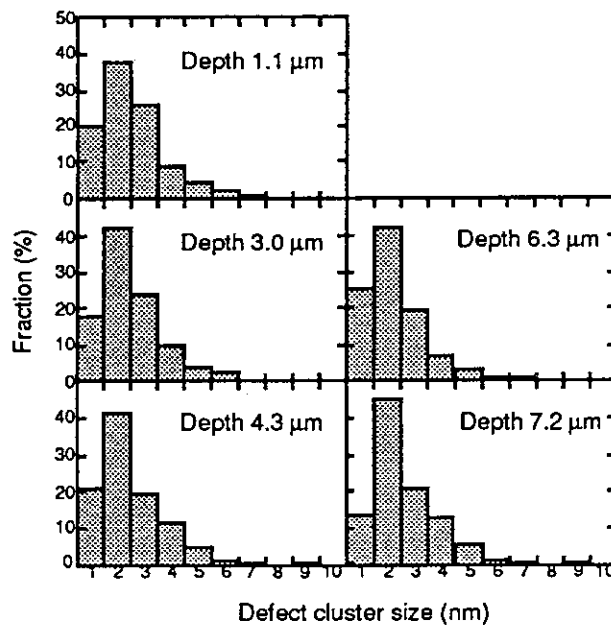


Fig. 3 Size of defect clusters in defect groups in gold irradiated with 170 MeV self-ions to 1.0×10^{14} ions/m² at room temperature.

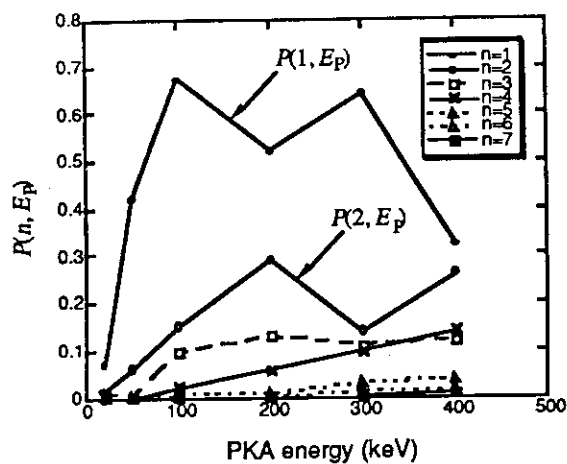


Fig. 4 Fraction of defect groups which contain n clusters as a function of PKA energy determined by 20 - 400 keV self-ion irradiation.

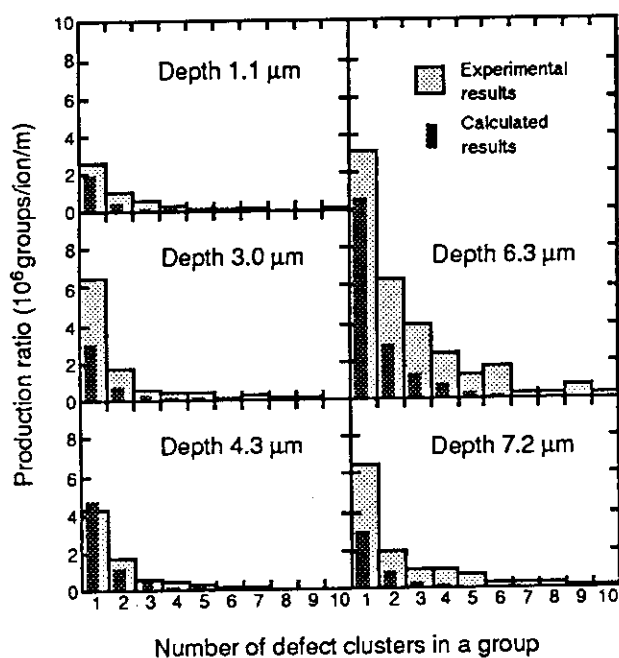


Fig. 5 Comparison of measured and estimated distribution of number of defect clusters in a group.

References

- 1) S. Ishino and N. Sekimura, Annales de Chemie, Science des Materiaux, 16 (1991) pp.341-350.
- 2) M. Kiritani, T. Yoshiie, S. Kojima and Y. Satoh, Radiation Effects and Defects in Solids 113 (1990) pp.75-96.

2.4 Electrical and Structural Properties of Li-ion Irradiated β -LiAl

K. Kuriyama, Hiromi Takahashi, Tomoharu Kato, Y. Kazumata*,
Y. Maeta*, H. Sugai**,

*College of Engineering and Research Center of Ion Beam
Technorogy, Hosei University,*

**Department of Physics, JAERI, **Department of Radioisotopes,
JAERI*

LiAl alloy is an useful material for solid-blankets of nuclear fusion¹⁾. Electrical conductivity of β -LiAl below room temperature has been reported²⁻⁴⁾. The important feature of the conduction mechanism for β -LiAl is governed by positive carriers(holes)^{5,6)} in the valence band. The electrical conductivity based on these holes is affected considerably by the defect structure⁷⁾ in β -LiAl (about 48-56 at.% Li). The defect structure at room temperature consists of two types of defects: vacancies in the lithium sublattice (V_{Li}), and lithium anti-structure atoms in the aluminum sublattice (Li_{Al}). A heat-capacity anomaly⁸⁾ relating to an abrupt change in the resistivity has been observed at around 95 K near the critical composition corresponding to the Li-deficient region. The anomalous behavior is closely correlated with the lower temperature ordering or clustering of Li vacancies^{8,9)}. The purpose of this work is (i) to measure the electrical resistivity of β -LiAl before and after heavy ion irradiation and (ii) to survey the modification of Li vacancies in Li-ion irradiated β -LiAl. In the previous report¹⁰⁾, we have studied the room-temperature resistivity of β -LiAl before and after Li-ion irradiations. A remarkable change in resistivity was not observed at room temperature since some of Li-ion-irradiation-induced defects are already recovered at room temperature. In this report, we describe the temperature-dependence of electrical resistivity of β -LiAl before and after Li-ion-irradiations.

Samples were prepared by a resistance furnace melting of 99.9% lithium

and 99.999% aluminum. The details of sample preparation have been previously described¹¹⁾. Li-ion irradiations were performed by a tandem accelerator at JEARI. 60 MeV- $^7\text{Li}^{3+}$ ions were used in this study. The projected range of Li^{3+} evaluated using TRIM was 0.56 mm. The dimension of Samples used here is about $5 \times 5 \times 1.5 \text{ mm}^3$.

Figure 1 shows a temperature dependence of resistivity of $\beta\text{-LiAl}$ before and after Li-ion irradiations. The Li dose is $1.6 \times 10^{15} \text{ cm}^{-2}$. Before irradiation, one can observe an abrupt change in resistivity at around 100 K (see open circles in Fig.1). This anomalous behavior has been associated with the lower temperature ordering⁹⁾ of Li vacancies. The resistivity after irradiation increases slightly below an ordering temperature (see closed circles in Fig.1). Figure 2 shows the Li dose versus resistivity for a sample irradiated at around 20 K. This indicates the tendency to increase in resistivity with increasing Li-ion dose. However, the resistivity is saturated at around $8 \times 10^{14} \text{ Li cm}^{-2}$. The increase in resistivity would be attributed to the transition from an ordered arrangement of Li vacancies to the partially disordered arrangement of Li vacancies, since in room-temperature annealed samples after Li-ion irradiations, the resistivity values are coincident with those before Li-ion irradiations (see open circles in Figs. 1 and 3). This recovery does not arise from the disappearance of Li vacancies and/or Li_{Al} antisite defects induced by Li-ion irradiations, because these defects can be existed stably in $\beta\text{-LiAl}$ ⁷⁾. Figure 3 shows a temperature dependence of resistivity of $\beta\text{-LiAl}$ after the room-temperature annealing of Li-ion irradiated sample (see closed circles in Fig.3). The Li dose is $8.6 \times 10^{14} \text{ cm}^{-2}$. The increase in resistivity was also reproduced below an ordering temperature of Li vacancies as shown in the first run of Li-ion irradiations (closed circles in Fig.1).

References

- 1) J.R.Powell, F.T.Miles, A.Aronson and W.E.Winsche: *BNL-18236*, Bookhaven National Laboratory(1973).
- 2) K.Kuriyama, T.Kamijoh and T.Nozaki: *Phys. Rev. B22*, 470 (1980); K.Kuriyama, S.Yamada, T.Nozaki and T.Kamijoh: *Phys. Rev. B24*, 6158(1981).
- 3) T.Asai, M.Hiratani and S.Kawai: *Solid State Commun.* **48**,173 (1983).

- 4) L.H.Hall, T.O.Brun, G.W.Crabtree, J.E.Robinson, S. Susman and T.Tokuhiro: Solid State Commun. **48**, 547(1983).
- 5) K.Kuriyama, T.Nozaiki and T.Kamijoh: Phys. Rev. B**26**, 2235(1982).
- 6) M.Yahagi: Phys. Rev. B**24**, 7401(1981).
- 7) K.Kishio and J.O.Brittain: J. Phys. Chem. Solids **40**, 993(1979).
- 8) K. Kuriyama, S. Yanada, T. Nozaki, and K. Kamijoh, Phys. Rev. B**24**, 6158 (1981).
- 9) T.O.Brun, S.Susman, R.dejus, B.Granelli, and K.Sköld, Solid State Commun. **45**, 721 (1983).
- 10) K. Kuriyama, H. Takahashi, C. Yoshiie, Y. Kazumata, H. Sugaai, *JAERI TANDEM, LINAC & V.D.G.* (Annual Report 1991), p.60.
- 11) K.Kuriyama, S.Saito and K.Iwamura: J. Phys. Chem. Solids **40**, 457(1979)457.

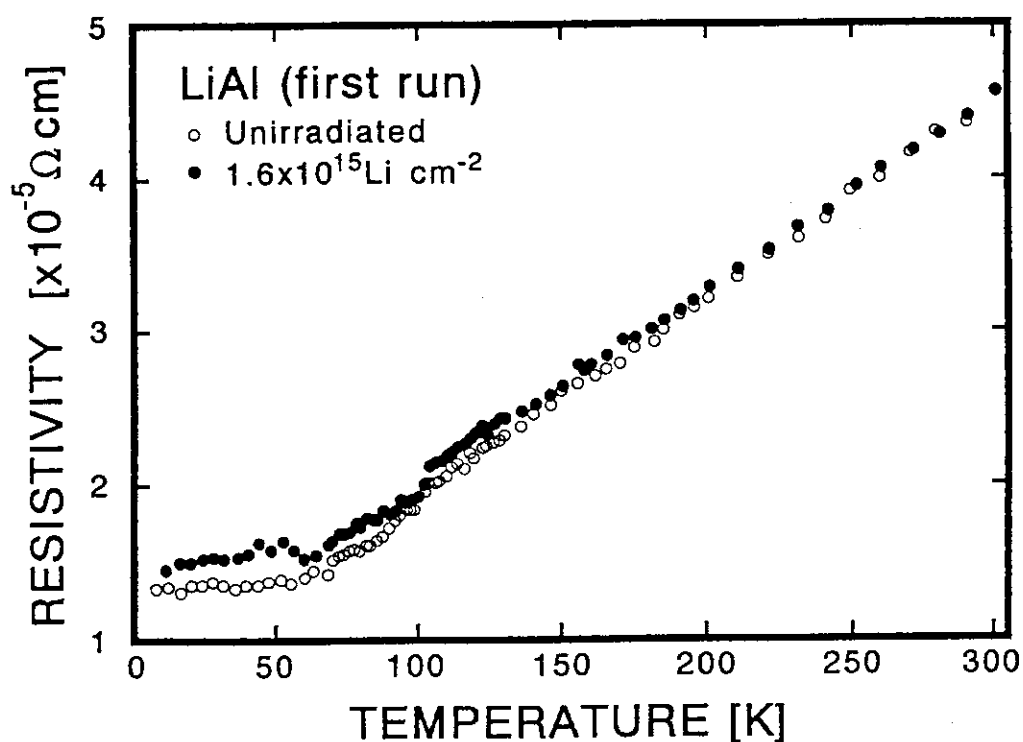


Fig.1. Temperature dependence of electrical resistivity of β -LiAl before and after Li-ion irradiation.

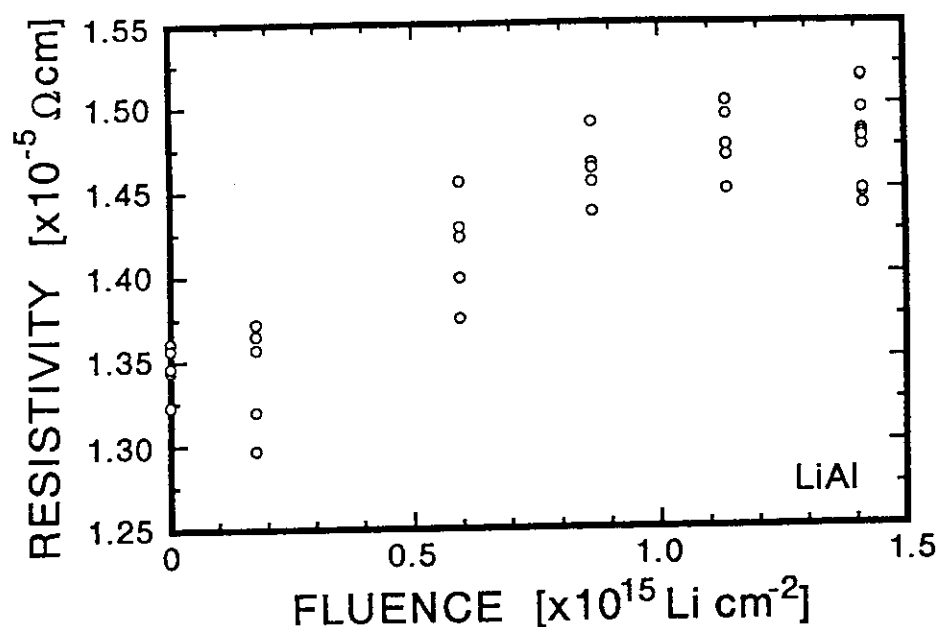


Fig.2. Li-ion dose versus electrical resistivity of β -LiAl irradiated at around 20 K.

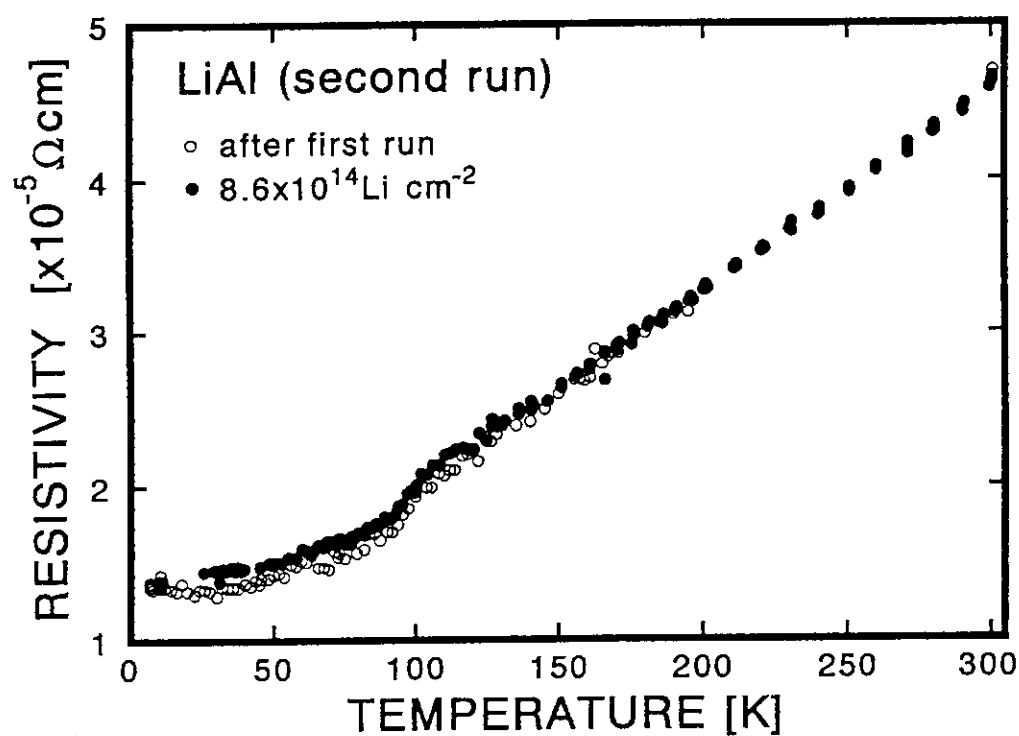


Fig.3. Temperature dependence of electrical resistivity of β -LiAl; room-temperature annealed sample(open circles) after Li-ion irradiation and Li-ion irradiated sample(closed circles) after the room-temperature anneal.

2.5 Effect of 180MeV Cu^{11+} and Br^{11+} Irradiation on Textured $\text{Bi}_2\text{Sr}_2\text{CaCu}_2\text{O}_x$

Hiroaki KUMAKURA, Hitoshi KITAGUCHI, Kazumasa TOGANO, Satoru OKAYASU* and Yukio KAZUMATA*

National Research Institute for Metals, *Japan Atomic Energy Research Institute

INTRODUCTION

For the application of $\text{Bi}_2\text{Sr}_2\text{CaCu}_2\text{O}_x$ (Bi-2212) in high-temperature regions, substantial increase of critical current density J_c in magnetic fields is required. This means that we must enhance so-called irreversibility field B_{irr} which is defined as the field where J_c becomes zero. For this purpose, introduction of pinning centers are now being attempted. One of the effective methods of introducing pinning centers is irradiation.¹⁻³⁾ In our previous papers, it is shown that 180MeV Cu^{11+} irradiation is highly effective to introduce flux pinning centers and to increase B_{irr} in the textured Bi-2212 tapes.^{4,5)} High-resolution transmission electron microscope observation clearly indicated that long columns having amorphouslike structure were introduced by the irradiation.⁶⁾ In this paper, we performed systematic experiments on high energy Cu^{11+} and Br^{11+} irradiations on textured Bi-2212 and report on the effect of irradiations on the flux pinning at various temperatures.

EXPERIMENTALS

Samples were grain-oriented polycrystalline Bi-2212 tapes prepared by a doctor blade method.⁷⁾ 180MeV Cu^{11+} and Br^{11+} irradiation were carried out on the Bi-2212 layers with fluence from 10^{10} - 10^{12} ions/cm². The direction of incident beam was perpendicular to the tape surface (i.e., parallel to the c-axis of Bi-2212). The projected range of the Cu^{11+} and Br^{11+} in Bi-2212 were calculated to be 16.4 μm and 14.7 μm using the method reported by Aruga et al,⁸⁾ respectively. These values were larger than the thickness of Bi-2212 layers. Therefore, almost all ions penetrated through the Bi-2212 layers. For comparison, 3MeV electron irradiation was also carried out at room temperature using the Dynamitron accelerator at Takasaki Research Establishment in JAERI with fluence of 10^{17} ~ 5×10^{18} e-/cm². Transition

temperature T_c was measured by the resistive method. Pinning characteristics were evaluated from the hysteresis ΔM in d.c. magnetization curves. D.c magnetization curves were measured in magnetic fields up to 8T at various temperatures up to T_c using a vibrating sample magnetometer. Magnetic field was applied parallel to the c-axis (perpendicular to the tape surface).

RESULTS AND DISCUSSION

T_c of Cu^{11+} and Br^{11+} irradiated samples is almost constant for fluence up to 5×10^{10} ions/cm², and then decreases for larger fluence. Transition width increases with increasing fluence for ion irradiation. This decrease in T_c is associated with the distortion of the crystal structure in the surroundings of the columnar defects as discussed elsewhere.⁹⁾ T_c of the Bi-2212 is much less sensitive to electron irradiation. Electron irradiation mainly produces small defects such as vacancies, and the decrease of T_c is due to these defects.

Substantial enhancement of the magnetic hysteresis ΔM was obtained for a fluence larger than 5×10^{10} Cu^{11+} /cm² and 1×10^{10} Br^{11+} /cm². This indicates that the intragrain J_c is increased by the ion irradiations. For electron irradiation, on the other hand, much larger fluence, larger than 10^{17} e⁻/cm², was required for the enhancement of ΔM . Figure 1 shows fluence dependence of ΔM in 1T and 2T at 24K for Cu^{11+} , Br^{11+} and electron irradiated samples. For Cu^{11+} and Br^{11+} irradiated samples, ΔM significantly increases with increasing fluence. For Cu^{11+} irradiation maximum of ΔM was observed at the fluence of $\sim 9 \times 10^{11}$ and then ΔM decreases for larger fluence, while for Br^{11+} irradiation maximum of ΔM was observed at smaller fluence. These ΔM decrease at larger fluence for Cu^{11+} and Br^{11+} irradiation is primarily due to the decrease of T_c . For the electron irradiated samples, on the other hand, enhancement of ΔM is not so large as the enhancement for ion irradiation, and saturation of ΔM was observed at $\sim 10^{18}$ e⁻/cm².

B_{irr} was defined as the field where ΔM vanished in M-B curve with criterion of 0.1emu/cm³. B_{irr} was also enhanced by the ion irradiation. This indicates that columnar defects is effective in increasing B_{irr} when field is parallel to the defects. Figure 2 shows enhancement factor of B_{irr} by the irradiation, $B_{irr}(\text{Irrad.})/B_{irr}(\text{No irradi.})$, for Cu^{11+} , Br^{11+} and electron irradiations as a function of temperature. The enhancement factors for the

Cu^{11+} and Br^{11+} irradiations increase with increasing temperature and take maximum values at $\sim 60\text{K}$. At low temperatures of $\sim 4.2\text{K}$, enhancement of B_{irr} by the ion irradiation is comparatively small. At this temperature range small defects which have already existed before the irradiation act as effective pinning centers, and the contribution by the columnar defects are relatively small. With increasing temperature, however, such small pinning centers become ineffective due to small pinning potential energy, and pinning by the columnar defects becomes dominant. At $\sim 60\text{K}$ an order of magnitude higher B_{irr} was obtained for Cu^{11+} and Br^{11+} irradiations. Above 60K , however, enhancement of B_{irr} by the ion irradiation becomes small with increasing temperature. One of the reasons for this small enhancement of B_{irr} at high temperature region is due to the degradation of T_c by the irradiation. However, the main reason is that pinning potential energy for Cu^{11+} and Br^{11+} irradiated samples is not large enough for the suppression of flux creep at high temperatures. Pinning energy estimated from relaxation of magnetization is as small as 40meV at 40K even after the ion irradiation.

This indicates that columnar defects are not such strong pinning centers in the Bi-2212 at high temperature region. This small pinning energy should be related to the intrinsic characteristic of pinning in Bi-2212, which originates from strong two-dimensionality.³⁾ For flux lines in superconductors having a weakly coupled layer structure, the so-called two-dimensional pancake model¹⁰⁾ is applicable when magnetic fields are parallel to the *c*-axis. In this model, the stacks of pancakes are easily sheared along the *a* or *b* direction, and therefore flux lines are not rigid but very flexible. Therefore, depinning of one or a few pancakes from the columnar defects occurs with the aid of thermal activation, and small potential energy is obtained. These results suggests that it is difficult to increase B_{irr} and, hence, J_c in magnetic fields of Bi-2212 significantly at high temperatures by introducing pinning centers.

References

- 1) L. Civale, A.D. Marwick, T.K. Worthington, M.A. Kirk, J.R. Thompson, L. Krusin-Elbaum, Y.R. Sun, J.R. Clem, and F. Holtzberg, Phys. Rev. Lett. **67**(1991)648.
- 2) J.R. Thompson, Y.R. Sun, H.R. Kerchner, D.K. Christen, B.C. Sales, B.C. Chakoumakos, A.D. Marwick, L. Civale, and J.O. Thompson, Appl. Phys. Lett. **60**(1992)2306.

- 3) W. Gerhauser, G. Ries, H.W. Neumuller, W. Schmidt, O. Eibl, G. Seamann-Ischenko, and Klaumunzer, Phys. Rev. Lett. **68**(1992)879.
- 4) H. Kumakura, S. Ikeda, H. Kitaguchi, K. Togano, H. Maeda, J. Kase, T. Morimoto, S. Okayasu and Y. Kazumata, J. Appl. Phys. **72**(1992)800.
- 5) H. Kumakura, H. Kitaguchi, K. Togano, H. Maeda, J. Shimoyama, S. Okayasu, and Y. Kazumata, Jpn. J. Appl. Phys. **10A**(1992)L1408.
- 6) B. Chenevier, S. Ikeda, H. Kumakura, K. Togano, S. Okayasu, and Y. Kazumata, Jpn. J. Appl. Phys. **31**(1992)L777.
- 7) J. Kase, T. Morimoto, K. Togano, H. Kumakura, D.R. Dietderich and H. Maeda, IEEE Trans. Magn. **27**(1991)1254.
- 8) T. Aruga, N. Nakata and S. Takamura, Nucl. Instrum. & Method **B33** (1988)748.
- 9) H. Kumakura, H. Kitaguchi, K. Togano, H. Maeda, J. Shimoyama, S. Okayasu and Y. Kazumata, to be published in J. Appl. Phys.
- 10) J.R. Clem, Phys. Rev. **B43**(1991)7837.

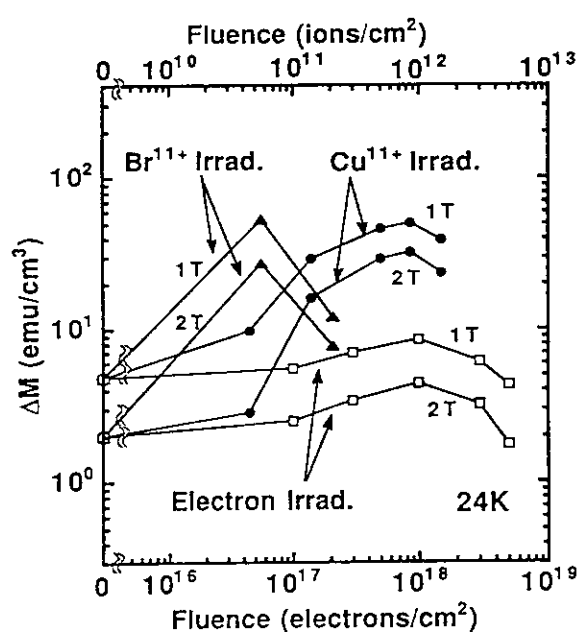


Fig.1. Hysteresis in d.c. magnetization at 24K as a function of fluence for Cu¹¹⁺, Br¹¹⁺ and electron irradiated Bi-2212.

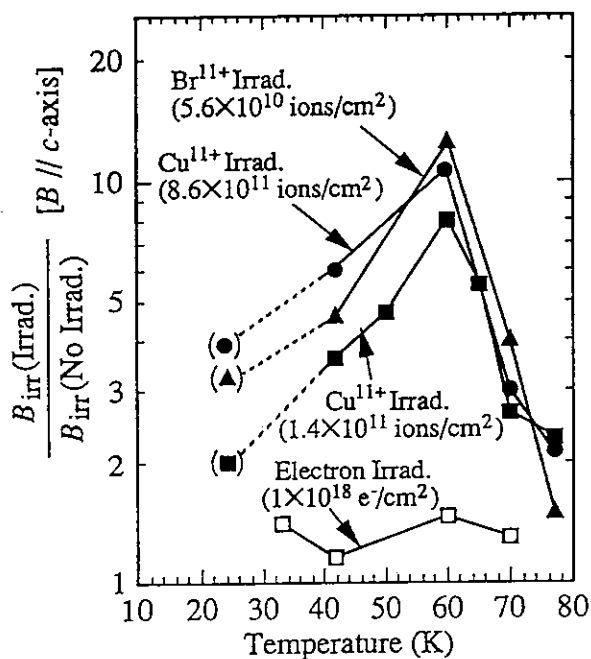


Fig. 2. Enhancement of Birr field by Cu¹¹⁺, Br¹¹⁺ and electron irradiation as a function of temperature.

2.6 High Energy Au Ion Irradiation to $\text{EuBa}_2\text{Cu}_3\text{O}_x$ Thin Films

Yukio Kazumata, Satoru. Okayasu

and Osamu Michigami*

Department of physics, JAERI.

*NTT Interdisciplinary Research Lab.

In high T_c superconducting materials, two kinds of defects are observed. These are point-like defects including clustered defects and columnar defects. When energetic particles are bombarded into a crystal, they dissipate their energies through the two processes; one is nuclear collisions and the other is electron excitations. Point defects are produced by the former process and columnar defects are reportedly introduced by the latter when the energy dissipation due to this process exceeds 2 keV/\AA .^{1,2,3}

In this report, we describe the effects of columnar defects on the superconductivity in $\text{EuBa}_2\text{Cu}_3\text{O}_x$ thin films. The thin films were irradiated by 230 MeV Au^{14+} ions by which columnar defects will be introduced. After the irradiations, magnetizations, ΔM calculated from hysteresis loops, irreversibility lines and activation energies for flux motion were studied.

High energy ion irradiations, 230 MeV Au^{14+} ions, were carried out by the Tandem accelerator in JAERI at liquid nitrogen temperature. $\text{EuBa}_2\text{Cu}_3\text{O}_x$ thin films, 5000 \AA in thickness, were prepared by a sputtering method. We used a Quantum Design superconducting quantum interference device (SQUID) Model MPMS magnetometer for measurements. A scan length of 3 cm was used so as to have sufficient uniformity of the applied magnetic field.

The dissipation energy due to electronic excitation by 230 MeV Au^{14+} ions is calculated to be 3 keV/\AA ,⁵ which is much larger than the formation energy (2 keV/\AA) of columnar defects. Therefore, columnar defects are presumably induced by

the irradiation.

The transition temperature, T_c , is 84 K before the irradiation and only a slight change, below 1 K, is observed by the dose of 2.3×10^{11} ions/cm², but it is reduced to 79.5 K after the dose of 6.0×10^{11} ions/cm².

The change of ZFC susceptibilities by the irradiations is shown in Fig.1. The susceptibilities at the high dose significantly decrease, particularly above 100 gauss, but no notable change is observed at the low dose.

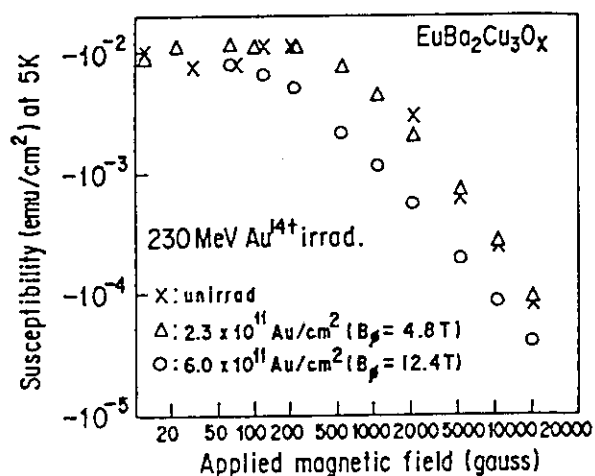


Fig.1. The change of ZFC Susceptibility at 5 K by the irradiation.

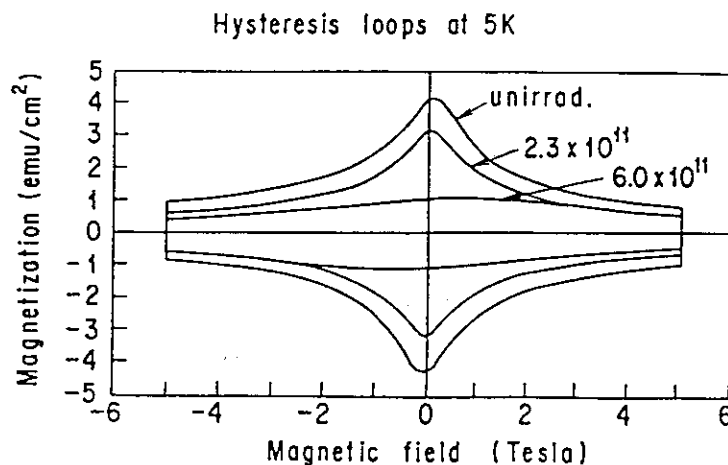


Fig.2. Hysteresis loops at 5 K.

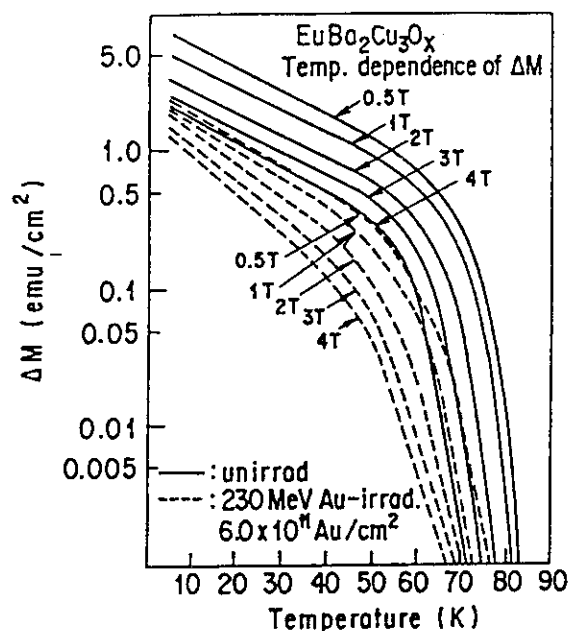


Fig.3. Temperature dependence of ΔM before and after the irradiation.

Hysteresis loops at 5 K are shown in Fig.2. When the loop at the high dose is compared with that of before the irradiation, the former takes a flat form without the peak found at 0 T in the latter loop. The peak, however, appears at high temperatures, and it is clearly observed above 45 K. As seen from the hysteresis loops in Fig.2, ΔM decrease with an increase of irradiation dose, particularly at lower magnetic fields. The temperature dependence of ΔM is shown in Fig.3. Two slopes in each field are observed. One at low temperatures is lower, and the other at high temperature is higher. After the irradiation, the slopes of the former become higher and those of the latter become lower. As the consequence of the change of the slope, the transition temperature from low to high slope broadens and loses sharpness as seen in the curve at 4 T after the irradiation.

Irreversibility lines obtained from hysteresis loops are shown in Fig.4. After the irradiation, the slopes of the lines become higher and breaks of the lines are found at high magnetic fields. A irreversibility line is usually expressed by the following equation,

$$H_{irr} = a[1 - (T_{irr}/T_c)]^n \quad (1)$$

The exponent n in eq.(1) is estimated to be 1.1 and 2.8 for

unirradiated and the high dose lines, respectively.

Activation energies calculated from the measurements of magnetic relaxation scarcely change for the low dose, but a remarkable reduction is observed for the high dose above 20 K.

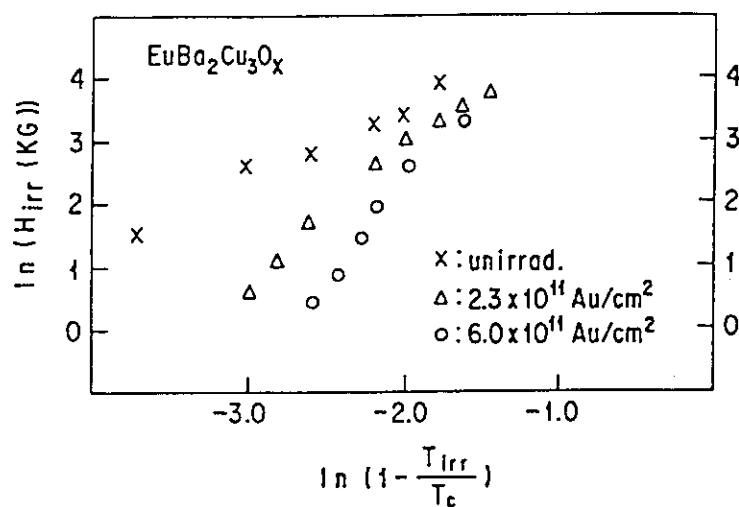


Fig.4. The change of irreversibility lines by the irradiation.

These experiments are summarized as follows:

- (1) After the irradiation, ΔM decrease although columnar defects are presumably produced.
- (2) Change of irreversibility line. Increase of the slope with an increase of the fluence.

REFERENCES

1. L.Civale, A.D.Marwick, T.K.Worthington, M.A.Kirk, J.R.Thompson, L.Krusin-Elbaum, Y.Sun, J.R.Clem, and F.Holtzberg, Phys. Rev. Letters 67(1991)648
2. W.Gerhauser, G.Ries, H.W.Neumuller, W.Schmidt, O.Eibl, G.Saemann-Ishenko, and S.Klaumunzer, Phys. Rev. Letters 68(1992)879.
3. H.Kumakura, S.Ikeda, H.Kitaguchi, K.Togano, H.Maeda, J.Kase, T.Morimoto, S.Okaysu, and Y. Kazumata, J. Appl. Phys. 72(2)(1992)800.
4. D.S.Billington and J.H.Crawford, Jr, Radiation damage in solids(Princeton, New Jersey,1961),p.21
5. T.Aruga, K.Nakata, and S.Takamura, Nucl. Instrum & Method B33(1988)748.

2.7 Effect of Au Ion Irradiation on Lattice Parameter in $\text{EuBa}_2\text{Cu}_3\text{O}_y$ Thin Film

Norito ISHIKAWA, Akihiro IWASE, and Tadao IWATA
Hiroshi MAETA, Koji TSURU*, and Osamu MICHIKAMI*

Department of Physics, JAERI,

*Electron Devices Laboratory,

NTT Interdisciplinary Research Laboratories.

In this study, we investigated an effect of heavy ion irradiation on crystal structure in $\text{EuBa}_2\text{Cu}_3\text{O}_y$ films. It has almost been established that irradiation with heavy ions, such as $\text{Sn}^{1)}$, $\text{Cu}^{2)}$, $\text{Xe}^{3)}$, etc., can create columnar defects in high- T_c superconductors. It is particularly interesting to examine the interaction between defects and vortices because it can be related to the recent controversy concerning vortex glass melting^{4),5)}. As a first step of the examination, we tried to investigate an effect of heavy ion irradiation on crystal structure by measuring X-ray diffraction pattern.

An epitaxially grown $\text{EuBa}_2\text{Cu}_3\text{O}_y$ film was prepared on MgO substrate by rf magnetron sputtering. The thickness of the film was about 0.3 μm . Superconducting transition temperature before irradiation was about 81K. The film was found to be c-axis oriented. 120 MeV Au ion was irradiated to the direction parallel to the c-axis of the sample at room temperature. The structural properties were estimated with X-ray diffractometer using Cu K_α radiation. c-axis lattice parameter (a_0) before irradiation was 11.760Å.

c-axis lattice parameter (a) as a function of ion fluence Φ was plotted in Fig.1. We could observe increase and saturation of a with increasing fluence. Damage production rate versus fluence were plotted in Fig.2 in order to estimate total cross section of defect production.

We employed following formulation^{6),7)} to analyze the data. It is assumed that there are several different types of defect configuration produced by irradiation and some of them are

annihilated by subsequent irradiation. If defects of type (1) to type (k-1) are unstable against subsequent irradiation and if all other types of defects, designated as type (k), are stable against subsequent irradiation, then the defect production and radiation annealing can be described by the following simultaneous differential equations;

$$\begin{aligned} \frac{dc}{d\Phi} \cong & \sum_{j=1}^{k-1} [\sigma_{d,j} - \sigma_{r,j} c_j(0)] \\ & \times \exp[-(\sigma_{r,j} + 2\nu_0 \sigma_{d,j}) \Phi] \\ & + \sigma_{d,k} \exp[-2\nu_0 \sigma_{d,k} \Phi]. \end{aligned}$$

where c is the total concentration of defects, Φ is the fluence, and the index j denotes the type of defects. For the defects of type j , c_j is the concentration, $\sigma_{d,j}$ is the displacement cross section, $\sigma_{r,j}$ is the cross section for radiation annealing, and $c_j(0)$ is the concentration of predoped defects of type j . ν_0 is the spontaneous recombination volume. According to the above formulation, we concluded from Fig.2 that the damage production rate curve can be fitted by the sum of 3 exponential functions of ion fluence. This indicates there are three different processes of defect production with different production cross section and different cross section for radiation annealing. Total cross section of defect production was estimated to be about 10^{-13} cm^2 by taking the value of damage production rate at $\Phi \rightarrow 0$.

References

- 1) L.Civale, A.D.Marwick, T.K.Worthington, M.A.Kirk, J.R.Thompson, L.Krusin-Elbaum, Y.Sun, J.R.Clem, and F.Holtzberg, Phys. Rev. Lett. 67 (1991) 648.
- 2) H.Kumakura, S.Ikeda, H.Kitaguchi, K.Togano, H.Maeda, J.Kase, T.Morimoto, S.Okayasu and Y.Kazumata, J. Appl. Phys. 72 (1992) 800.
- 3) D.Bourgault, M.Hervieu, S.Bouffard, D.Groult, and B.Raveau, Nucl. Inst. and Meth. B42 (1989) 61.

- 4) T.K.Worthington, M.P.A.Fisher, D.A.Huse, John Toner, A.D.Marwick, T.Zabel, C.A.Feild, and F.Holtzberg, Phys.Rev. B, 46 (1992) 11854.
- 5) W.Jiang, N.C.Yeh, D.S.Reed, U.Kriplani, T.A.Tombrello, A.P.Rice, and F.Holtzberg, Phys. Rev. B 47 (1993) 8308.
- 6) T.Iwata and A.Iwase, Nucl. Inst. and Meth. B61 (1991) 436
- 7) T.Iwata and A.Iwase, Rad. Effects and Defects Solids 113 (1990) 135.

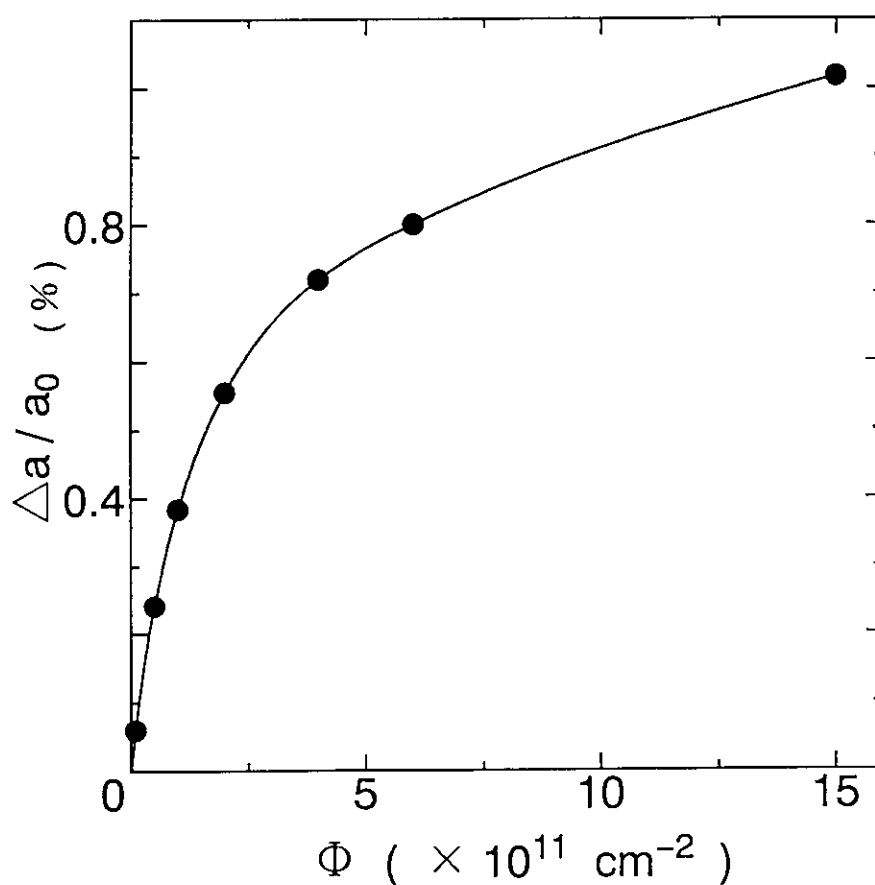


Fig.1

Increment of lattice parameter(a) normalized by a_0 is plotted as a function of ion fluence. $a_0=11.760\text{\AA}$ is lattice parameter before irradiation. Solid curve is fitted to the data according to the differential equations explained in the text.

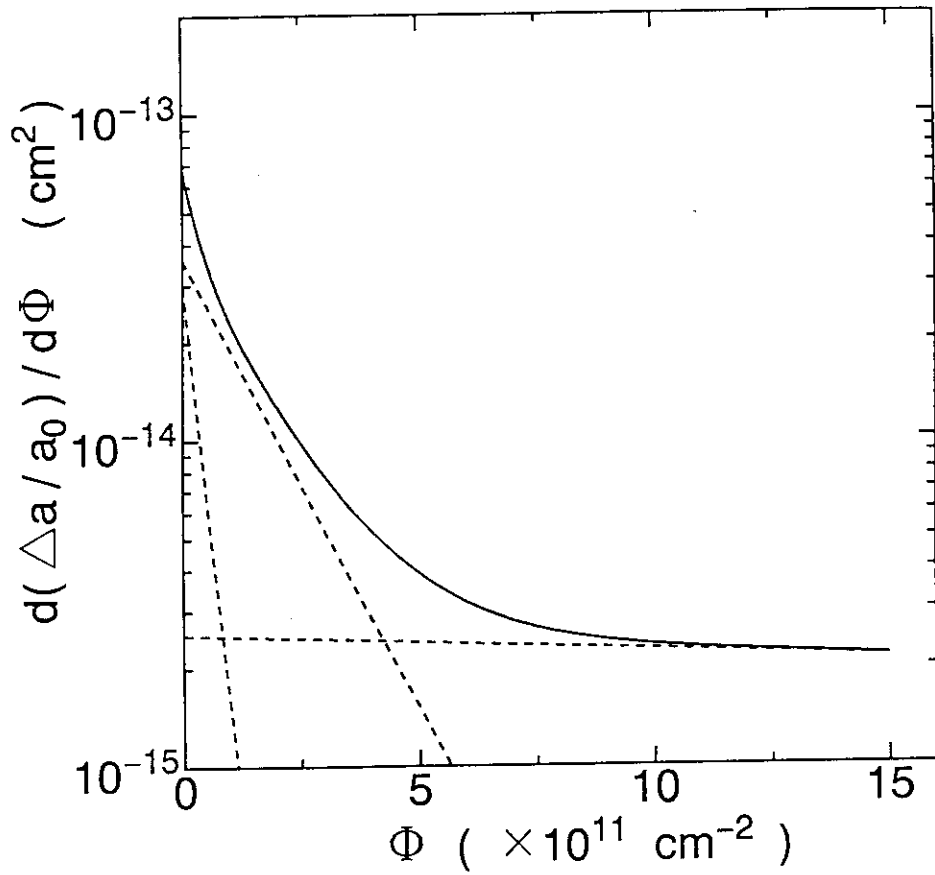


Fig.2

Damage production rate is plotted as a function of ion fluence using the solid curve in Fig.1. $\Delta a = a - a_0$. Each straight dotted line indicates different defect production process. The solid curve is a sum of 3 straight dotted lines, suggesting that there are 3 different defect production processes.

2.8 Irradiation Effect on Thermal Expansion of Synthetic Single Crystal Diamond

Katsuji HARUNA, , Hiroshi MAETA*, Fumihisa ONO**,
Hisao AIZAWA, Hideki USUI and Kazutoshi OHASHI

Faculty of Engineering, Tamagawa University,

*Department of Physics, JAERI

**Liberal Arts of Okayama University

1. Introduction

Diamond based semiconductor devices may turn out to be of great technological importance due to the outstanding physical properties, such as high thermal conductivity, good thermal and chemical stability. It is very strong against radioactive rays and fits to the electronic devices in the high temperature region owing to the wide energy gap. However, there are no n-type diamonds so far found. To make the electron devices based on diamond semiconductor, it is essential to construct the p-n junction. There are many methods to dope the impurities into semiconductors. In order to get n-type diamond, we select the ion implantation method. Ion implantation is a prime candidate technique for doping, but the issues of annealing radiation damage, avoiding graphitization, and driving implanted species into substitution sites have not been completely resolved. Before solving these problems, however, there are many physical properties of as grown synthetic single crystal diamond which are to be clarified. Among these, we select the thermal expansion problem. Usually the lattice parameter of a cubic crystalline material increases with increasing temperature, so the linear thermal expansion coefficient is positive. Physically this positive thermal expansion is attributed to the fact that the lattice separation becomes wider with increasing temperature. However, there are many materials that show a negative thermal expansion coefficient, including Si, Ge, GaP, InP.^{1,2,3)} Such tetrahedrally bonded solids show negative values for the thermal expansion coefficient below approximately 100 K. These materials basically have diamond structures. Therefore, it is very interesting to know whether the diamond crystal has a negative thermal expansion coefficient or not in the low temperature region and how the irradiation effects on it will be.

We measured the lattice parameter of a synthetic diamond crystal using the Bond method.⁴⁾ Then, we obtained the thermal expansion coefficients from our experiments. The negative thermal expansion was not confirmed even with the maximum accuracy in our measurements. We also measured the temperature dependence of the lattice parameter of the synthetic diamond single crystal irradiated by high energy accelerated heavy self ions. But, its thermal expansion behavior does not show any remarkable change.

2. Experimental Procedures

The synthetic diamond single crystals used in our experiment were purchased from Sumitomo Denko Co., Ltd. Ib type contained less than 80 ppm of nitrogen and were colored yellow. Its shape was thin square plates with dimensions of $3.5 \times 3.5 \times 0.3 \text{ mm}^3$ and the surfaces of the specimens were oriented parallel to the (100) plane. We measured the temperature dependence of lattice parameter for two kinds of specimens by Bond method. One is as grown and another irradiated with 100 MeV C^{+6} ion up to the fluences of $3.5 \times 10^{15} \text{ ions/cm}^2$ at about liquid nitrogen temperature using tandem accelerator. After the irradiation, the specimen was warmed up to room temperature. The measurements were performed in a specially designed glass cryostat.⁵⁾ To attain the highest possible accuracy, a finely focused $\text{K}\beta$ line from an iron target was used, together with the highest possible reflection angle corresponding to (100) planes. This was the (400) plane, for which $2\theta = 160.01^\circ$. The wavelength of the $\text{K}\beta$ line was taken as 1.75653 \AA . Before each measurement, the tilt angle of the specimen was carefully adjusted and the relative accuracy of $\pm 1 \times 10^{-6}$ was maintained in determining the lattice parameter. The temperature was varied in the range 4.2-320 K and a precision of $\pm 0.1 \text{ K}$ was maintained during the course of the experiment.

3. Results and Discussion

In Fig. 1, the lattice parameters of two specimens in the temperature range 4.2-320K are plotted. Open circle shows that of as grown diamond crystal and solid circle that of the irradiated one. The values are corrected for refraction, absorption and Lorentz factors. It is clearly shown that the lattice parameter is more or less constant between 4.2-90K. This feature is considerably different from those observed in other tetrahedrally bonded solids. Since there is no distinct minimum in the plot of

the lattice parameter over this wide temperature range, we conclude that there is no negative thermal expansion as within as the precision of our measurement. Solid circle shows the temperature dependence of lattice parameter of the specimen irradiated by high energy accelerated heavy ions. Since there is no distinct minimum in the plot of the lattice parameter over wide low temperature range, we also observe that there is no negative thermal expansion in the irradiated diamond single crystal as far as the precision of our measurement is concerned.

The thermal expansion coefficients are calculated from the observed curves of the lattice parameter. The results are plotted in Fig. 2. Open circle and solid circle correspond those in Fig.1. The solid line traces reasonable values of thermal expansion coefficients that are fitted to the fourth-order polynomial. These coefficients are determined by the method of least squares. Present result shows that diamond has a very small thermal expansion coefficient (of the order of 10^{-8}) below 100 K and that the lattice parameter is more or less constant between 4.2-90 K. This is due to the very strong binding force of diamond. Recently Xu et al⁶⁾ reported their theoretical result of the thermal expansion of diamond. They showed that diamond has only positive thermal expansion coefficients using tight binding calculation. We may conclude that synthetic single crystal diamond does not show negative thermal expansion at low temperatures within our experimental precision. Present result is a support of their theory.

References

- 1) T. H. K. Barron, J. G. Collins and G. K. White: *Adv. in Phys.* 29 (1980) 609.
- 2) K. Haruna, H. Maeta, K. Ohashi and T. Koike :*J. Phys. C* (1986) 5149.
- 3) K. Haruna, H. Maeta, K. Ohashi and T. Koike: *J. Phys. C* 20 (1987)5275.
- 4) W. L. Bond: *Acta.Crystallogr.* 13 (1960) 814.
- 5) H. Maeta, T. Kato and S. Okuda :*J. Appl. Crystallogr.* 9 (1976) 378.
- 6) C. H. Xu, C. Z. Wang, C. T. Chan and K. M. Ho: *Phys. Rev. B* 43 (1991) 5024.

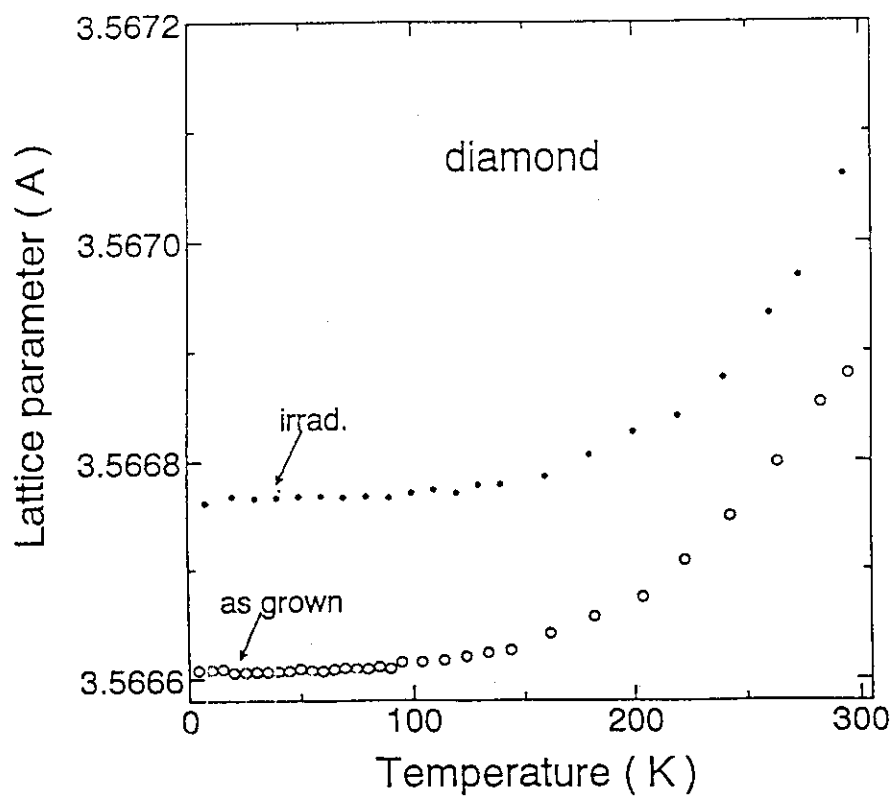


Fig.1 Temperature dependence of the lattice parameter for synthetic single crystal diamond

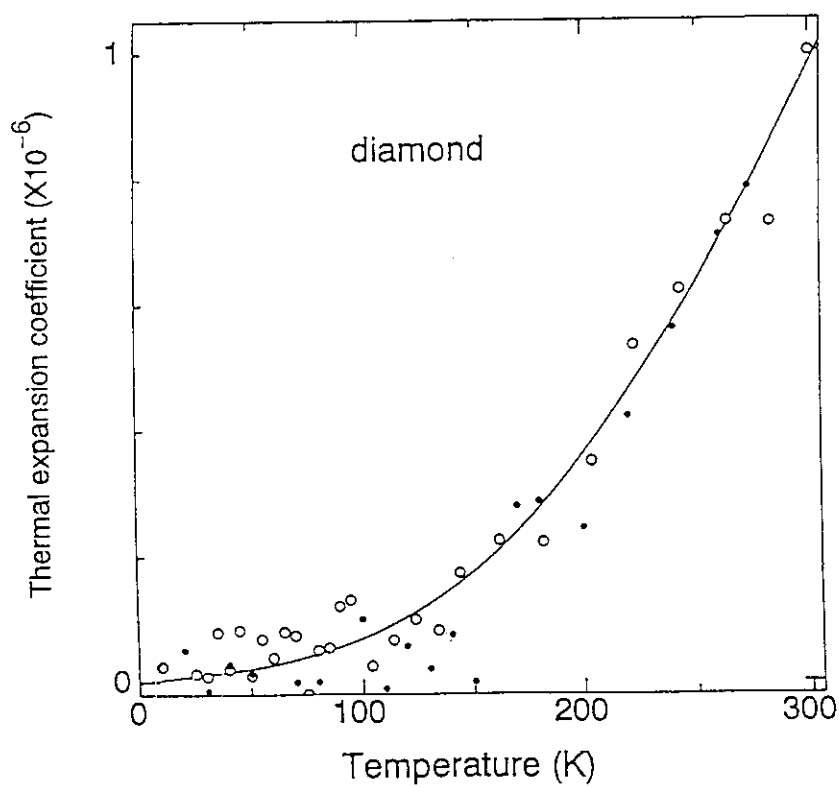


Fig.2 Temperature dependence of the thermal expansion coefficient for synthetic single crystal diamond

2.9 X-ray Study of Strain Distribution Produced by MeV Energy Ion Implantation

Hiroyuki TANAKA, Hirofumi TOMITA, Eiichi TSUJI,
Takuya KANAMARU, Masaru KURIBAYASHI
Hiroyuki KATOH, Kohtaro ISHIDA
Satoru OKAYASU*, Kazuya AIZAWA*
Hiroshi TOMIMITU* and Yukio KAZUMATA*

Science Univ. of Tokyo, *JAERI

Introduction

Ion implantation is a useful technique to inject impurity atoms into semiconducting crystals for IC device fabrication. Recently, many studies of high energy, over MeV, ion implantation are developed to make getter for improving device performance¹⁾. An ion implanted layer accompanies radiation damages which play crucial role in the device performance. Damage is produced by collision of implanted ions with crystal atoms which remove from their lattice position. Another damage is introduced by implanted ions stopped in the crystal with lattice distortion. Both damages introduce lattice expansion so that a strain depth profile directly relate to distribution of displaced atoms and stopping ions.

In this report, X-ray rocking curves of high energy ion implanted Si(111) wafers are investigated to determine strain profiles using the X-ray dynamical diffraction theory in distorted crystals²⁾. The strain profile obtained by simulation are compared with energy loss curves and stopping atom distribution calculated with Aruga's program³⁾ which is an expanded code of EDEP-1 for high energy region.

Experimental

Ni, Cu and Au ions were implanted into Si(111) wafers using the Tandem accelerator in JAERI at Tokai. The accelerating energy were 160MeV for Ni and Cu, and 230MeV for Au. During the implantation the sample holder were cooled with liquid

nitrogen.

X-ray rocking curves of the samples were obtained with multi-crystal diffractometer at BL-14B in Photon Factory at KEK in Tukuba. X-ray rocking curves from the distorted crystals are disrupted by very small angle, order of arc-seconds, around the Bragg peaks. Therefore, a high resolution diffractometer system should be used for investigating the strain profile. Our system used in this experiment was as follows; Vertically polarized synchrotron radiations at BL-14B were monochromatized first by a pair reflection of Si(111) crystals with (+,-) setting and the X-rays were more precisely monochromatized and paralleled by a Si(220) groove crystal which was set to the first monochromator crystals as (-,-), i.e. the monochromator reflection system was (+,-,-,+) setting. A sample crystal was mounted on a precise diffractometer. The diffracting and measuring equipments were controlled by a computer system.

Results and Discussion

Dotted curves in Figs. 1-a, 2-a and 3-a show the X-ray rocking curves measured from Si(111) wafers implanted by Cu, Ni and Au ions, respectively. Abscissae of the figures indicate deviation of diffraction angle and $W=1$ corresponds to $\Delta\theta=1.93''$ in the present case. Each rocking curve has a strong Bragg peak caused by a perfect region as well as subsidiary peaks due to a strain region. From computer simulation it can be concluded that position and intensity of the main subpeak are related to the magnitude and the width of the strain region. Furthermore, the oscillation of small peaks between a Bragg and a main subpeak determined shape of the strain profile. The best fitting simulation curves are shown in Figs. 1-a, 2-a and 3-a as solid curves. The strain profiles used for the calculations are shown in Figs. 1-b, 2-b and 3-b as solid curves. To compare with the strain profile, the energy loss per unit length and the distribution of stopping ions calculated by Aruga's program are also shown. An appearance of strain profile are nearly equal to the distributions of stopping ions except a region near the crystal surface, where

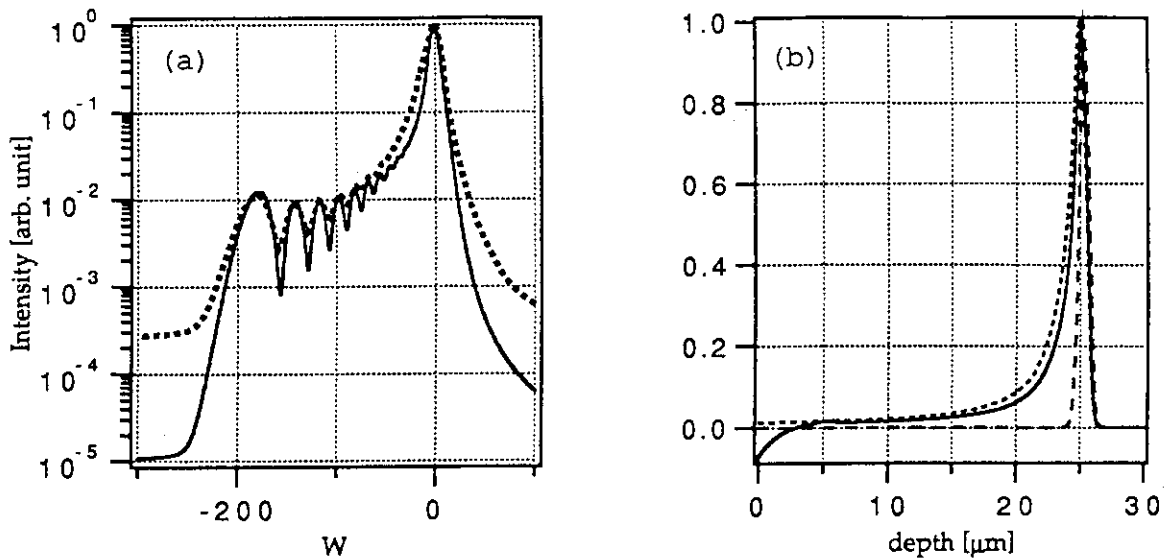


Fig.1. (a) Experimental (dots) and calculated (solid) rocking curve from Si(333) implanted Ni^{+10} 2.07×10^{14} [ions/cm²] with 160MeV. (b) Strain profile used (solid) and energy loss per unit length (dots) and stopping ion profile (dash). See text.

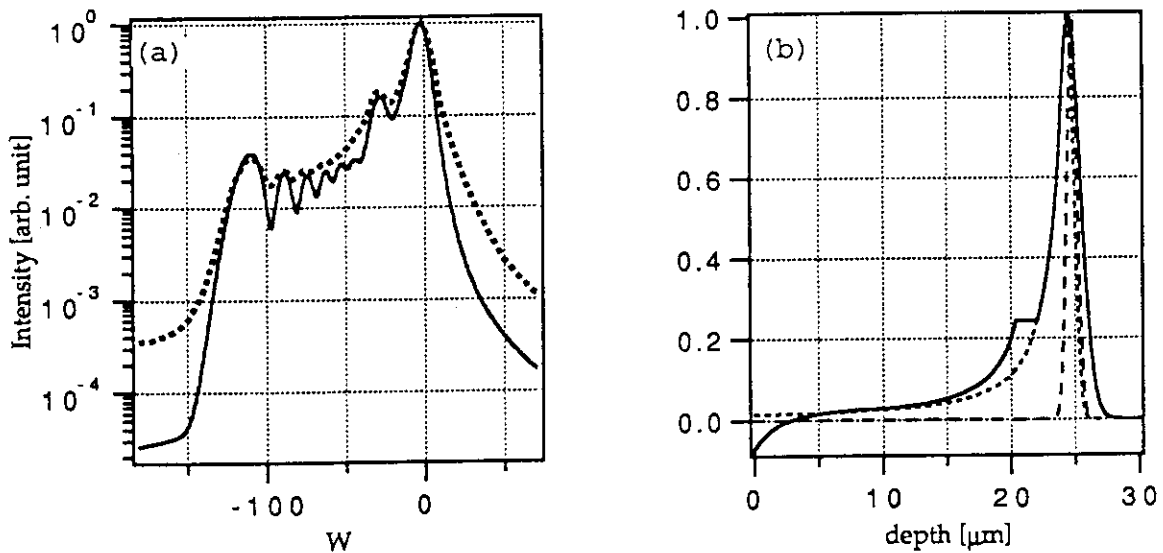


Fig.2. (a) Experimental (dots) and calculated (solid) rocking curve from Si(333) implanted Cu^{+10} 1.7×10^{14} [ions/cm²] with 160MeV. (b) Strain profile used (solid) and energy loss per unit length (dots) and stopping ion profile (dash). See text.

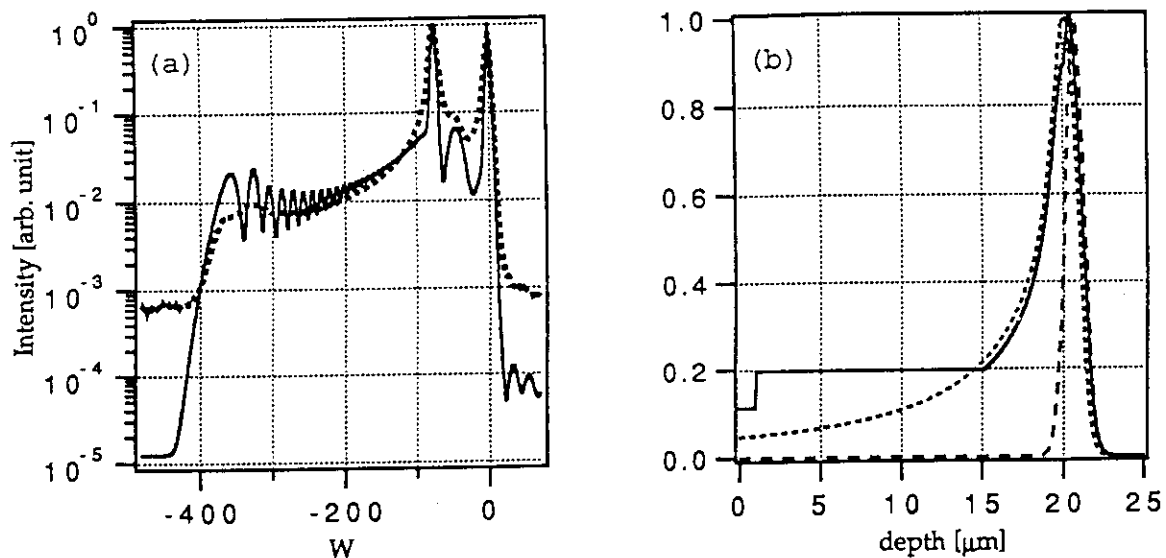


Fig.3. (a) Experimental (dots) and calculated (solid) rocking curve from Si(333) implanted Au^{+14} 1.7×10^{14} [ions/cm²] with 230MeV. (b) Strain profile used (solid) and energy loss per unit length (dots) and stopping ion profile (dash). See text.

magnitude of strain, $\Delta d/d$, decreases. The decrease can be interpreted that crystal atoms escape by the collision of implanted ions. The details of simulation and annealing effect are now in progress.

The authors would like to thank Dr.T.Aruga for his kind guidance and advice to calculate energy loss and stopping ion profiles.

Reference

- 1) H.Wong, N.W.Cheung, P.K.Chu, J.Liu and J.M.Mayer:
Appl.Phys.Lett., 52(1988)1023.
- 2) S.Takagi; J.Phys.Soc. Jpn., 26(1969)1239.
- 3) T.Aruga, K.Nakata and S.Takamura: Nuch.Instr. and Meth.,
B33(1988)748.

2.10 XDT-observation of Dislocations Induced in Si Single Crystal by High Dose Irradiation of Energetic Heavy Ions

Hiroshi TOMIMITSU, *Vittaya AMORNKITBANRUNG, Kazuya AIZAWA,
Satoru OKAYASU and Yukio KAZUMATA.

Dept. Materials Science and Engineering, JAERI; *Dept. Physics,
Faculty of Science, Khon Kaen University, Thailand.

Introduction

The lattice disorder in Si single crystals induced by ion-irradiation has been studied by the X-ray diffraction topography(XDT). Schwuttke et al.¹⁾ have shown that the disorder concentrates at the very thin layer within the stragglings of the ranges of projectiles on the bombardment of Si crystals by 2MeV N, B and P ions, the dose being more than 10^{16} ions/cm², while the upper and lower parts of the specimen crystal separated by the thin layer remain perfect. Further studies by Bönse, Hart and Schwuttke²⁾ and by Bönse and Hart³⁾ found the interference fringes arising from the two perfect regions separated by the thin layer.

One of the present authors^{4, 5)} has also reported that 1)the specimens were macroscopically deformed as a whole, 2)they sustained heavy strains which were concentrated at the boundary between the irradiated- and non-irradiated regions, 3)regularly arrayed systematic fringes were observed within the irradiated area, and 4)the characteristic images of the radiation damage were observed, however, 5)other defect such as crack or dislocation was not observed within the specimen with the dose not more than 10^{16} /cm².

In the present article, a special observation of dislocations induced in the specimen by the O-ion irradiation with the dose as high as 10^{18} /cm² will be reported, which is the first time in the study of ours.

Experimental Procedure

The Si-wafers of Fz-grown single crystal used in the present study are of 001-surface, thickness being about 0.5mm.

The irradiation of 120MeV O⁷⁺-ions in Si crystals was carried out by the Tandem Accelerator of JAERI. The abnormally high dose up to 4.7×10^{18} /cm² was achieved by con-fining the beam-size to around 5mm in diameter. The sample was cooled with liquid nitrogen during the irradiation period.

The topographs were taken with the so-called Lang method using $\text{Mo-K}\alpha$ X-rays from conventional X-ray generator operated at 45kV and 25mA, focus size being of 0.1mm in diameter. The topographs were recorded on ILFORD L4-type nuclear emulsion plates. Topographs were taken with 24 reflections of four kinds, 111, 220, 004 and 224, to identify the Burgers vector.

Results and Discussion

Within the irradiated area on the specimen surface, the cracks were recognized by eyes. In the topographs, further, many dislocation-like images were observed, which were penetrating into the non-irradiated area from the irradiated one. An example of the topograph is shown in Fig.1. They are rather similar to that observed by one of the present authors⁶⁾ in the case of LiF and NaF crystals irradiated by 0.5 MeV protons and by 1.1 MeV N^+ ions.

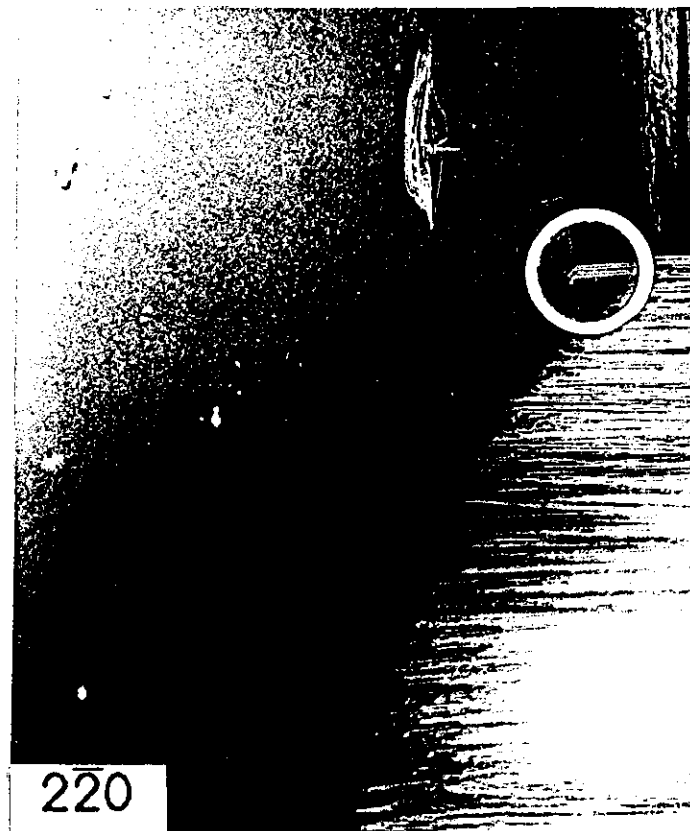


Fig.1 Example of the X-ray topographs
The Burgers vector of the encircled dislocation arrays were analyzed.

We tried to identify the Burgers vector for those dislocation-like defects, from a careful Burgers vector analysis; i.e. the dislocation should be imaged with no-contrast (invisible) or with very low contrast (very faint image) when the value of $\mathbf{b} \cdot \mathbf{g}$ equals to 0, \mathbf{b} meaning the Burgers vector and \mathbf{g} the diffraction vector. The results of the analysis are shown in Table 1.

Table 1. Burgers vector analysis

$ \mathbf{b} \cdot \mathbf{g} $				
Diffraction vector, \mathbf{g}	Burgers vector, \mathbf{b}			Result of Observation*
	[011]	$[\bar{1}21]$	$[\bar{1}31]$	
$\bar{1}11$	2	2	3	○
$11\bar{1}$	0	0	1	△
$\bar{1}\bar{1}1$	0	2	3	○
$\bar{1}1\bar{1}$	2	4	5	○
220	2	2	4	○
$\bar{2}20$	2	6	8	○
$\bar{2}02$	2	4	8	○
$\bar{2}0\bar{2}$	2	0	0	×
$0\bar{2}2$	4	6	8	○
$02\bar{2}$	0	2	4	△
400	0	4	4	○
040	4	8	12	○
$\bar{2}24$	6	6	8	△
$22\bar{4}$	2	2	0	×
$\bar{4}22$	4	2	4	○
$42\bar{2}$	0	2	0	△
$\bar{2}42$	6	8	12	○
$24\bar{2}$	2	4	8	△
$\bar{2}24$	6	10	12	○
$\bar{2}2\bar{4}$	2	2	4	○
$\bar{2}42$	6	12	16	○
$\bar{2}4\bar{2}$	2	8	12	○
$\bar{4}22$	4	10	12	○
$42\bar{2}$	0	6	8	○

* ○=visible, △=faintly visible, ×=invisible.

The conclusion of the analysis is as following;

- 1) $[011]$ is less possible, because it showed contradictions in the topographs taken with $1\bar{1}1$, 400 , $\bar{4}2\bar{2}$ (to be visible) and with $\bar{2}0\bar{2}$, $22\bar{4}$ (to be invisible).
- 2) $[\bar{1}21]$ seems to be rather possible, although it showed small contradiction in the topograph taken with $22\bar{4}$ (to be invisible).
- 3) $[\bar{1}31]$ apparently seems more possible, because it agreed well with $\bar{2}0\bar{2}$, $22\bar{4}$ (invisible). The $[\bar{1}31]$ -type Burgers vector is, however, thought abnormal in the Si crystal.

The Burgers vector of the dislocation-like defects was, thus, concluded to be $[\bar{1}21]$ in the present study. so the further sample preparation is necessary to clarify the Burgers vector.

Conclusions

Cracks were observed by eyes on the specimen surface with the O-ion irradiation of the high dose of $4.7 \times 10^{18}/\text{cm}^2$. By X-ray diffraction topography, furthermore, dislocation-like images were observed, whose Burgers vector was preliminarily concluded to be $[\bar{1}21]$.

Aknowledgement

The authors are much indebted to Dr.T.Abe of Shin-Etsu Semiconductors Co. for his kind offering the Si-wafers used in this study.

References

- 1) G.H.Schwuttke, K.Brack, E.E.Gardner and H.M.DeAngelis: Proc.Santa Fe Conf. Radiation Effects in Semiconductors, ed.F.Vook, (Plenum Press, N.Y., 1968), p.406.
- 2) U.Bonse and M.Hart and G.H.Schwuttke: Phys.Status Solidi **33**(1969), 361.
- 3) U.Bonse and M.Hart: Phys.Status Solidi **33**(1969), 351.
- 4) H.Tomimitsu: Jpn.J.Appl.Phys. **22**(1983), L674.
- 5) H.Tomimitsu: from "JAERI TANDEM, LINAC & V.D.G. Annual report 1982" to ibid 1987.
- 6) H.Tomimitsu: J.Phys.Soc.Japan **38**(1975)905.

2.11 Photoacoustic Spectroscopic Studies on Radiation Damage of Li_4SiO_4 and $\text{Li}_{3.7}\text{Al}_{0.1}\text{SiO}_4$

Tetsuya NAKAZAWA, Kenji NODA, Yosinobu ISHII, Hisayuki MATSUI*,
Naoki IGAWA, Dieter VOLLATH**, Hideo OHNO and Hitoshi WATANABE

Department of Materials Science and Engineering, JAERI,

*Faculty of Engineering, Nagoya University,

**Kernforschungszentrum Karlsruhe GmbH, Institut für Material
und Festkörperforschung III,

1. Introduction

Li_4SiO_4 is a candidate breeder material for D-T fusion reactors. $\text{Li}_{3.7}\text{Al}_{0.1}\text{SiO}_4$ was recently developed to improve tritium release performance of Li_4SiO_4 especially at low temperatures. The defects, introduced in these materials under the fusion blanket environment, will give changes of the structure which will affect tritium release behavior, thermal and mechanical properties.

In this study, the changes of structure in Li_4SiO_4 and $\text{Li}_{3.7}\text{Al}_{0.1}\text{SiO}_4$ irradiated with oxygen ions were investigated using Fourier transform infrared photo-acoustic spectroscopy (FT-IR PAS) to obtain the information of radiation damage due to high energy neutrons.

2. Experimental

Samples used were thin disks (8-9 mm in diameter, 0.4-1 mm in thickness) obtained by cutting the sintered rods of Li_4SiO_4 and $\text{Li}_{3.7}\text{Al}_{0.1}\text{SiO}_4$. Ion irradiations for the samples were carried out at the ambient temperature with 120 MeV oxygen ions in an irradiation vacuum chamber attached to a tandem accelerator at JAERI. The samples irradiated were measured at room temperature with a Perkin-Elmer model 1760X FT-IR spectrometer.

3. Results and Discussion

The FT-IR PAS spectra of as-synthesized Li_4SiO_4 and $\text{Li}_{3.7}\text{Al}_{0.1}\text{SiO}_4$ samples are shown in fig. 1. The band at about 1000 cm^{-1} has been interpreted as one of the two active bands of the SiO_4 -tetrahedra (ref. 1-3). The active band has been also observed at $944\text{-}894\text{ cm}^{-1}$ as one of the vibrations of isolated SiO_4 -tetrahedra in ZrSiO_4 (ref. 1). Thus, it is reasonable to assume that the

bands at 944 and 870 cm^{-1} observed in the spectrum of Li_4SiO_4 are caused by the vibrations of SiO_4 -tetrahedra. In the spectrum of $\text{Li}_{3.7}\text{Al}_{0.1}\text{SiO}_4$, the bands for SiO_4 -tetrahedra are observed at 928 and 860 cm^{-1} . It was observed that the absorption bands for SiO_4 -tetrahedra shifted to the lower frequency side in case of $\text{Li}_{3.7}\text{Al}_{0.1}\text{SiO}_4$. The shifts of the bands were thought to be caused by doping Al.

In fig. 2, the FT-IR PAS spectra of Li_4SiO_4 irradiated to the fluences of 5.01×10^{19} and 1.65×10^{20} ions/ m^2 are shown. The slight shifts of absorption bands for SiO_4 -tetrahedra to the lower frequency side are observed with the fluence. In addition to these, the band at 1042 cm^{-1} and the shoulders at 1232 and 1180 cm^{-1} were observed to become prominent with fluence. Some silicon oxides have been found as one of the radiolysis products in Li_4SiO_4 (ref. 4). In the infrared spectra of some kind of silica, the bands at about 1200 and 1100 cm^{-1} have been assigned as the Si-O stretching and the chain-type Si-O-Si vibration, respectively (refs. 1-3). It was considered that the prominent band observed at 1042 cm^{-1} in fig. 2 can be attributed to Si-O-Si vibration. The shoulders at 1232 and 1180 cm^{-1} were thought to be assigned as Si-O stretching. It was also observed for $\text{Li}_{3.7}\text{Al}_{0.1}\text{SiO}_4$ irradiated to the fluences of 9.63×10^{18} and 2.46×10^{20} ions/ m^2 that the absorption bands for SiO_4 -tetrahedra slightly shifted to the lower frequency side with fluence. Furthermore, it was revealed that the absorption band at 1031 cm^{-1} due to the Si-O-Si bond and the shoulders at 1230 cm^{-1} caused by the Si-O stretching grew with fluence.

The FT-IR PAS spectra of both Li_4SiO_4 and $\text{Li}_{3.7}\text{Al}_{0.1}\text{SiO}_4$ were recorded at room temperature after annealing at 773 K for 30 min. Fig. 3 shows the recovery behavior of the FT-IR PAS spectra of Li_4SiO_4 irradiated to 1.65×10^{20} ions/ m^2 . The intensity of remarkable band at 1042 cm^{-1} due to the Si-O-Si bond vibration was decreased by annealing. Furthermore, the shoulder at about 1200 cm^{-1} due to the Si-O stretching vanished by annealing. However, a complete recovering of irradiation damages on chemical structure was not observed at the annealing temperature of 773 K. In the FT-IR PAS spectra of $\text{Li}_{3.7}\text{Al}_{0.1}\text{SiO}_4$ in annealing experiments, the similar phenomena were observed.

The prominent bands for SiO_4 -tetrahedra in Li_4SiO_4 shifted to the lower frequency side by doping Al which has three electrons to bind the oxygen atoms (fig. 1). This means that the Si-O bond in $\text{Li}_{3.7}\text{Al}_{0.1}\text{SiO}_4$ is weaker than that in Li_4SiO_4 . In other words, the binding strength between the aluminum ions and the oxygen ions seems to be stronger than that between the lithium ions and

the oxygen ions. During irradiation, lithium, oxygen, aluminum and silicon ions in Li_4SiO_4 and $\text{Li}_{3.7}\text{Al}_{0.1}\text{SiO}_4$ are displaced. The displacement causes the introduction of the lithium ion vacancies and interstitials, which are considered to form clusters, i.e., colloidal lithium metals (ref. 4), and the decompositions of the SiO_4 -tetrahedra. Such irradiation effects are reflected in the changes of vibration mode in SiO_4 -tetrahedra on the PAS spectra. In fact, the prominent bands for SiO_4 -tetrahedra slightly shifted to the lower frequency side with fluence in the PAS spectra. The appearances of the new phase due to the decomposition of SiO_4 -tetrahedra with the irradiation were also observed on the PAS spectra. The new phase having the Si-O-Si (1042-1031 cm^{-1}) and Si-O (1232-1180 cm^{-1}) stretching modes in the infrared activity are thought to be some silicates such as SiO_2 and SiO_3 -chain (refs. 1-4). Judging from the FT-IR PAS spectra with fluence, the new phase, which is formed with the decompositions by displacements due to the irradiation, is considered to precipitate in Li_4SiO_4 polycrystalline containing many irradiation defects (ref. 5).

Temperature of breeders in the blanket region during operation is expected to be in the range 583 to 1223 K for Li_4SiO_4 (ref. 6). However, the FT-IR PAS spectra at the annealing temperature of 773 K did not show the sufficient recovery in irradiated Li_4SiO_4 and $\text{Li}_{3.7}\text{Al}_{0.1}\text{SiO}_4$. It is, thus, supposed from the results that the colloidal lithium metals, which is not recovered up to 700 K (ref. 5), and the decomposition formed by the irradiation will be accumulated in low temperature region of the breeder blanket during the irradiations. These radiation damage in Li_4SiO_4 and $\text{Li}_{3.7}\text{Al}_{0.1}\text{SiO}_4$ is thought to be one of dominant factors affecting the various materials properties.

The FT-IR PAS spectra of Li_4SiO_4 and $\text{Li}_{3.7}\text{Al}_{0.1}\text{SiO}_4$ irradiated in the fluence range 10^{18} to 10^{20} ions/ m^2 gave the information of new phases due to the decomposition of SiO_4 -tetrahedra with the irradiation. However, further studies of radiation damage in Li_4SiO_4 and $\text{Li}_{3.7}\text{Al}_{0.1}\text{SiO}_4$, especially TEM observations of damage microstructure, are required to obtain complete information on the radiation damage in the materials.

References

- 1) F. Matossi, J. Chem. Phys., 17 (1949) 679.
- 2) R. Hanna, J. Am. Ceram. Soc., 48 (1965) 595.
- 3) I. Simon and H. O. McMahon, J. Am. Ceram. Soc., 36 (1953) 160.

- 4) J. E. Tiliks, G. k. Kizane, A. A. Supe, A. A. Abramkovs, J. J. Tiliks and V. G. Vasiljev, Fusion Engrg. Des., 17 (1991) 17.
- 5) K. Noda, K. Uchida, T. Tanifuji and S. Nasu, J. Nucl. Mater., 91 (1980) 234.
- 6) C. E. Johnson, K. R. Kummerer and E. Roth, J. Nucl. Mater., 155-157 (1988) 188.

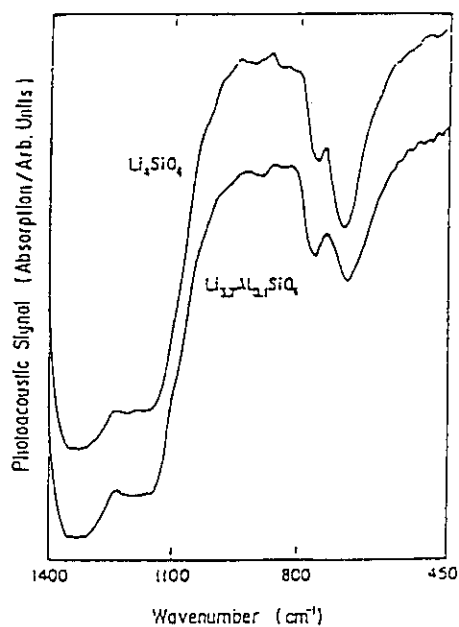


Fig. 1 FT-IR PAS spectra of Li_4SiO_4 (upper) and $\text{Li}_{3.7}\text{Al}_{0.1}\text{SiO}_4$ (lower).

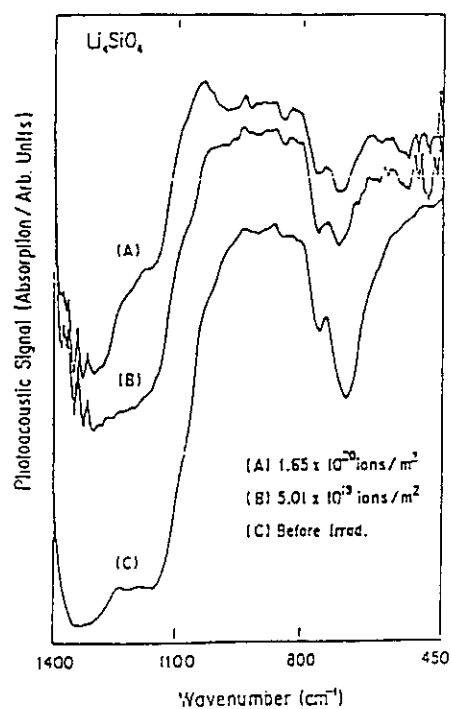


Fig. 2 FT-IR PAS spectra of Li_4SiO_4 irradiated to various fluences with 120 MeV oxygen ions.

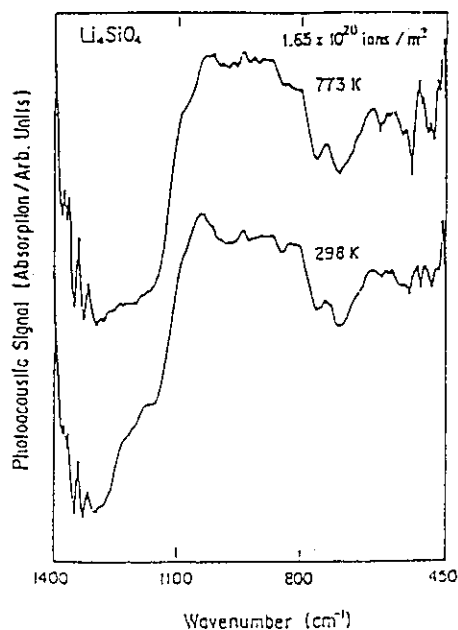


Fig. 3 Recovery behavior of FT-IR PAS spectra of Li_4SiO_4 irradiated to 1.65×10^{20} ions/m² with 120 MeV oxygen ions.

2.12 Change of Surface Morphology in ThO_2 and $(\text{Th,U})\text{O}_2$ Irradiated with 100 MeV Iodine Ions

Mitsuo AKABORI, Kimio HAYASHI, Hironobu KIKUCHI,
Akinori ITOH and Kousaku FUKUDA

Department of Fuels and Materials Research, JAERI

1. Introduction

In order to clarify radiation effects in actinide oxide fuels, we have continued a series of ion-irradiation experiments. In a previous study¹⁾, we reported on the radiation effects of UO_2 pellets irradiated with 100 MeV I, Br and O ions. In the present work, thorium-based oxides, ThO_2 and $(\text{Th,U})\text{O}_2$, were irradiated with high-energy iodine and oxygen ions. In this report, we deals with the results on surface observations of the iodine-irradiated ones.

2. Experimental procedures

Sintered ThO_2 and $(\text{Th,U})\text{O}_2$ discs of 10-13 mm in diameter, 0.5-1.0 mm in thickness and 92-96 %TD (theoretical density) were used in this study. Compositions of $(\text{Th,U})\text{O}_2$ were 20, 30 and 40 mol% UO_2 . Irradiation of I^{+7} and O^{+6} ions with an energy of 100 MeV was performed with the 20 MV JAERI tandem accelerator in a vacuum of about 10^{-8} torr at a temperature below 573 K. The ion dose irradiated was in the ranges of 1×10^{18} - 5×10^{19} ions/ m^2 for I ion and 2×10^{19} - 1×10^{21} ions/ cm^2 for O ion. After irradiation, the samples were inspected with an optical microscope, a secondary electron microscope (SEM) and an electron-probe micro-analyzer (EPMA).

3. Results

Iodine-irradiated spots of about 5 mm in diameter were easily visible in all the discs. In the case of ThO_2 discs, the I-irradiation resulted in a blue ThO_2 . There was also a change in the shade of color over the spots, suggesting that the irradiation dose was not uniform over the irradiated area.

As shown in Figure 1, which gives SEM micrographs of the surfaces for the ThO_2 and $\text{Th}_{0.6}\text{U}_{0.4}\text{O}_2$ discs irradiated to 4.5×10^{19} ions/ m^2 , three types of changes in the surface morphology, namely, surface smoothing, crater and protrusion formations, are observable. This figure indicates that the surface smoothing occurred to the degree that grain boundaries, pores and polishing

scratches observed in the unirradiated area are barely visible at the irradiated area.

Figure 2 shows SEM cross-sections of the ThO_2 disc irradiated to 2.3×10^{19} ions/ m^2 . They were observed after polishing and etching with nitric acid containing sodium fluoride. The surface region of 2-3 μm in thickness seems to have a sponge-like structure. As seen in fig.2(b), the spongy structure is likely to be consisted of fine grains or sub-grains. The initial grain size of the ThO_2 was estimated to be above about 10 μm . Therefore the result indicates that the initial large grains at the near-surface may subdivide into smaller grains of less than about 1 μm in grain size during the ion irradiation. The similar phenomenon of forming the surface microstructure has been observed in ion-implanted²⁾ and high-burnup^{3,4)} UO_2 .

The EPMA was used to examine the protrusion observed in the ThO_2 and $(\text{Th,U})\text{O}_2$ discs. It was found that the protrusion was of the same composition as the bulks for both the discs. Furthermore, the shape of protrusion, just like worms, appears to be unique, as compared with blisters which are usually formed on surfaces of metals implanted with gaseous ions, such as hydrogen and helium, and of which the shape is like a dome. Figure 3 shows a highly magnified SEM micrograph of the ThO_2 protrusion, of which the near-surface region was fractured during handling. The protrusion is formed from ThO_2 of about 1 μm in thickness and its inside appears to be vacant. Also, the ThO_2 foil appears to be composed of a number of fine grains.

Studies on the lattice growth induced by the iodine-irradiation using a micro-beamed X-ray diffraction technique and the radiation effects in the thorium-based oxides irradiated with high-energy oxygen ions are now in progress.

References

- 1) K.Hayashi, H.Kikuchi, T.Shiratori, S.Kashimura, M.Akabori and K.Fukuda: JAERI-M 92-124, pp.71-74(1992).
- 2) H.J.Matzke and A.Turos, J. Nucl. Mater. 188(1992)285.
- 3) C.T.Walker, T.Kaneyama, S.Kitajima and M.Kinoshita: J. Nucl. Mater. 188(1992)73.
- 4) L.E.Thomas, C.E.Beyer and L.A.Charlot: J. Nucl. Mater. 188(1992)80.

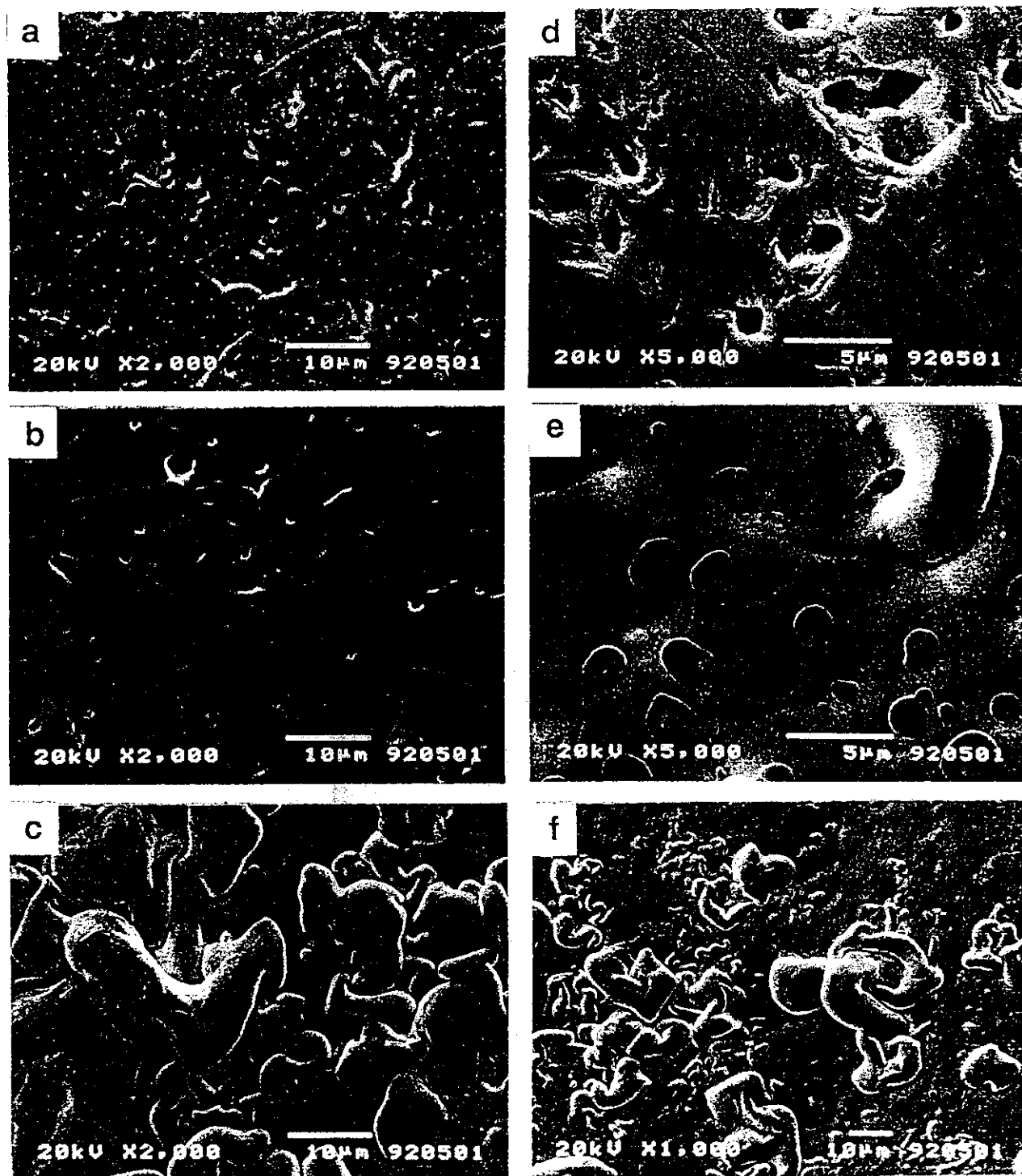


Fig.1 SEM micrographs of the ThO_2 and $(\text{Th,U})\text{O}_2$ surfaces irradiated with 100 MeV- I^{7+} ions to a dose of 4.5×10^{19} ions/ m^2 . Left- ThO_2 and right- $\text{Th}_{0.6}\text{U}_{0.4}\text{O}_2$; a)&d) unirradiated areas; b)&e) outer regions of irradiated areas; c)&f) center regions of irradiated areas.

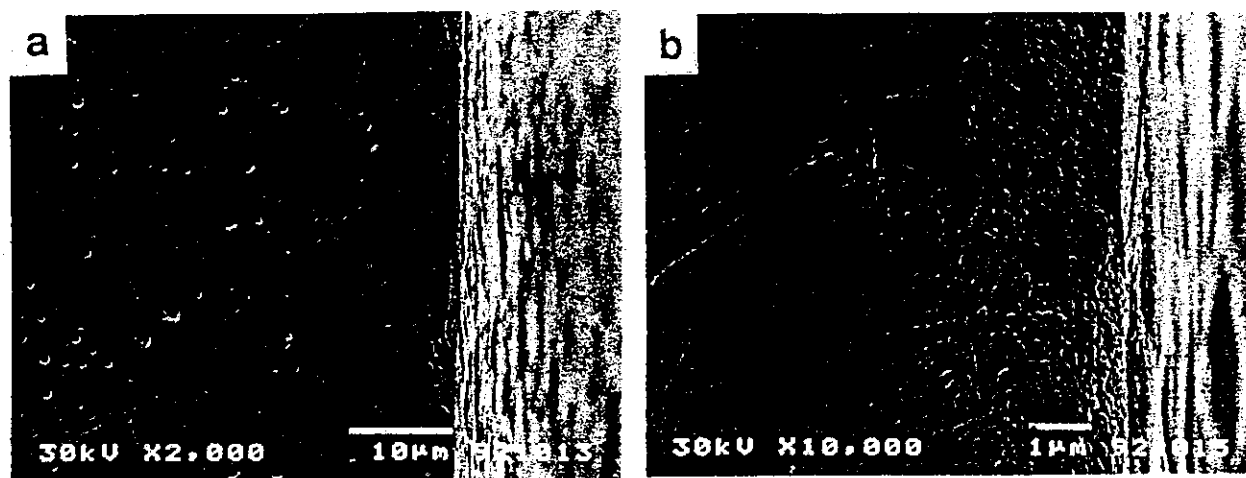


Fig.2 Cross-section SEM micrographs of the ThO_2 irradiated to a dose of 2.3×10^{19} ions/ m^2 . a) shows microstructures of the near-surface region, spongy structure and a line corresponding to the end of the projected range of 100 MeV-I ions. b) shows high-magnificated feature of the spongy structure.

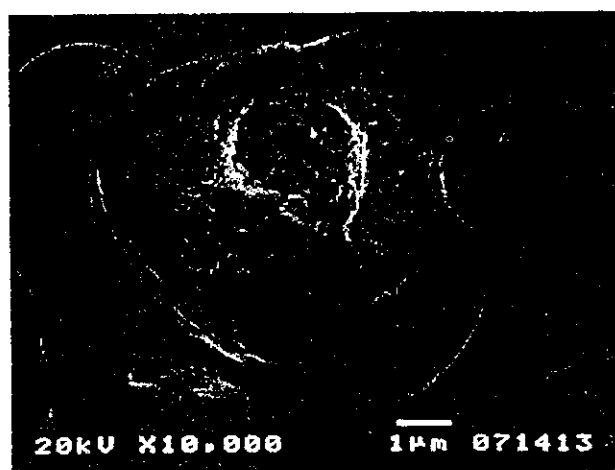


Fig.3 SEM micrograph of a fractured protrusion observed at the ThO_2 irradiated to a dose of 4.5×10^{19} ions/ m^2 .

2.13 Radiation Damage of UO_2 by 100 MeV Iodine, Nickel and Chlorine Ions

Kimio HAYASHI, Hironobu KIKUCHI, Tetsuo SHIRATORI
and Kousaku FUKUDA

Department of Fuels and Materials Research, JAERI

1. Introduction

Uranium dioxide (UO_2) has been used as the fuel of nuclear reactors including light water reactors. At high burnups exceeding 50–70 GWd/t, changes in microstructure of UO_2 matrix have been observed recently at the peripheral region of the fuel pellet. The changes consist of loss of definable grain boundaries and increase in porosity¹⁾, which are thought to be due to radiation damage by fission fragments.

The present authors started a research in radiation damage of UO_2 by high-energy ion irradiation using the TANDEM accelerator. And preliminary results on 100 MeV iodine irradiation were published earlier²⁾. In the present study, UO_2 specimens were irradiated with lighter ion species, i.e., nickel and chlorine. The purpose is to study the relative importance of nuclear and electronic energy depositions in contribution to the microstructural changes.

2. Experimental

In order to obtain well-defined data, some improvements were made in experimental methods, compared with the previous iodine irradiation²⁾. The main items are i) annealing of specimens after polishing, ii) measurement of the irradiation temperature by a pyrometer, and iii) change of the masking material from Pb to Mo in X-ray diffractometry.

2.1 Specimens

Sintered UO_2 discs sliced from fuel pellets (10.4 mm in diameter and $\text{O/U}=2.00^3)$ were polished by emery paper and diamond paste, as in the previous experiment²⁾. Subsequently, the specimens were annealed in flowing Ar-4\%H_2 mixture gas at 1500°C for 2 hours or longer, so as to remove the surface damage introduced by the polishing⁴⁾.

2.2 Irradiation

Irradiation was made at ambient temperature with 100 MeV Ni^{6+} and Cl^{8+} ions using the TANDEM accelerator at JAERI. The rear side of the target was cooled by water kept at 20°C, and the temperature at the beam-incidence side surface was monitored by an infrared pyrometer (PbS sensor, model IR-AP, Chino Ltd.). The surface temperature was lower than 200°C, which is the lower detection limit of this pyrometer.

2.3 Post-irradiation analysis

The irradiated specimens were analyzed by an X-ray diffraction apparatus, RU-200B of Rigaku Ltd., with a Cu-K alpha beam. The specimens were masked with a molybdenum plate (0.2 mm thick) having a 2 mm hole, to limit the X-ray analysis area within the ion beam spot (5 mm in diameter). The lattice parameter was obtained by the least squares fitting of six diffraction lines between 77 and 140° in 2θ .

3. Results and Discussion

3.1 Effect of polishing on lattice parameter change

Before irradiation, as-polished and annealed specimens were analyzed by X-ray diffractometry. The results of the lattice parameter (L) are as follows.

(A) as-polished : $L_1 = 0.54711 \pm 0.00001$ nm (3 samples)

(B) annealed : $L_2 = 0.54710 \pm 0.00001$ nm (4 samples)

These two values agree very well ($L_1/L_2=1.00002$). Comparing the results obtained by Matzke⁴⁾ using the Rutherford backscattering technique, the surface damage introduced by the polishing is thought to have remained only at the near surface (presumably $<0.1 \mu\text{m}$ in depth). And the information obtained by diffraction of the X-ray, which penetrates UO_2 by ca. $2 \mu\text{m}$, is considered to be hardly disturbed by the polishing.

3.2 Analysis of irradiation results

The lattice parameter change is plotted as a function of Ni ion fluence in Fig.1. First, the change increases with the fluence, and then tends to saturate at ca. +0.3%. As shown in Fig.1, the fluence dependency is similar to that for the previous iodine irradiation, while the saturation fluence is different approximately by an order of magnitude.

In Fig.2, the lattice parameter changes are plotted as a function of dpa (displacement per uranium atom). These dpa values were determined as follows.

(a) The nuclear energy deposition was calculated by EDEPJR-87 code⁵⁾,

(b) the energy partition to uranium and oxygen atoms in UO_2 was derived from the calculation by Soullard⁶⁾, and

(c) displacement energies of 40 and 20 eV were assumed for U and O atoms in UO_2 ⁶⁾.

Figure 2 indicates that the damage effect at the surface can be expressed comprehensively by the dpa values, namely the normalized nuclear energy depositions. This result suggests that as far as the lattice parameter is concerned, the damage effect in UO_2 is mainly due to the nuclear energy deposition.

Similar analysis is to be made on the chlorine irradiation results, while X-ray diffractometry of the chlorine-irradiated samples are under way.

As further works, the following experiments are under consideration in order to study the effect of the electronic energy deposition on properties of UO_2 .

- (i) To get a high-energy ion beam of light species (e.g. oxygen) by the TANDEM accelerator, and to make it penetrate a thin target of UO_2 . The property change due mainly to electronic energy deposition will be observed.
- (ii) To irradiate first the specimen with heavy ions (e.g. iodine) and to irradiate it subsequently with high energy light ions. The surface change caused first by the nuclear energy deposition will be modified by the electronic energy deposition effect in the second irradiation.

References

- 1) J.O.Barner, M.E.Cunningham, M.D.Freshley and D.D.Lanning, Proc. Intern. Topical Mtg. on LWR Fuel Performance (Avignon, France, April 21-24, 1991) pp.538-548.
- 2) K.Hayashi et al., JAERI-M 92-124 (1992) pp.71-74.
- 3) M.Yoneyama et al., JAERI-M 92-118 (1992) p.13.
- 4) H.J.Matzke and A.Turos, J. Nucl. Mater. **114** (1983) 349-352.
- 5) T.Aruga, K.Nakata and S.Takamura, Nucl. Inst. Meth. in Phys. Research **B33** (1988) 748-751.
- 6) J.Soullard and A.Alamo, Rad. Effects **38** (1978) 133-139.

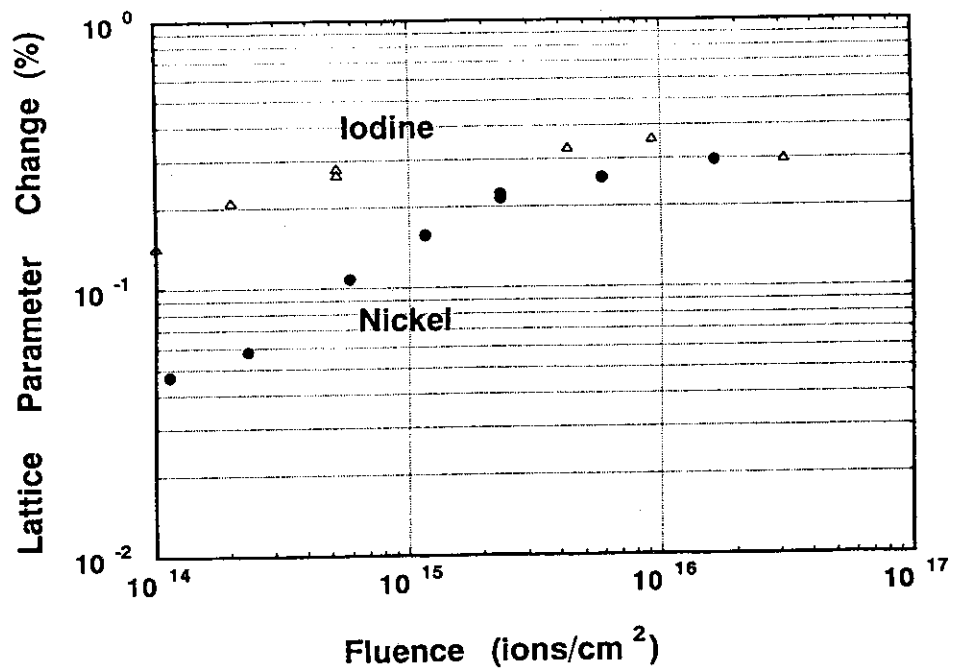


Fig.1 Lattice parameter change of UO_2 by 100 MeV Ni and I ion irradiation, expressed as a function of fluence.

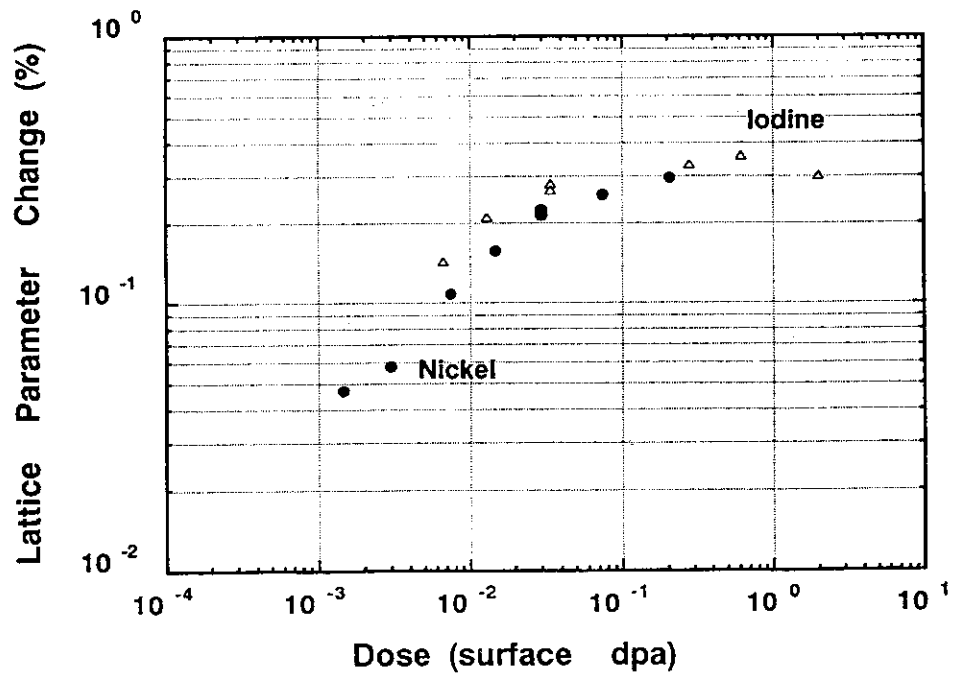


Fig.2 Lattice parameter change of UO_2 by 100 MeV Ni and I ion irradiation, expressed as a function of displacement per U-atom (dpa) at the incident surface.

2.14 Elution of Injected Ions in Etched Polyimide

Yoshihide KOMAKI, Niro ISHIKAWA, Tsutomu SAKURAI,
Katsutoshi FURUKAWA, and Yasuyo MATSUMOTO*.

Department of chemistry and fuel research, JAERI, Tokai.

*Sumitomo Electric Industries, Co. Ltd., Osaka

Introduction:

A figure emerged by etching polyimide film irradiated through a mask of copper plate of a pattern by heavy ions. The channel in the figure shows to have a given depth and smooth edge. On an etching condition, the etched patterns in the figure were found to be clear for irradiation by heavier ions and the NaClO solution around 60°C was appropriate in etching polyimide¹⁾.

Heavy ions injected over the mask into the thick polyimide film remain at a depth and elute into the etching solution with fragments of the polyimide. But, it is undeniable that some ions may remain in the etched polyimide. When the technologies forming microchannels and microholes in the polymer by the heavy ion irradiation and etching are applied to fabricating parts of electronics, the residual ions are fear to affect seriously the electrical characteristics in the polymer. But, it is impossible at present that each residual ion is counted separately. Then, the elution behaviour of injected ions has been examined during etching by using the activation analysis, which shows the heighest sensitivity at present.

Experimental

Injected ions in thick polyimide were radioanalytically determined for each step of etching. The ions suitable for activation analysis needed to be injected, and ^{45}Sc was selected because of the large thermal cross section ($\sigma:13\text{b}$), long half life of generated ^{46}Sc (T:84d), easy measurement of γ -ray (889 KeV (100%)), and irradiation condition in tandem accelerator.

180 MeV $^{45}\text{Sc}^{12+}$ of $4 \times 10^{12}/\text{cm}^2$ were injected into 30 μm thick polyimide up to about 20 μm depth through the stacked polymers. The radioactivity of the 1 cm^2 sample irradiated by the thermal neutron fluence, $3.1 \times 10^{19} \text{nvt}$ was measured by Ge-detector after cooling for 48 days

and the change in weight after etching in 10%NaClO solution at 60°C. The samples irradiated by Br ion were examined for etching behavior, too.

Results and Discussion

Injected ions in the film are considered to elute with the etched polyimide little by little. On the other hand, the only irradiated region of polyimide must dissolve quickly, followed by the slow dissolution of the unirradiated polyimide. Consequently the amount of residual ions in the etched polyimide is estimated from the activity of the residual polyimide which remains after quickly etching.

Figure 1 and Fig. 2 show the vertical sections of the unetched polyimide film injected by Br ion and of the film etched for some period. The irradiated polyimide shows the preferential dissolution during etching.

Fig. 3 is γ -ray spectra of the thermal neutron irradiated polyimide injected by ^{45}Sc ion, the upper curve the spectra before etching and the lower after 3h etching. They indicate γ -ray of ^{46}Sc at 889 KeV and the decrease of the intensity during etching. The virgin resin contained ^{45}Sc a little, too.

Figure 4 shows the changes in weight of the etched polyimide containing ^{46}Sc and in the residual radioactivity against etching time. After etching for about 3.4h the irradiated polyimide is eluted out followed by the slow dissolution of only bulk polyimide. Each dissolution rate at A and C on the curves was found to be about 5.8 and 0.1 $\mu\text{m/h}$ and injected heavy ions not to elute until more than 25% of the irradiated polyimide dissolved. As $4 \times 10^{12}/\text{cm}^2$ heavy ions indicates the density to be more than a track per 10 nm^2 and almost overlappes, the dissolution rate in such a volume will be shown larger than that of a track. At B crossed by the dissolution curves of the irradiated polyimide(A) and the bulk (C), the only surface of the unirradiated polyimide was considered to remain, but the radioactivity was yet detected. Radioactivity at B indicates 0.7 (dps), 0.2 at 4h etching and ultimately zero at 5h. Table 1 shows the radioactivity in the irradiated polyimide deducted by that of the unirradiated polyimide and the weight at the various etching periods. When microchannels and microholes are formed in the polyimide by the heavy ion irradiation of $\sim 10^{12}\text{p/cm}^2$ followed by etching, etching for longer than the calculated period by 1.5h emerges the slightly deeper channels and holes than the original range of ion($\sim 51\mu\text{m}$), but indicates the residual ions per the injected ones to be below than the limit of detection.

Reference

- 1) Y. Matsumoto, Y. Matsuura, Y. Hibino, K. Iwata, Y. Komaki, N. Ishikawa, T. Sakurai, and E. Tachikawa., Proc. Int. Conf. on Evolution in Beam Appli., Takasaki (1991) 639

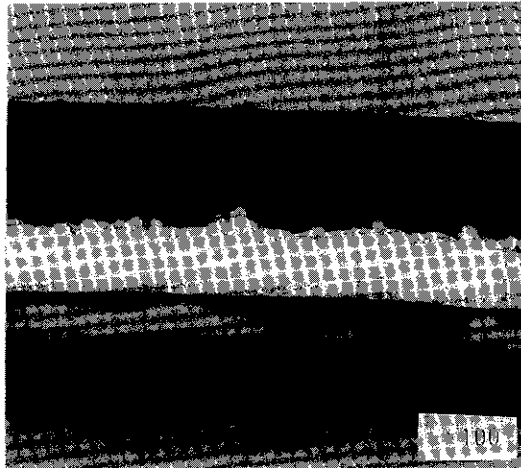


Fig.1 Vertical section of un-etched polyimide irradiated by Br ion

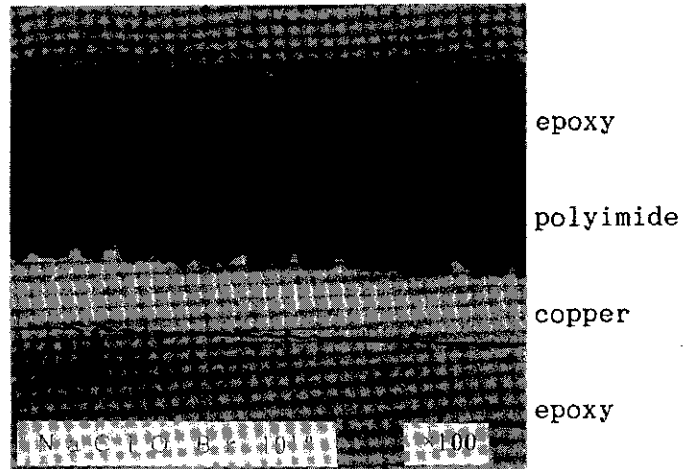


Fig. 2 Vertical section of etched polyimide irradiated by Br ion

Table 1 Residual activity of ^{46}Sc in polyimide at various etching periods

Polyimide	10%NaClO, 60°C		Activity (^{46}Sc) (dps) _t
	Etching time (h)	Weight (g) $\times 10^{-3}$	
No. 1	0	2.63	10.4(0.07)
2	1	2.23	10.7(0.07)
3	2	1.56	6.55(0.06)
4	3	1.07	1.46(0.03)
5	4	0.83	0.33(0.01)
6	5	0.66	-0.03
7	6	0.54	-0.02

Activity of ^{46}Sc in virgin polyimide is 42(dps/g)_o.
(0.07) is the error.

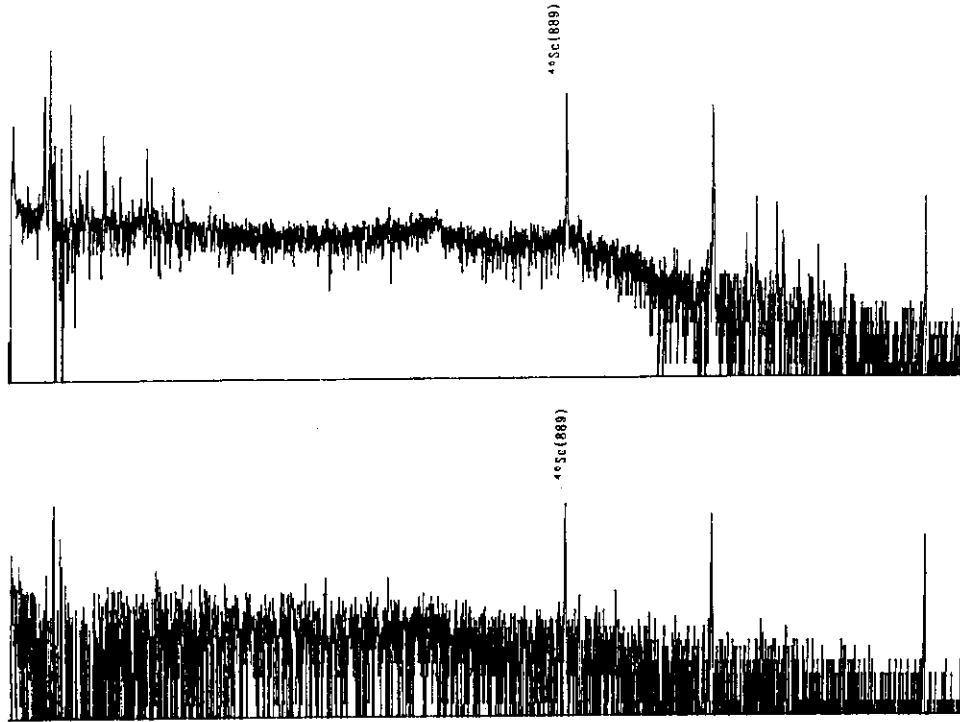


Fig. 3 γ -ray spectra of Sc ion irradiated polyimide
 upper: prior to etching
 lower: after 3h etching

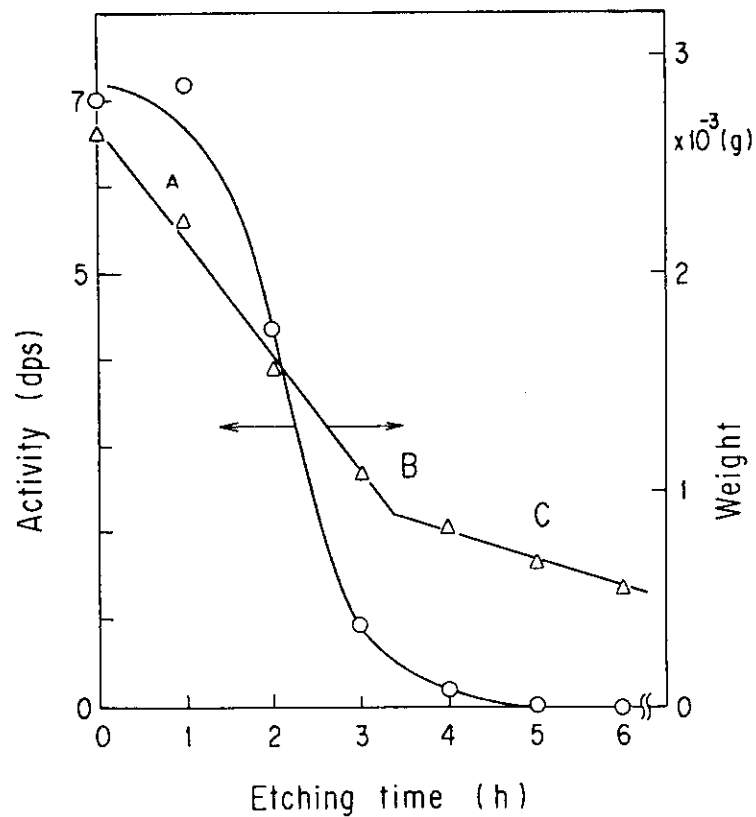


Fig. 4 Change in weight and radioactivity of polyimide
 injected by Sc ion to etching time

2.15 Mechanism of Single Event Effect in Power MOSFETs and CMOS ICs

Isamu NASHIYAMA, Toshio HIRAO, Hideshi YASUDA*,
Hiroshi TAKADA*, Toshinobu SASA*, Tadaaki KUROSAKI**,
Sumio MATSUDA**, Satoshi KUBOYAMA**, Takashi TAMURA**,
Yosuke SHIMANO**, Tooru KANNO**, Jiro OHYA***,
Takayuki ISHII***, and Yasuhiro YOSHIOKA***

Department of Material Development, JAERI,

*Department of Reactor Engineering, JAERI,

**Parts and Material Laboratory, NASDA

***Ryoei Technica Corp.

ABSTRACT

Power MOSFETs and CMOS ICs are important devices for power switching and digital processing respectively. However, they have a possible catastrophic failure mode known as SEB(single event burnout) / SEL(single event latch-up) triggered upon incidence of high-energy heavy ions. This is an important phenomenon to be considered in space electronic applications.

An outline of mechanism for SEB has been examined experimentally by a new measurement system in the previous work ¹⁾. In this paper, we discuss the detailed mechanism of SEB which was analyzed by a numerical simulation as compared with the experimental data using heavy ion beams from the tandem accelerator. SEB hardness of improved power MOSFETs has been also demonstrated.

EPICS SPECTRA

To study the SEB mechanism, collected charge spectra in power MOSFET was measured by a pulse-height measurement system called EPICS (Energetic Particle Induced Charge Spectroscopy). The EPICS has a charge-sensitive amplifier (CSA) with dynamic range over 100dB and a logarithmic converter. Typical EPICS spectra are shown in Fig.1 ¹⁾. It has been already identified that the 1st and 2nd peaks correspond to the collected charge from a drain/p⁺ junction and the injected charge from a source junction respectively.

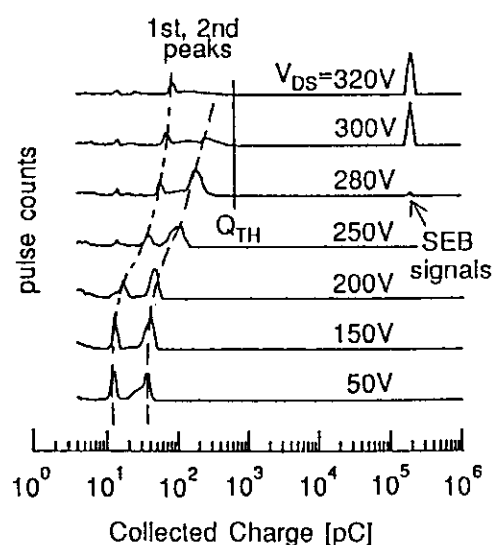


Fig.1. Typical EPICS Spectra ¹⁾

EXPERIMENTS

In the previous work, power MOSFETs and a test structure were exposed to mono-energetic ions using a tandem van-de-graaff accelerator at JAERI. The incident ions were 140MeV Si, 200MeV Ni, and 133MeV Br. The sample power MOSFET was commercial type which had 500V of rated BV_{DS} and 12A of I_D . The test structure had diode construction only and no parasitic transistor which was fabricated with the same photo-mask set and process conditions for power MOSFET without source diffusion process.

Table 1. Characteristics of irradiated ions.

Element Symbol	Energy [MeV]	LET [Mev/(mg/cm ²)]	Range [μm]
¹² C	105	1.4	200
¹² C	77	1.7	120
¹⁷ Cl	150	13	43
²⁸ Ni	200	30	32

Since there is a discrepancy that the 2nd peak is too sharp as seen in Fig.1 in contrast with previously proposed model ²⁻⁴⁾, another SEB model is proposed with an analysis based on a numerical simulation as compared with experimental data this year. Several kinds of ions and samples were also used to identify the nuclear reactions and to confirm Q_{TH} attribute to a specific device design. Characteristics of irradiated ions are shown in Table 1.

RESULTS AND DISCUSSION

Although two peaks shown in Fig.1 were observed for power MOSFET, only 1st peak was observed for the test structure. The 1st peak was identified as the collected charge multiplied by the avalanche effect with in the electric field of the drain/ p^+ junction because the test structure has this junction only. Therefore, the 2nd peak for power MOSFETs indicates the injected charge from the source electrode by the amplification effect of the activated parasitic bipolar transistor. In accordance with previously proposed model ²⁻⁴⁾, the 2nd peak should be broad and continuous with the 1st peak because the value of the voltage drop varies with the position of an ion track in the p^+ layer. The shape of the experimentally observed 2nd peak does not supports this model. Therefore, new mechanism by vertical current flow along the ion track was proposed ¹⁾. We propose a mechanism by which the potential redistribution by the plasma column directly activates the parasitic bipolar transistor. A two dimensional computer simulation for power MOSFET by the VENUS-3D ⁵⁾ is shown in Fig.2. The result obviously indicates that the source/ p^+ junction can be forward biased with voltage drop ΔV_p of p^+ layer by the plasma column and subsequently electrons can be injected from the source electrode. Because the 1st and the 2nd peak correspond directly to the integrated base current and emitter current respectively, the distance between the 1st and the 2nd peak represents the current gain of the parasitic bipolar transistor. It is apparent that highly doped p^+ layer will reduce the ΔV_p and the distance of the 1st and 2nd peak ⁶⁾. The experimental data shown in Fig.3 of improved power MOSFET demonstrate this requirement for the SEB hardened device. It is observed that the triggering V_{DS} for SEB is advanced from 280V to 310V.

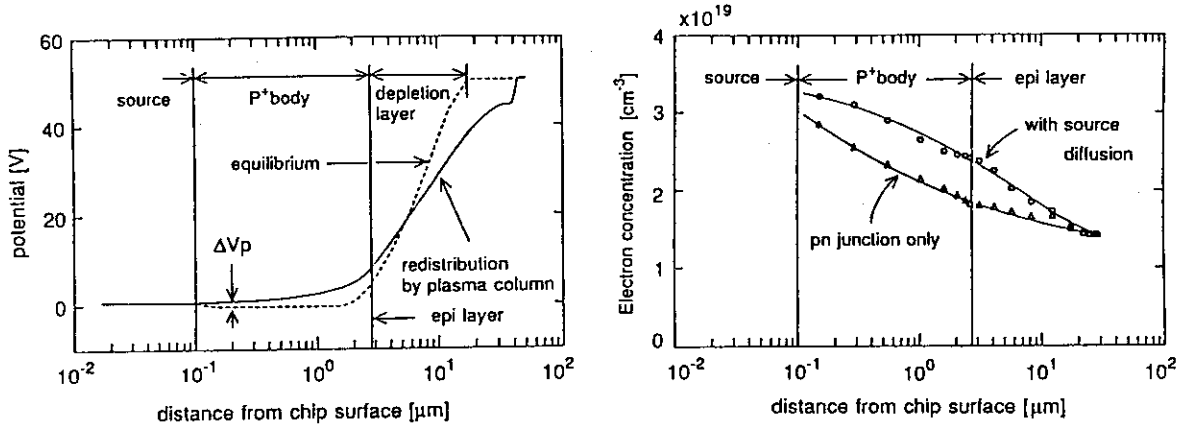


Fig.2. Simulation results for charge injection along an ion track

Potential redistribution by an incident ion (left). Injected electrons from the source electrode compared with the test structure (right). The simulation is performed using the impurity profile for a power MOSFET with $V_{DS}=50V$. Incident ion has $LET=20 \text{ MeV}/(\text{mg}/\text{cm}^2)$ with $36\mu\text{m}$ of range. Both figures are at 50ps after the incidence.

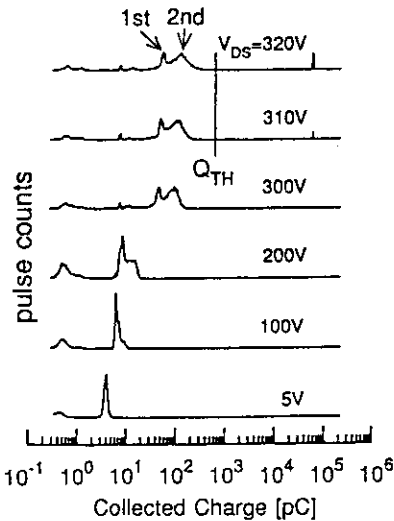


Fig.3. EPICS spectrum for improved power MOSFET with 200MeV Ni

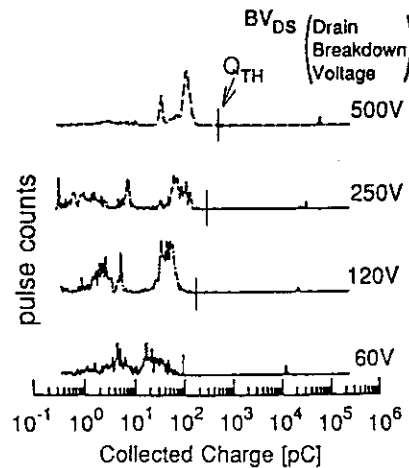


Fig.4. Q_{TH} for various BV_{DS} sample with 200MeV Ni

It is also indicated in Fig.1 that the both peaks move toward right with increasing V_{DS} , and SEB is triggered when a threshold charge Q_{TH} is reached. Fig.4 shows the charge spectra obtained by Ni ion irradiation for several samples which have different BV_{DS} . A large amount of collected charge is observed for a high BV_{DS} sample with thick epitaxial layer. Each sample has different Q_{TH} attribute to a specific device design such as the device structure and the impurity profile. Moreover, charge spectra shown in Fig.5 by C ions indicate that SEB are triggered, whereas the 1st and 2nd peaks (the 2nd peak is not distinguishable in this case) are still below Q_{TH} . There is very broad signal between the peaks and Q_{TH} . Additionally, according to SEL data for CMOS 64Kbit-SRAM shown in Fig.6, it is clearly observed that SEL occurrence rate for C ions differs from that for Si or

Ni ions. The broad signal of power MOSFET and SEL occurrence of SRAM for C ions may originate from nuclear reactions because of the higher energy transfer rate as compared with elastic recoils. To confirm practically nuclear reactions, an experiment to identify the coincidence of the energy transfer from irradiating ions has been prearranged next year.

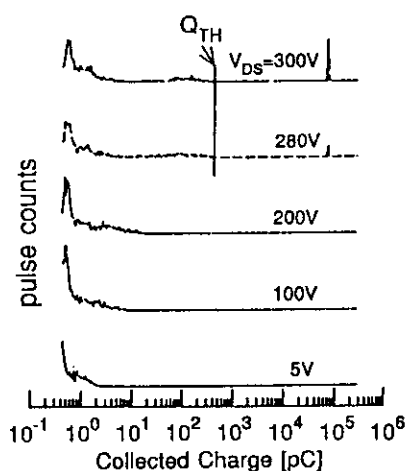


Fig.5. Broad signal bellow Q_{TH} with 105MeV C ions

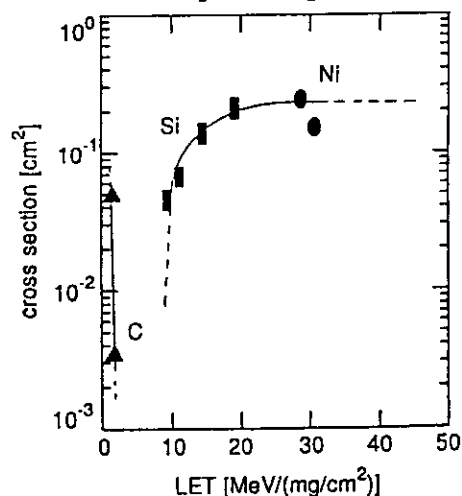


Fig.6. SEL cross section for CMOS 64Kbit-SRAM

CONCLUSION

A new SEB triggering mechanism by current flow along ion track was proved by preliminary numerical simulation in addition to experimental observation. This mechanism also suggests that a highly doped p^+ layer is preferable for SEB hardened devices. An experimental data of improved power MOSFET quite demonstrates this requirement.

It was observed that SEB triggering might be due to nuclear reactions. For further study to confirm nuclear reactions experimentally, preparation of new measurement system called multiple channel analyzer system is under way.

REFERENCES

- 1) Ikuo KANNO, et al., "Mechanism and Evaluation Technique for Single Event Phenomenon of power MOSFETs and SRAMs," JAERI-M 92-124, pp.79, (1992)
- 2) A.E.Waskiewicz, et al., "Burnout of Power MOS Transistors with Heavy Ions of Californium-252," IEEE Trans. Nucl. Sci., Vol.NS-33, No.6, pp.1710-1713, (1986)
- 3) J.H.Hohl, et al., "Analytical Model for Single Event Burnout of Power MOSFETs," IEEE Trans. Nucl. Sci., Vol.NS-34, No.6, pp.1275-1280, (1987)
- 4) J.H.Hohl, et al., "Features of the Triggering Mechanism for Single Event Burnout of Power MOSFETs," IEEE Trans. Nucl. Sci., Vol.NS-36, No.6, pp.2260-2266, (1989)
- 5) S.Nagata, et al., "Three dimensional device simulator VENUS-3D," Proc.10th Symposium on Calculation in Electrical and Electronic Engineering, pp.357-362, (1989)
- 6) S.Kuboyama, et al., "Mechanism for Single-Event Burnout of Power MOSFETs and Its Characterization Technique," IEEE Trans. Nucl. Sci., Vol.NS-39, No.6, pp.1698-1703, (1992)

III. NUCLEAR CHEMISTRY

3.1 Tests of a Gas-jet Coupled Ion Source for On-line Isotope Separator

Shin-ichi ICHIKAWA, Masato ASAI*, Hideki IIMURA, Nobuo SHINOHARA,
Kazuaki TSUKADA, and Akihiko OSA*

Department of Chemistry, JAERI

*Department of Nuclear Engineering, Nagoya University

A gas-jet coupled ion-source has been installed at the JAERI-ISOL. The purpose of this ion source is to study short-lived isotopes produced by charged-particle induced fission of actinide. The coupling of a gas-jet technique and ISOL system was proposed by Nitschki¹⁾ and used extensively in study of nuclei far from stability in several laboratories.^{2,3,4)} The gas-jet coupled ISOL system has two merits:

- 1) the delay time is short, corresponding to the mean transport time in the gas-jet system, and
- 2) the target is located far from the hot environment of the ion source, which allows low melting-point elements such as transuranium elements to be used as a target.

In this paper, the performance of the gas-jet-coupled ion source and overall efficiencies for some neutron-rich rare-earth nuclides are given.

A schematic illustration of the gas-jet coupled ion source system is shown in Fig. 1. The system consists of an aerosol generator, a target chamber, a skimmer chamber, a differential pumping system, and an ion-source. The target chamber is connected to the tandem accelerator beam line with a HAVAR foil window of 5 μm thickness. In this study, argon gas was used as a carrier gas. Since the range of fission products is much shorter in Ar gas than in He gas, a smaller target chamber can be used in the case of Ar gas, which allows much shorter evacuation time of the gas through the chamber. The skimmer chamber was evacuated by differential pumping system which is composed of two turbomolecular-pumps having pumping speeds of 1800 l/s and 300 l/s, respectively. In order to obtain high ionization efficiencies for short-lived rare-earth elements, a high-temperature thermal ion source was used. The ion source consists of a vaporizer, an ionizer, a tungsten filament, and a heat shield.

The temperature around the ionizer was measured to be 2500 K by an optical pyrometer. The argon mass flow rate through an exit hole of capillary tube and the pressure inside the skimmer chamber were measured to be 40 cm^3/s (STP) and

≤ 10 Pa, respectively, at maximum. The geometrical conditions and typical gas-jet parameters are summarized in Table 1.

The performance of the ion-source system was tested by measuring intensities of mass-separated ions in on-line experiments. The short-lived isotopes were produced by proton induced fission of ^{238}U . The γ -ray associated with the decay of individual isotopes was measured with a HPGe detector placed in front of collection point of a tape transport system. In this measurement, the acceleration voltage of the ISOL was set at 30 kV. The total separation efficiency, defined as the ratio of number of isotopes collected at the tape system to that produced by the ^{238}U fission, is estimated to be 7.3% for ^{140}Cs , 4.3% for ^{144}La , 5.8% for ^{148}Pr and 3.9% for ^{152}Nd by taking into account the beam intensity, the target thickness and the formation cross sections.^{5, 6)}

Mass-separated beam intensities obtained with this ion source system are summarized in Table 2. The values are normalized to a proton beam current of 1 μA . We notice from the results that the mass-separated beam intensities of isotopes with $A \geq 150$ are significantly enhanced in proton induced fission of ^{238}U over those obtained from thermal-neutron fission of ^{235}U .

References

- 1) J.M.Nitschke, in: Proc. Int. Conf. on properties of nuclei far from the region of beta-stability, Leysin, Switzerland, 1970, Vol.1(CERN, Geneva, 1970)p.153.
- 2) R.A.Anderl, V.J.Novick and R.C.Greenwood, Nucl. Instr. Meth. **186**(1981)153.
- 3) K.Okano, Y.Kawase, K.Kawade, Y.Yamamoto, M.Hanada, T.katoh and I.Fujiwara, Nucl. Instr. Meth **186**(1981)115.
- 4) D.M.Moltz, R.A.Gough, M.S.Zisman, D.J.Vieira, H.C.Evanse and J.Cerny, Nucl. Instr. Meth. **172**(1980)507.
- 5) H.Umezawa, J.Inorg. Nucl. Chem. **33**(1971)2731.
- 6) A.T.Kandil, J.Inorg. Nucl. Chem. **38**(1976)37.

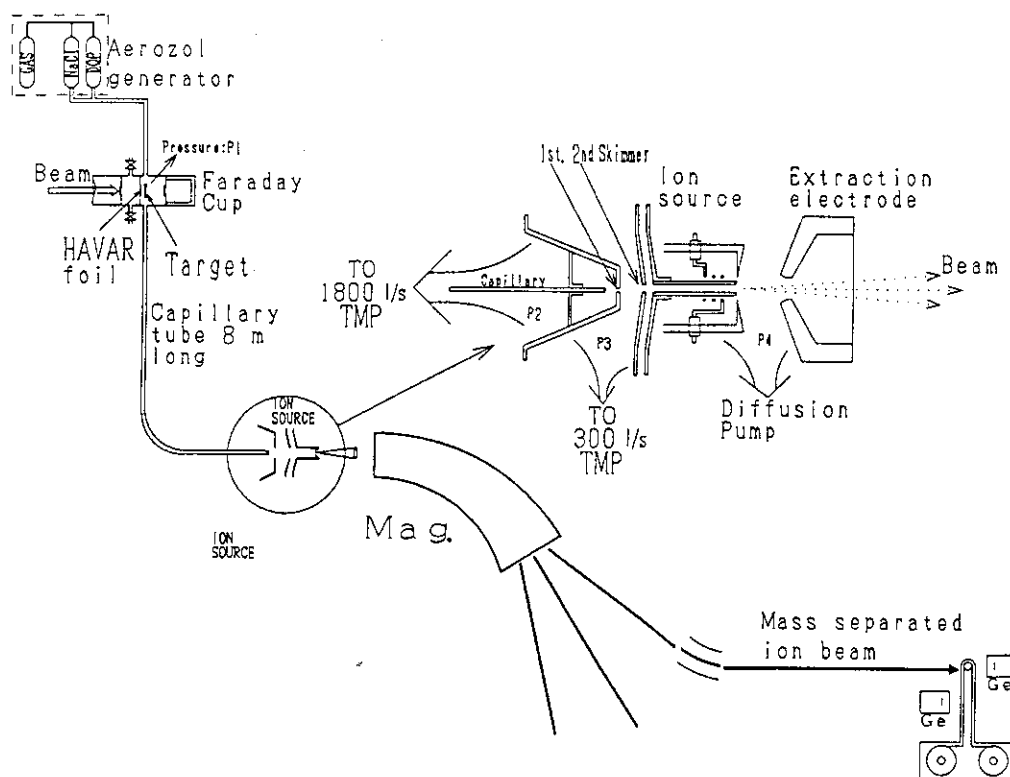


Fig.1 Out-line of gas-jet-coupled ion source system prepared for the study of short-lived neutron-rich nuclei produced in charged particle induced fission.

Table 1 Some typical values of the gas-jet-coupled ion source parameters for operation with proton induced fission of ^{238}U

Aerosol material	DOP+NaCl	
Carrier gas	Ar	
Gas flow rate	40 cm ³ /s STP	
Volume of target chamber	75	cm ³
Target chamber pressure(P1)	8x10 ⁴	Pa
1st-skimmer chamber pressure(P2)	≤10	Pa
2nd-skimmer chamber pressure(P4)	≤10 ⁻³	Pa
capillary/1st skimmer separation	7	mm
1st/2nd-skimmer separation	11	mm
Acceleration voltage	30	kV
Ion source temperature	2450	K

Table 2 Radioactivities mass-separated by the
gas-jet coupled JAERI-ISOL following nuclear
reaction, $^{238}\text{U} + \text{P}$, at $E(\text{P})=15 \text{ MeV}$

Nuclide	half-life	beam strength (atoms/s μA)
^{140}Cs	63.72 s	7200
^{144}Cs	1.02 s	~90
^{144}Ba	11.5 s	2500
^{144}La	40.8 s	2900
^{148}La	1.05 s	15
^{148}Pr	2.0, 2.27 m	1240
^{152}Nd	11.6 m	600
^{156}Pm	26.7 s	120
^{160}Eu	44. s	20

3.2 Measurement of Hyperfine Structure in Radioactive Nuclide, ^{143}Pr ($T_{1/2} = 13.6$ D), by Collinear Laser-ion-beam Spectroscopy

Hideki IIMURA, Masashi KUBOTA, * Yoshinori NAKAHARA,
Shin-ichi ICHIKAWA and Takayoshi HORIGUCHI**

Department of Chemistry, JAERI, *Department of Physics, Toho
University, **Department of Physics, Hiroshima University

Collinear laser-ion-beam spectroscopy can provide sub-Doppler resolution and has been used to study hyperfine structure (hfs) in ions of some stable and long-lived isotopes. Recent developments of on-line mass separation technique have made this spectroscopy applicable to short-lived isotopes. There are a few groups in the world working on this subject and they determined the hyperfine constants in long isotopic chains of several elements. However, the hyperfine constants of many isotopes remain unknown. Because nuclear moments can be determined from the hyperfine constants and are important information for nuclear structure research, more experiments on hfs are needed. At JAERI-ISOL we have studied nuclear structure of rare-earth elements by β - γ spectroscopy. In order to strengthen this research we set up a beam line of collinear laser-ion-beam spectroscopy a few years ago.

The $Z=59$ Pr isotopes exhibit a transition from spherical to deformed shapes as the neutron number increases from $N=82$ to 90, providing a good chance of testing various nuclear models. In these isotopes, level scheme of ^{143}Pr ($T_{1/2} = 13.6$ d) was studied through the ^{143}Ce ($T_{1/2} = 1.4$ d) β -decay.¹⁾ However, the nuclear moments of the ground state of ^{143}Pr are unknown and it is an obstacle to make detailed theoretical investigations of this nucleus. In this work we performed measurements of hfs in ^{143}Pr by collinear laser-ion-beam spectroscopy to determine the nuclear moments of this nucleus.

The ^{143}Ce nucleus, the parent of ^{143}Pr , was produced by the thermal neutron irradiation of CeO_2 powder (enriched to 92.77 % in ^{142}Ce) in JRR3. After the irradiation the activity was cooled for about a week until most of ^{143}Ce decayed to ^{143}Pr , and then ^{143}Pr was separated from $^{142}, ^{143}\text{Ce}$ by a solvent extraction method. The separated ^{143}Pr was put into a surface ionization ion source of JAERI-ISOL.

The experiment was performed in the same way as that of ^{141}Pr .²⁾ The $^{143}\text{Pr}^+$ ions, part of which are in the metastable $4f^3(4I^0)5d^5G_2$ level, was produced by the ion source and then accelerated to 40 keV. After mass-separation with a magnet, the $^{143}\text{Pr}^+$ ions were injected into the beam line of laser spectroscopy. The intensity of the beam was about 1×10^7 ions/sec. The metastable ions were excited to the $4f^3(4I^0)6p^5H_3$ level by a counter propagating laser beam. The interaction region was defined by a cage of 10 cm in length and 1 cm in diameter, which was kept at the potential of -3 kV. Resonance was observed by detecting the fluorescence light from the 5H_3 level to the ground level. The fluorescence light was collected by an ellipsoidal mirror onto a cooled photomultiplier. This mirror was installed for this experiment instead of a spherical mirror used before, and the efficiency was improved by about seven times. Stray light from the laser beam was suppressed by broad-band filters. Hyperfine spectra were measured by scanning the laser frequency of about 10 GHz and recorded in multichannel scaling (MCS) mode by using a personal-computer-based data

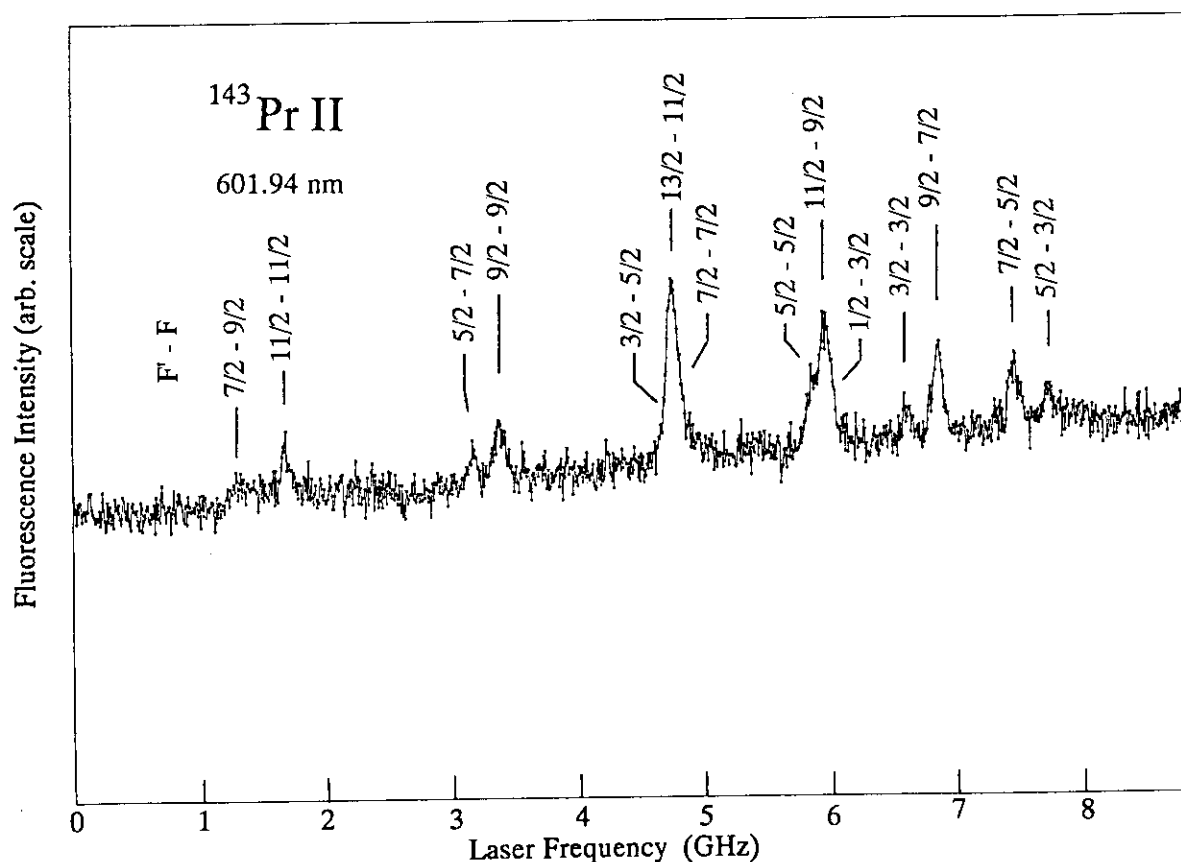


Fig. 1. Typical hyperfine spectrum of the transition 5G_2 - 5H_3 ($\lambda = 601.94$ nm) in ^{143}Pr ($T_{1/2} = 13.6$ d). F quantum numbers are indicated for upper state (F') and lower state (F).

acquisition system. A transmission of a confocal etalon with a free spectral range of 150 MHz was also recorded simultaneously as calibrations of the frequency.

Typical hyperfine spectrum obtained for ^{143}Pr II from the metastable $^5\text{G}_2$ level to the $^5\text{H}_3$ level ($\lambda = 601.94$ nm) is shown in Fig.1. This is the first hyperfine-spectrum obtained in this country for a radioisotope by collinear laser-ion-beam spectroscopy. The hyperfine components are assigned as shown in Fig. 1. The analysis of the data is in final stage now, and the hyperfine constants A and B will be obtained soon.

References

- 1) D. F. Kusnezov, D. R. Nethaway and R. A. Meyer: Phys. Rev. C40 (1989) 924.
- 2) H. Iimura, Y. Nakahara, S. Ichikawa, K. Kotani, M. Wakasugi and T. Horiguchi: J. Phys. Soc. Jpn. 59 (1990) 4208.

3.3 Level Scheme of ^{127}La Fed by the ^{127}Ce Decay

Hideki IIMURA, Shin-ichi ICHIKAWA, Nobuo SHINOHARA,
Masaaki Magara, Masumi OSHIMA, * Masato ASAI**
Akihiko OSA** and Hiroshi YAMAMOTO**

Department of Chemistry, JAERI, *Department of Physics,
JAERI, **Department of Nuclear Engineering,
Nagoya University

Neutron-deficient nuclei in the $A=120-130$ mass region exhibit a transition from triaxial to prolate shapes, providing a good chance of testing various nuclear models. For the ^{127}La nucleus, in-beam γ -ray spectroscopic studies^{1,2)} were made to establish high-spin level structure. They proposed two rotational bands although the band-head energy remains unknown. There has been no other information on the level scheme of ^{127}La except a few γ -rays assigned to the decay from ^{127}Ce to ^{127}La .^{3,4)} Therefore the level scheme of ^{127}La remains quite incomplete. In the present work, we studied the level scheme of ^{127}La through the β -decay of ^{127}Ce ($T_{1/2}=32$ sec) to clarify mainly the structure of low-spin levels.

The experiments were performed by using the on-line mass separator at the tandem accelerator facility. The ^{127}Ce nucleus was produced by the reaction $^{nat}\text{Mo}(^{35}\text{Cl}, 1\text{pxn})^{127}\text{Ce}$ with a 185-MeV ^{35}Cl beam. Reaction products were ionized in a surface ionization ion source and then mass-separated electromagnetically. In order to obtain ^{127}Ce activity free from the Cs and Ba isobars, the monoxide ions $^{127}\text{Ce}^{16}\text{O}^+$ were separated by setting the magnetic field at the mass number of 143. This method was not able to separate ^{127}La from ^{127}Ce , and the former was the main impurity throughout this experiment. The mass-separated ^{127}Ce activity was implanted into an aluminum-coated Mylar tape in a tape transport system and periodically transported to a measuring position, where γ -ray singles measurements were performed with a low-energy photon HPGe detector and a 20 % HPGe detector. The decays of γ -rays were traced by taking successively 16 spectra counted for 4 sec each in order to distinguish γ -ray peaks of ^{127}Ce from those of daughter nuclides.

For this work, we have developed a chamber of the tape transport system, which allowed us to place two Ge detectors very close to the point

at which mass-separated ion beam hit the tape. A 32 % HPGe detector and a 28 % n-type HPGe detector were set on this chamber for γ - γ coincidence measurements. This setup improved the coincidence efficiency more than two times. Coincident events were recorded in list mode on a 5-inch compact disk, the capacity of which is 600 M byte.

In order to obtain more information on transitions, a β - γ delayed coincidence measurement was performed with a plastic scintillator and the low-energy photon HPGe detector. A simultaneous measurement of γ -rays and electrons was also made with the n-type HPGe detector and a Si(Li) detector to determine internal conversion coefficients.

Data analysis is now in progress. Although very preliminary, several new γ -lines have been assigned to the decay of ^{127}Ce , which are summarized in Table I.

Table I. Energies (in keV) of the γ -rays of ^{127}Ce .

Present work	Previous work ^{a)}
58.5, 75.7, 120.3, 137.5, 177.5, 196.0, 226.3, 236.1, 279.6, 311.6, 423.0, 428.7, 456.3	58.6, * 114.8, 120, * 177, 253, 398

a) Data from refs. 3 and 4.

* gamma-rays probably belonging to ^{127}Ce .

References

- 1) D. Ward, H. Bertschat, P. A. Butler, P. Colombani, R. M. Diamond and F. S. Stephens: Phys. Lett. **56B** (1975) 139.
- 2) P. J. Smith, D. J. Unwin, A. Kirwan, D. J. G. Love, A. H. Nelson, P. J. Nolan, D. M. Todd and P. J. Twin: J. Phys. **G11** (1985) 1271.
- 3) D. D. Bogdanov, A. V. Demyanov, V. A. Karnaukhov, M. Nowicki, L. A. Petrov, J. Voboril and A. Plochocki: Nucl. Phys. **A307** (1978) 421.
- 4) J. Genevey, A. Gizon, N. Idrissi, B. Weiss, R. Beraud, A. Charvet, R. Duffait, A. Emsallem, M. Meyer, T. Ollivier and N. Redon: Proc. 5th Int. Conf. on Nucl. Far From Stability, Ontario, Canada, 1987, p. 419.

3.4 Decay Properties of ^{245}Cf

Masaaki MAGARA, Nobuo SHINOHARA, Kazuaki TSUKADA,
Yuichi HATSUKAWA*, Shin-ichi ICHIKAWA, Yuichiro NAGAME* and
Masumi OSHIMA**

Department of Chemistry, *Department of Radioisotopes, **Department of
Physics, JAERI.

I. Introduction

Californium-245 was produced in 1950 as the first isotope of 98th element by $^{242}\text{Cm}(\alpha, n)^{245}\text{Cf}$ reaction¹⁾. The ^{245}Cf nuclide decays by an orbital electron capture (EC-decay) and an alpha particle emission (α -decay) with branching of about 70% for the EC decay and 30% for the α -decay²⁾. The α -particle energies measured by Kusch et al.³⁾ are 7.137, 7.084, 7.036, 6.983 and 6.886 MeV, but the intensities of α -groups have not been determined yet. There are no data on the γ -rays following the decay of ^{245}Cf .

We have investigated the decay of neutron-deficient californium nuclides and clarified the decay properties of ^{245}Cf such as the half-life, the relative intensities of the α -groups and the branching ratio of α -decay to the EC-decay. In this paper, the results are described on the γ -rays following the decay of ^{245}Cf with α - γ and X- γ coincidence measurements, and the preliminary decay scheme of ^{245}Cf is proposed on the basis of those data.

II. Experimental

Natural uranium targets (3 to 7 mg/cm² thick) were prepared by the sedimentation method using an acetone solution. The uranium targets were irradiated with ^{12}C ions (76 MeV) for 1.5 hours at the tandem accelerator and average beam intensity was 160 particle nA. After the irradiation, the produced californium nuclides were separated rapidly by the anion-exchange method⁴⁾ using the computer-controlled rapid ion-exchange separation system⁵⁾. The radiometric sources were prepared by evaporating the effluent of californium fraction on titanium disks. The two-parameter α - γ and X- γ coincidence measurements were carried out using a silicon surface barrier detector and two germanium detectors.

III. Results and discussion

Figure 1 shows the projected spectrum of γ -rays coincident with α -ray of 7.090 MeV obtained from the α - γ coincidence measurement. Two γ -rays of 56.1 keV and 50.5 keV together

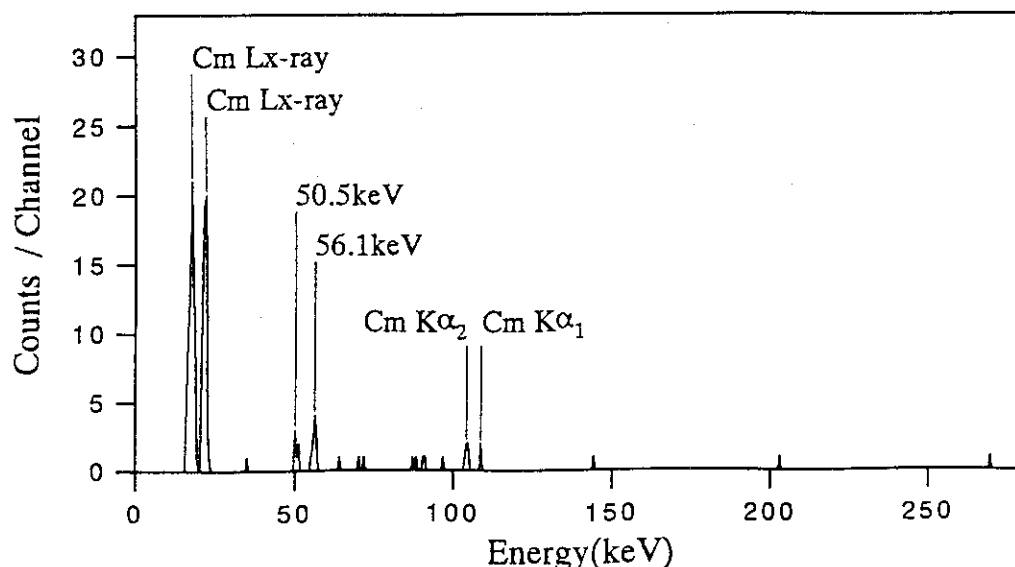


Fig. 1 Projected spectrum of γ -rays obtained from α - γ coincidence measurement.

with X-rays of Curium are observed in the spectrum. However, no γ -ray was observed in the projected spectrum of γ -rays coincident with the α -ray of 7.145 MeV. This result suggests that the 7.145 MeV α -group feeds to the ground state of ^{241}Cm , $1/2^+ [631]$. If the observed α transition with the largest intensity is a favored transition which has no spin and parity change, it is reasonable that the ground state of ^{245}Cf is $1/2^+$.

Assuming that the ground state of ^{245}Cf is $1/2^+$, rotational levels of ^{241}Cm nuclei are deduced from the observed α -ray energies using the relation between the rotational energy and band-head angular momentum⁶⁾.

Five α -groups, 7.145, 7.090, 7.065, 7.023 and 6.985 MeV, were observed in α -decay of ^{245}Cf . As the 7.145 MeV α -ray is a favored

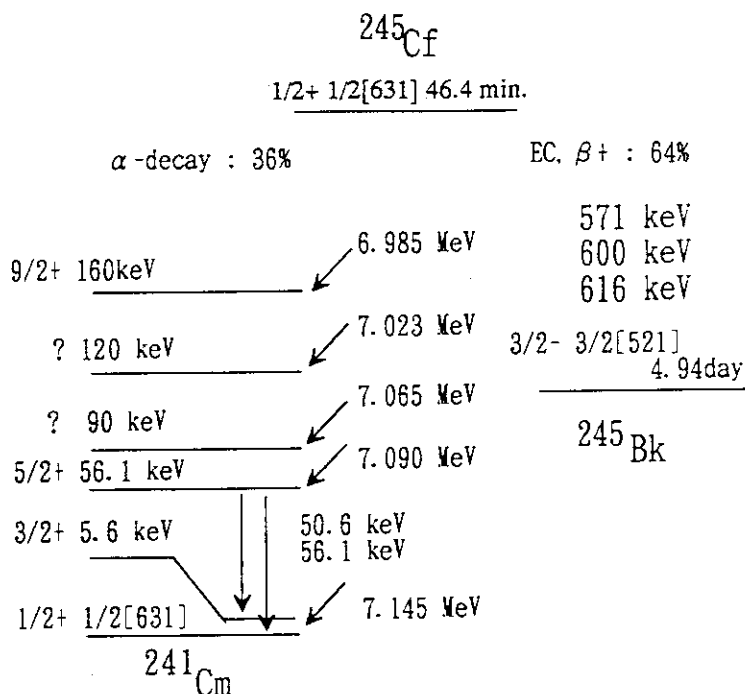


Fig. 2 : Proposed decay scheme of ^{245}Cf

transition, the lower α -group of 7.090 MeV can be the transition to the member of the rotational band and would be the transition to the $5/2$ level. It is considered that two γ -rays of 56.1 and 50.6 keV observed in coincidence with α -ray of 7.090 MeV are assigned to the $5/2 \rightarrow 1/2$ and $5/2 \rightarrow 3/2$ transitions, respectively. The energy levels $7/2$ and $9/2$ are expected at 69 and 160 keV, respectively. The energy level fed by 6.985 MeV α -group should be assigned to $9/2$. However, the level excited at 69 keV is close to both levels at 56.1 keV and 90 keV, so it is very difficult to observe the $7/2$ level separately from those of 56.1 keV and 90 keV in α -ray measurement.

From those results, we propose the decay scheme of ^{245}Cf as shown in fig. 2.

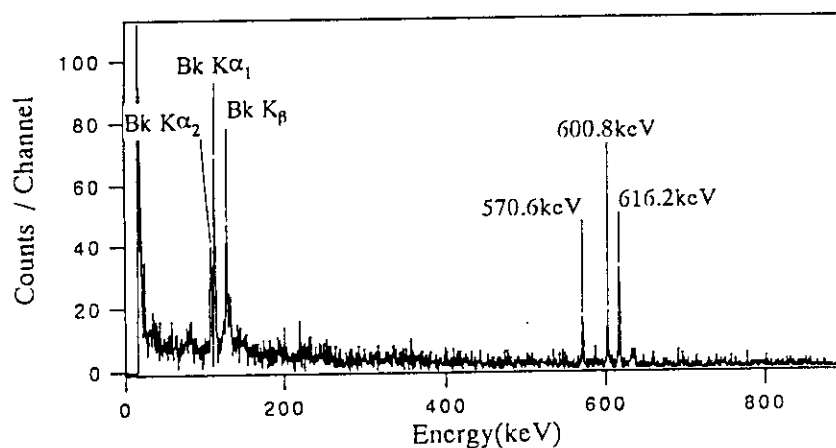


Fig. 3 Projected spectrum of γ -rays obtained from X- γ coincidence measurement.

Figure 3 shows the projected spectrum of γ -ray coincident with the berkelium K X-ray. It is found from the figure that the γ -rays of 571, 600 and 616 keV have the same origin as the characteristic X-ray of berkelium. Also half-lives of these γ -rays are in agreement with that of ^{245}Cf (46.4 min). However, no γ -ray coincident with the γ -rays of 571, 600 and 616 keV was observed in the projected γ -ray spectrum.

References

- 1) S.G. Thompson, K. Street, Jr., A. Ghiorso and G.T. Seaborg: Phys. Rev. **80** (1950) 790.
- 2) A. Chetham-Strode, Jr., G.R. Chopin and B.G. Harvey: Phys. Rev. **102** (1956) 747.
- 3) W. Kusch and Z. Szegłowski: JINR-E6-3992 (1968).
- 4) S. Usuda: J. Radioanal. Nucl. Chem.: **111** (1987) 477.
- 5) K. Tsukada, T. Ohtsuki, K. Sueki, Y. Hatsukawa, H. Yoshikawa, K. Endo, H. Nakahara, N. Shinohara, S. Ichikawa, S. Usuda and M. Hoshi: Radiochimica Acta **51** (1990) 77.
- 6) A. Bohr and B.R. Mottelson: Mat Fys Medd. Dan Vid. Selekt. **27** (1953) 16.

3.5 A Research for the Production of Transuranium Elements

Ichiro FUJIWARA, Seiichi SHIBATA*, Hisaaki KUDO**, Nobuo SHINOHARA***, Kazuaki TSUKADA***, Shin-ichi ICHIKAWA***, Hideki IIMURA***, Masaaki MAGARA***, Masumi OSHIMA****

School of Economics, Otomon Gakuin University, *Institute for Nuclear Study, University of Tokyo, **Department of Chemistry, Niigata University, ***Department of Chemistry, ****Department of Physics, JAERI

Transuranium isotopes produced by the heavy ion reactions have been studied by means of helium-jet recoil-transport technique.¹⁾ For production of nobelium, target of ^{244}Pu was bombarded by ^{16}O beams, where the nobelium isotopes are expected to be produced through the $^{244}\text{Pu}(^{16}\text{O}, xn)^{260-x}\text{No}$ reactions. Alpha-ray spectrum of the reaction products is shown in Fig. 1. The isotopes of ^{256}No (half-life; 2.91 s) and ^{255}No (3.1 min) are observed in this spectrum.

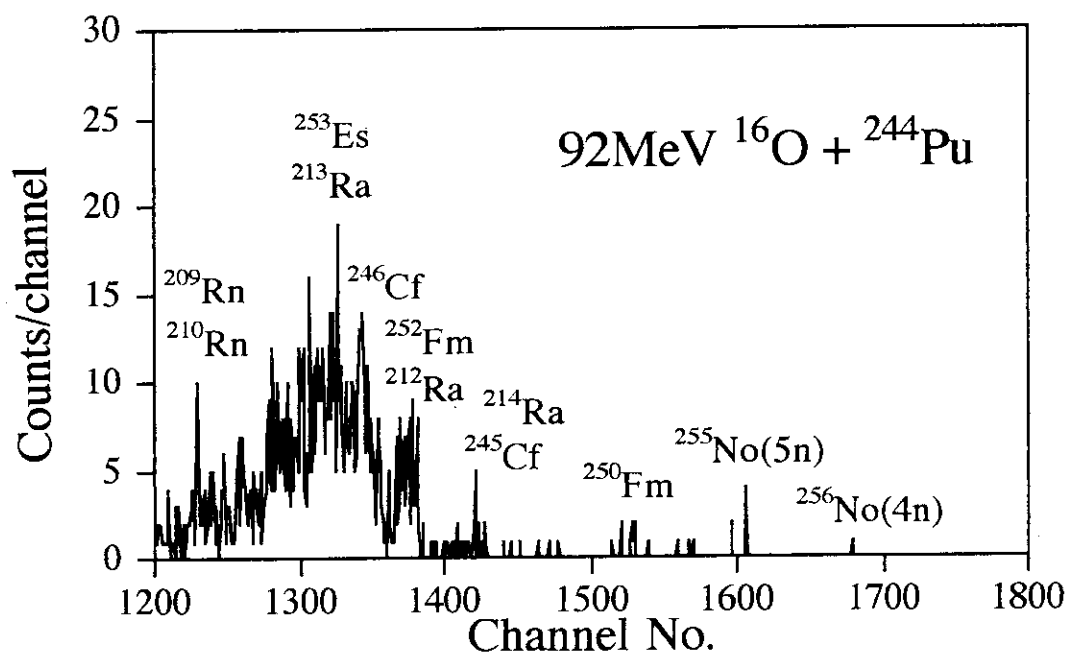


Fig. 1 Alpha-ray spectrum measured in the $^{16}\text{O} + ^{244}\text{Pu}$ reaction.

Reference

- 1) I. Fujiwara, et al.: JAERI-M 92-124 (1992) 106.

3.6 Fast Separation of Iodine Produced from Heavy Ion-induced Fissions of Actinides

Nobuo SHINOHARA, Kazuaki TSUKADA, Shin-ichi ICHIKAWA,
Masaaki MAGARA, Tsutomu OHTSUKI*

Department of Chemistry, JAERI, *Laboratory of Nuclear
Science, Tohoku University

The isotopic yields of iodine have been measured in the ^{12}C - and ^{19}F -induced fissions of ^{235}U , ^{238}U and ^{237}Np using a fast radiochemical separation technique followed by γ -ray spectrometry.¹⁾ Figure 1 shows the schematic drawing for the rapid separation of iodine. In the γ -ray measurement on the chemically-separated iodine fraction, the isotopes of $^{128-141}\text{I}$ were observed and their yields were determined. Detailed discussion on the fission yields will be presented elsewhere.

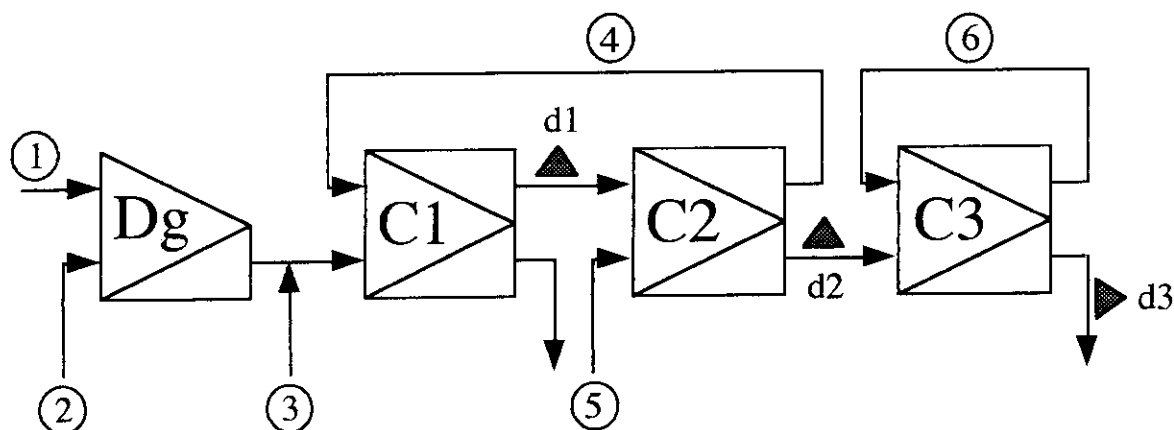


Fig. 1 Flow sheet of the SISAK chemical separation system for the fast separation of iodine. Dg, C and d in the figure stand for degasser, centrifuge and Ge detector, respectively. The reagents used in the separation are as follows: (1) gas-jet (KCl , He), (2) 0.1M H_2SO_4 , 0.001M KI , 0.01M NaHSO_3 , (3) 0.25M NaNO_2 , (4) CCl_4 , (5) 0.1M H_2SO_4 , 0.2M NaHSO_3 , and (6) CHCl_3 . The aqueous solutions are heated to about 90°C .

Reference

- 1) N. Shinohara, et al.: JAERI-M 92-124 (1992) pp.108.

3.7 Fission of the $^{238}\text{U} + \text{p}$ System in the Giant Dipole Resonance Region

Ryoichi KASUGA, Takayuki YAMAGUCHI, Daisaku YANO, Naruto TAKAHASHI, Akihiko YOKOYAMA, Hiroshi BABA and Nobuo SHI-NOHARA*

Department of Chemistry, Faculty of Science, Osaka University, *Department of Chemistry, JAERI

Fission mass and nuclear charge distributions of actinide nuclei in low excitation energy (spontaneous and thermal neutron induced fission) are known to be different from those in the region above 20 MeV¹⁾. We assumed that the giant dipole resonance, GDR, might take a part for the difference in the fission characteristics, and the mass and charge distributions of the fission fragments have been measured for the $^{238}\text{U} + \text{p}$ system in the range of $E_x = 11.7 - 20.6$ MeV by means of radiochemical method²⁾ in order to settle the question.

The width of the heavy wing obtained by fitting to the observed mass distribution with Gaussian curve remained nearly constant over the energy range studied, whereas that of the light wing which was equal to that of the heavy wing at $E_x = 12.4$ MeV monotonously increased with the excitation energy until it reached to the maximum around $E_x = 17$ MeV. Then the FWHM turned to decrease with increase of the excitation energy and approached again to that of the heavy wing at $E_x = 20.6$ MeV as shown in Fig. 1. It is known that the giant dipole resonance takes place around $E_x = 14$ MeV³⁾. The width of the light wing reaches the maximum at $E_x = 17$ MeV and the energy is different to the maximum energy of GDR but so far we have not obtained any indication that the change of fission characteristics took place due to the GDR excitation. In the present study we attempted to study more closely the symmetric fission region where the data were quite scarce and also to obtain more precise data of charge and mass distributions at $E_x = 16.0 - 18.6$ MeV.

Uranium targets were prepared by electrodeposition of UO_2 onto aluminum foils of 1.5 mg/cm^2 in thickness. The thickness of uranium was $1.5 - 2 \text{ mg/cm}^2$. Each target was sandwiched by five aluminum foils of 1.5 mg/cm^2 in thickness in order to separate the fission fragments by the difference of the ranges. Silver, cadmium and indium were chemically separated from the target and other fission products in order to obtain precise data in the symmetric mass region. Irradiation was carried out with a proton beam from the tandem Van de Graaff at Japan Atomic Energy Research Institute. The excitation energies applied in the experiments were 16.0, 16.5, 17.2 and 18.6 MeV.

Long and short irradiations of uranium targets were carried out; the former for 3 hours and the latter for 30 minutes in general. After the irradiation the targets were subjected to the non-destructive γ -ray spectrometry combined with chemical separation when necessary. Gamma-rays were measured by means of Ge detectors for the non-destructive and chemically separated samples. Measured γ -ray spectra were analyzed by use of BOB code⁴⁾. The detected photopeaks were assigned to relevant nuclides and their formation cross sections were determined.

The light fragments were selectively collected by the difference of the ranges and the precise cross sections were obtained in symmetric mass region. The mass distributions at $E_x = 17.2$ MeV obtained in this study is shown in Fig. 2. Though the width of the heavy wing is equal to that obtained previously, the value of the light wing is 18 amu instead of the previous value of 20 amu. The difference arose mainly due to introduction of a different charge distribution. The analysis is still progressing.

References

- 1) S.Baba, H. Umesawa and H. Baba, Nucl. Phys., A175(1971)177.
- 2) N. Nitani, T. Yamaguchi, D. Yano, N. Takahashi, H. Baba and N. Shinohara, JAERI-M 92-124(1992)119.
- 3) J.T. Cadwell, E. J. Dowdy, B. L. Berman, R. A. Alvarez and T. Meyer, Phys. Rev. C21(1980)1215.
- 4) H. Baba, T. Sekine, S. Baba and H. Okashita, JAERI Report, (1972)1227.

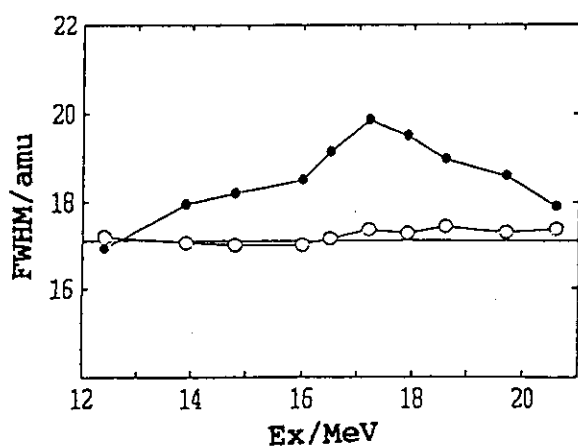


Fig. 1. The variation of the FWHM with excitation energy ●: light wing, ○: heavy wing.

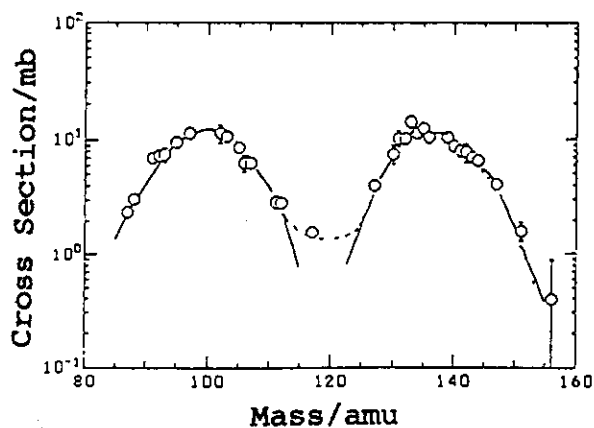


Fig. 2. Mass distribution of the $^{238}\text{U} + p$ system at $E_x = 17.2$ MeV

3.8 Angular Distribution of Fission Fragments in Proton-induced Fission of ^{232}Th and ^{244}Pu

Kazuaki TSUKADA, Nobuo SHINOHARA, Yuichiro NAGAME *,
Shin-ichi ICHIKAWA, Masaaki MAGARA, Yuichi HATSUKAWA *,
Ichiro NISHINAKA ** and Hiromichi NAKAHARA **

Department of Chemistry, *Department of Radioisotopes, JAERI

**Faculty of Science, Tokyo Metropolitan University

The incident energy dependence on the formation cross section of the fission fragments produced in the higher asymmetric fission has been studied by a radiochemical method. These results show that the energy dependence of the higher asymmetric products is obviously different from that of the symmetric products, and is rather similar to that of the asymmetric products near the peak top of the mass distribution. In order to investigate the correlation between the angular anisotropy and the fragment mass in the higher asymmetric region, the angular distribution of fission fragments has been measured.

Angular distribution of fission fragments in 15 MeV proton-induced fission of ^{232}Th 1) and ^{244}Pu were measured by the recoil-catcher foil method. An aluminum catcher foil of 4.9 mg/cm^2 thickness was put on the wall of a semicylindrical holder of 60 mm in length and a 35 mm radius. The proton-bombardment was performed for about 10 h at the JAERI tandem accelerator. After bombardment the aluminum catcher foil was taken out and sliced to strips of appropriate width corresponding to some solid angle. In addition, the asymmetric rare earth products were chemically separated from the other fission products by the computer-controlled rapid ion-exchange separation system 2), and determined with the γ -ray spectrometry. The measured radioactivities were corrected for decay, genetic relationships, chemical yield, and cutting ambiguity so that the relative radioactivities at the end of bombardment could be obtained. The values of $W(\theta)$ at 13 different angles from each irradiation were least square fitted to the equation; $W(\theta) = a + b \cos^2 \theta$. The typical angular distribution of ^{143}Ce produced in the system of $^{232}\text{Th} + p$ is shown in Fig. 1 along with the fitted curve. The anisotropy of each product was defined as $1 + b/a$, that is, $W(0^\circ)/W(90^\circ)$. The dependence of the angular anisotropy on fragment mass in the system of $^{232}\text{Th} + p$ is shown in Fig. 2. The asymmetry degree of mass division is defined as the ratio of the mass of a heavy fragment to that of the complementary light fragment, the correlation between the angular anisotropy and the fragment mass ratio is shown in Figs. 3 and 4. From these figures, the anisotropies of symmetrically divided fission products are considerably smaller than those of asymmetrically divided one, while the anisotropies are of intermediate value for the intermediate mass division. The anisotropy of the higher asymmetric region is similar to

that of the asymmetric region near the peak top of the mass distribution as shown in Figs. 3 and 4.

References

- 1) H.Kudo et. al, Phys. Rev. **C25** (1982) 909.
- 2) K.Tsukada et. al, Radiochim. Acta **51** (1990) 77.
- 3) H.Kudo et al, Phys. Rev. **C25** (1982) 3011.

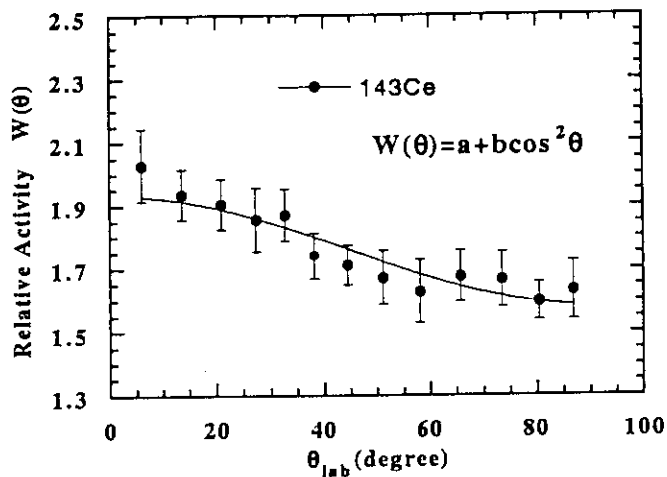


Fig. 1 Angular distribution of ^{143}Ce produced in the 15 MeV proton-induced fission of ^{232}Th . The line is the curve fitted by the least-squares method assuming $W(\theta) = a + b \cos^2 \theta$.

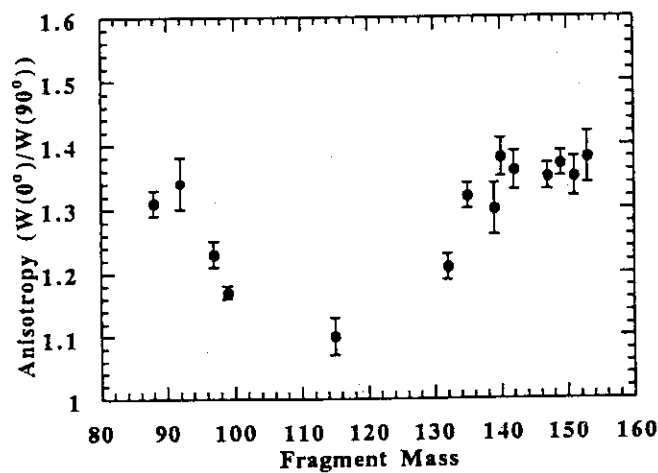


Fig. 2 Angular anisotropy of fission fragments produced in the system of $^{232}\text{Th} + p$ as a function of fragment mass.

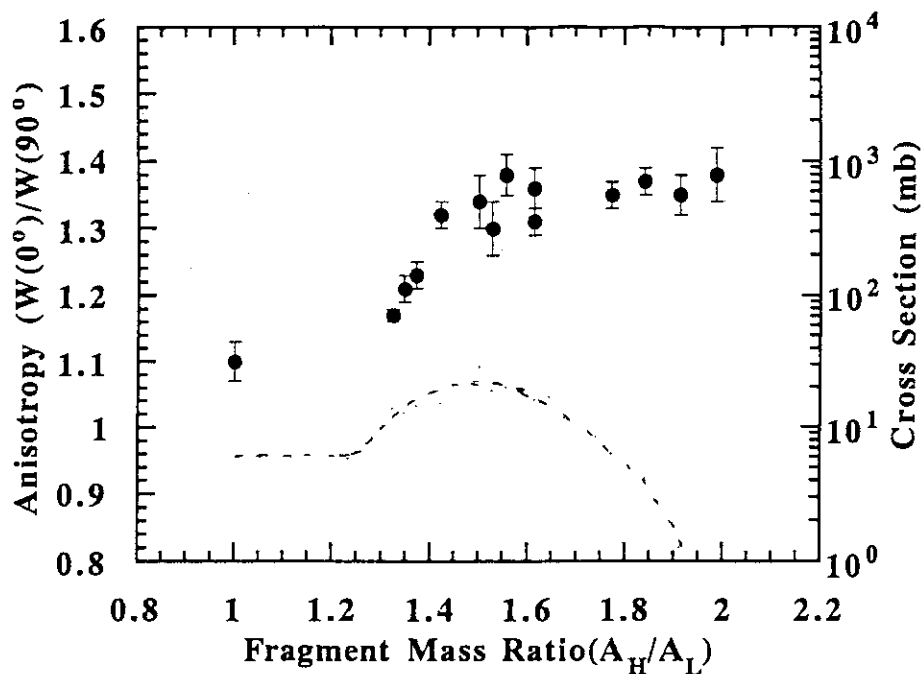


Fig. 3 Dependence of angular anisotropy on fragment-mass ratio in the 15 MeV proton-induced fission of ^{232}Th . The dashed curve is the mass yield curve for the 14.8 MeV proton-induced fission of ^{232}Th 3).

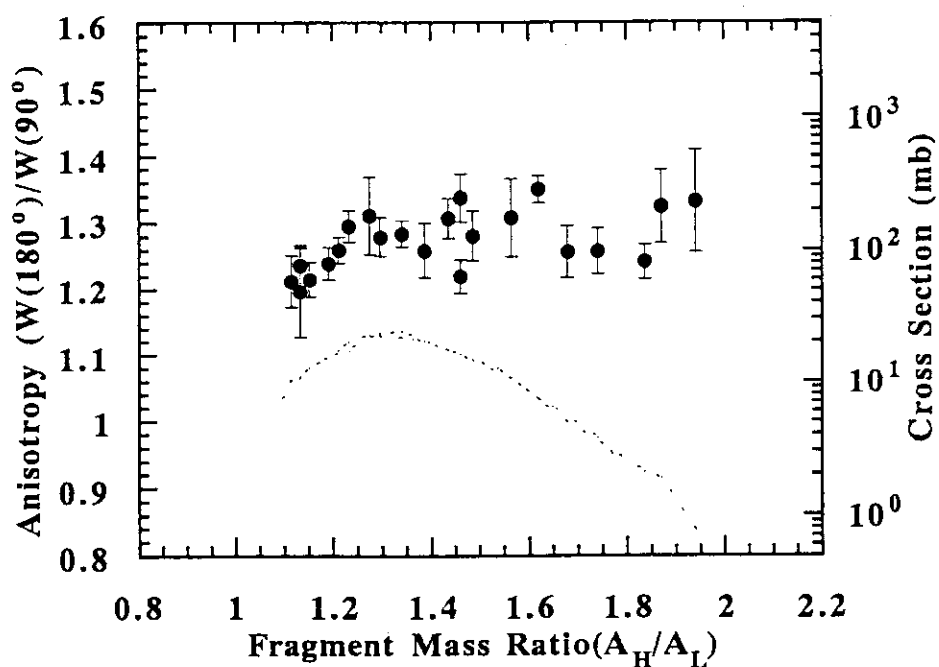


Fig. 4 Dependence of angular anisotropy on fragment-mass ratio in the 15 MeV proton-induced fission of ^{244}Pu . The dashed curve is the mass yield curve for the 15 MeV proton-induced fission of ^{244}Pu .

3.9 Isotopic Distributions of Fission Products from Neutron Deficient Nuclei in Light Actinide Region

Ichiro NISHINAKA, Masashi TANIKAWA, Shinya MIYAMOTO,
Keisuke SUEKI, Hiromichi NAKAHARA, Tsutomu OHTSUKI[†],
Kazuaki TSUKADA*, Masaaki MAGARA*, Toshiaki SEKINE**,
Yuichi HATSUKAWA**, Yuichiro NAGAME**, and Hiroshi IKEZOE***

Department of Chemistry, Tokyo Metropolitan University,

[†]Laboratory of Nuclear Science, Tohoku University,

*Department of Chemistry, **Department of Radioisotopes,

***Department of Physics, JAERI

In recent study¹⁾ it is verified that there are two independent deformation paths in fission phenomena, namely two different fission barriers leading to two kinds of scission configurations. The aim of this work is to observe how mass division phenomena, symmetric and asymmetric, are correlated with the neutron number of the fissioning nuclide in the region of light actinides. Use of heavy ion beams only allows an investigation of nuclear fission of neutron deficient nuclides because no target nuclide is available for the study of this region by light particles. In heavy ion reactions, however, the excitation energy of the compound nucleus becomes high even with the incident beam energy near the Coulomb barrier. Thus, it is likely that the shell effects which are considered to be related to asymmetric mass division disappear at high excitation energy. Some studies^{2,3)} on the fission of neutron deficient nuclei formed by heavy ion reactions were carried out but no experimental evidence was observed on the asymmetric mass division component in mass yield curve. In our previous experiment⁴⁾, we reported an observation of some component in the energy spectrum of fission fragments produced in $^{18}\text{O} + ^{209}\text{Bi}$. However, the fragment energies were measured for the fragments that passed through a window and two cathode foils of the PPAC, and the correction for the energy loss was more than 10 MeV in some cases. In present experiments, the detection system was improved for more precise measurement of kinetic energy of fission fragments.

Two reactions, $^{18}\text{O} + ^{209}\text{Bi}$ and $^{16}\text{O} + ^{209}\text{Bi}$, were carried out. ^{18}O (85 MeV) and ^{16}O (86, 98 MeV) beams were supplied by the JAERI tandem accelerator. The target used was 50 $\mu\text{g}/\text{cm}^2$ bismuth metal evaporated onto a 10 $\mu\text{g}/\text{cm}^2$ carbon backing. The time of flight and kinetic energy of fission fragments were measured in coincidence at an angle of 60° with respect to the beam. The start detector of the time of flight measurement was a micro-channel-plate detector (MCPD) consisted of a 10 $\mu\text{g}/\text{cm}^2$ carbon foil and a micro-channel-plate. The stop detector was a SSD of a small solid angle (0.3 msr) which measured kinetic energy. In the experiment for $^{16}\text{O} + ^{209}\text{Bi}$, another MCPD was placed in front of the SSD as a stop detector. The flight paths were 103.4 cm and 93.3 cm for ^{18}O , $^{16}\text{O} + ^{209}\text{Bi}$ reactions, respectively. In order to distinguish fission fragments

from the beam scattered by the target, the complementary fragment was detected in coincidence by a position sensitive parallel-plate-avalanche counter (PPAC) located on the opposite side about 35 cm from the target at the angle of about 100° with respect to the beam. In each experiment, 350 MeV ^{127}I beam was bombarded onto thin (about $50 \mu\text{g}/\text{cm}^2$) calibration targets which were prepared by evaporation of Ag, In, and Sb onto $10 \mu\text{g}/\text{cm}^2$ carbon backing foils, in order to make precise absolute calibration of energy and time of flight. For the 78 MeV ^{18}O elastically scattered particle, the time resolution was 0.2 nsec in terms of the full width at half maximum (FWHM) and the energy resolution was 0.4 MeV (FWHM) in the experiment of the $^{18}\text{O} + ^{209}\text{Bi}$ reaction. The mass resolution was 3.7 amu (FWHM) for In recoil particles. The resolutions of the detection systems were similar in the experiment for $^{16}\text{O} + ^{209}\text{Bi}$ reaction.

The number of fission events observed were 2.8×10^4 , 5.0×10^4 and 2.2×10^4 for ^{18}O (85 MeV) + ^{209}Bi , ^{16}O (86, 98 MeV) + ^{209}Bi , respectively. Figures 1 and 2 show the velocity and the kinetic energy distributions of fission fragments in the center-of-mass system. In the velocity distributions there seems to be some structure at around $0.048 V_{\text{CM}}/c$. Figure 3 shows mass yield curves derived from velocity and kinetic energy of fragments. The mean mass is 3~4 amu less than the half value of the compound mass, which corresponds to the average number of neutrons evaporated from fissioning nuclei before fission and from fission fragments after fission. The observed mass distribution in each system is, as a whole, nearly symmetric with the width of $\sigma_A = 14.5$ amu. However, there seems to be some asymmetric component in the mass distribution observed at the incident beam energies near the Coulomb barriers. Especially in the mass yield curve of $^{18}\text{O} + ^{209}\text{Bi}$ reaction, shoulders are observed clearly at around mass number 90 and 135. Figure 4 shows three mass yield curves of fission observed for compound nuclei, with the same atomic number but with different numbers of neutron ^{225}Pa ($N=134$), ^{227}Pa ($N=136$) and ^{233}Pa ($N=142$)^{5). They were produced by different reactions but at the same excitation energy of 32 MeV. The solid lines in this figure indicate the results of three Gaussian fit. From this fitting, the asymmetric component is about 10% for $^{225,227}\text{Pa}$ and about 60% for ^{233}Pa . In the fission of Pa nuclei, the mass division characteristic drastically changes as the neutron number changes from about 136 to 142.}

References

- 1) T. Ohstuki, Y. Nagame, H. Ikezoe, K. Tsukada, K. Sueki, and H. Nakahara, Phys. Rev. Lett. **66** (1991) 17.
- 2) B. D. Wikins, B. B. Back, H.-G. Clerc, J. E. Gindler, B. G. Clagola, and L. E. Gledenin, Dynamics of Nuclear Fission and Related Collective Phenomena, Springer-Verlag, New York, (1981) p145.
- 3) H. M. Blann, Phys. Rev. **123** (1961) 1356.
- 4) I. Nishinaka et. al, JAERI TANDEM LINAC & V.D.G Annual Report, (1991) 113.
- 5) I. F. Croall and J. G. Cuninghame, Nucl. Phys. A **128** (1969) 402.

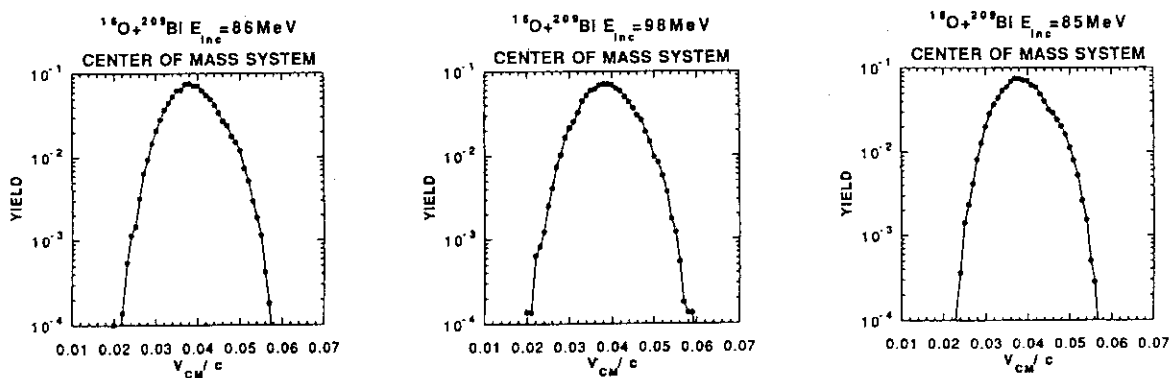


Fig.1 Velocity distributions of fission fragments

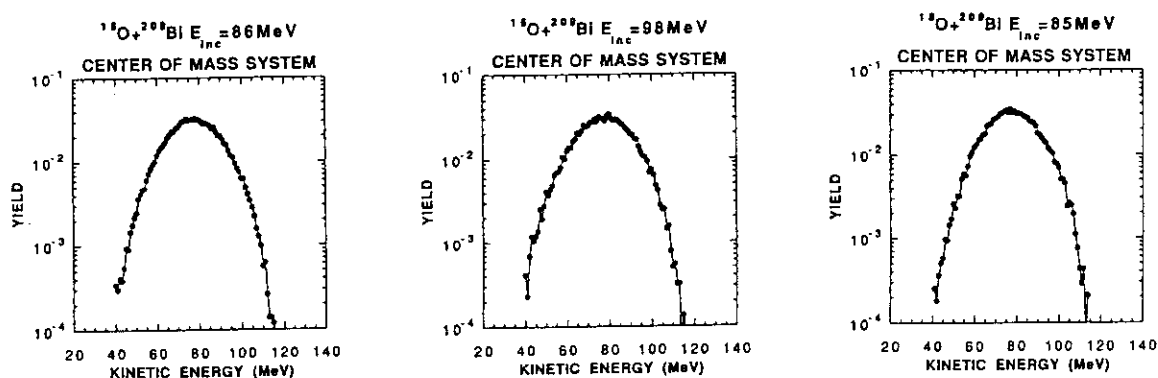


Fig.2 Kinetic energy distributions of fission fragments

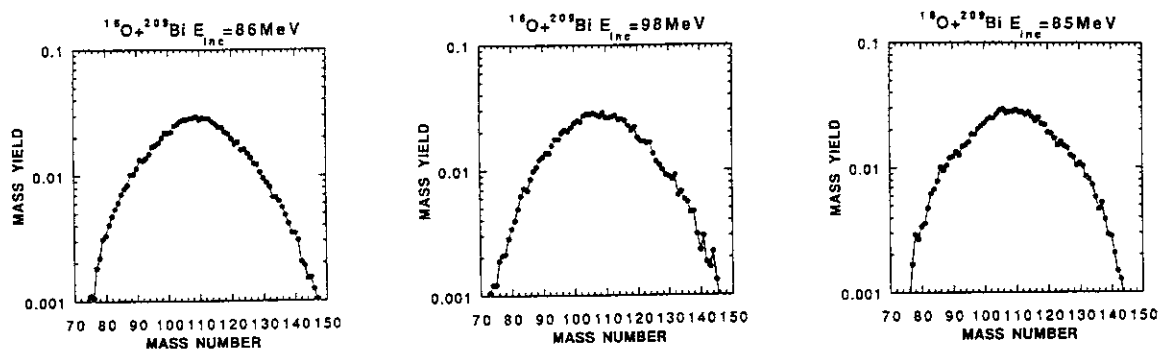
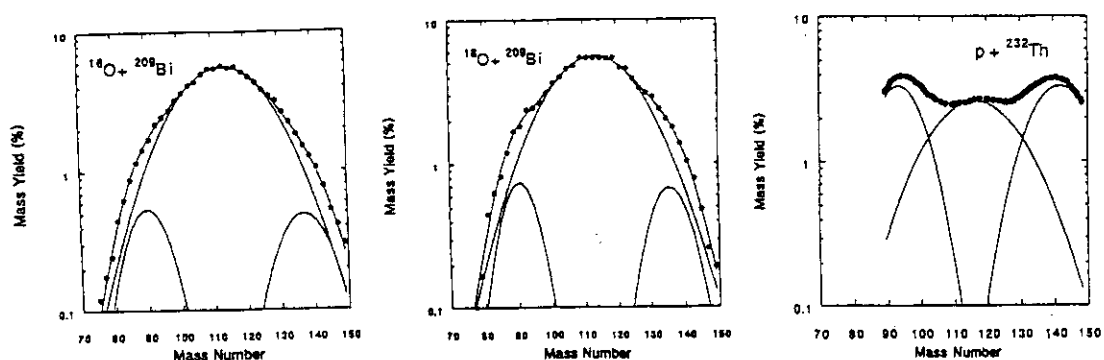


Fig.3 Mass distributions of fission fragments

Fig.4 Mass distributions of fission fragments in the reactions $^{16}\text{O}+^{209}\text{Bi}$, $^{18}\text{O}+^{209}\text{Bi}$ and $p+^{232}\text{Th}^{5)}$. Excitation energy of the compound nucleus is 32MeV in all reactions.

3.10 Fragment Mass and Kinetic Energy Distributions in Heavy Ion Induced Fission at Sub-barrier Energy Region

Yuichiro NAGAME, Hiroshi IKEZOE*, Kazuaki TSUKADA, Yuichi
HATSUKAWA, Masaaki MAGARA, Masumi OSHIMA*, Tsutomu
OHTSUKI**, Reiji SASAKI**, Yuka AOKI**, Jirota KASAGI** and
Ichiro NISHINAKA***

*Department of Radioisotopes, *Department of Physics, JAERI*

***Laboratory of Nuclear Science, Tohoku University*

****Department of Chemistry, Tokyo Metropolitan University*

To search for the multi-mode fission process in neutron deficient heavy actinides around $Z=100$ at excitation energy of $E^* = 20 - 40$ MeV, we measured fragment mass and kinetic energy distributions in heavy ion induced fission at sub-barrier energy region.

The experiments were carried out at the JAERI tandem accelerator using the ^{35}Cl beam with an incident energy of 176 MeV to bombard a ^{209}Bi target. Fission fragments were measured with a double velocity technique using time-of-flight (TOF) telescopes. Start and stop signals were delivered with a microchannel plate equipped with a carbon foil and a position sensitive parallel-plate avalanche counter. The fission fragment mass M and total kinetic energy E_{TKE} were obtained from the center-of-mass velocities v_1 and v_2 of pair fragments,

$$M = \frac{M_f}{1 + v_1/v_2}, \quad (1)$$

$$E_{TKE} = \frac{1}{2} M_f v_1 v_2. \quad (2)$$

where M_f denotes the mass number of the fissioning nucleus ^{244}Fm .

The preliminary mass and total kinetic energy distributions are shown in Figs. 1 and 2, respectively. The gross feature of these distributions observed in this system ($E^* \sim 35$ MeV) is nearly symmetric. The mean value $\langle E_{TKE} \rangle$ of about 196 MeV in Fig. 2 is in good agreement with the expected value from the empirical formula of Viola *et al.*¹⁾. Detailed analysis on the widths and structures of the mass and TKE distributions is in progress.

Reference

- 1). V. E. Viola *et al.*, Phys. Rev. C **31** (1985) 1550.

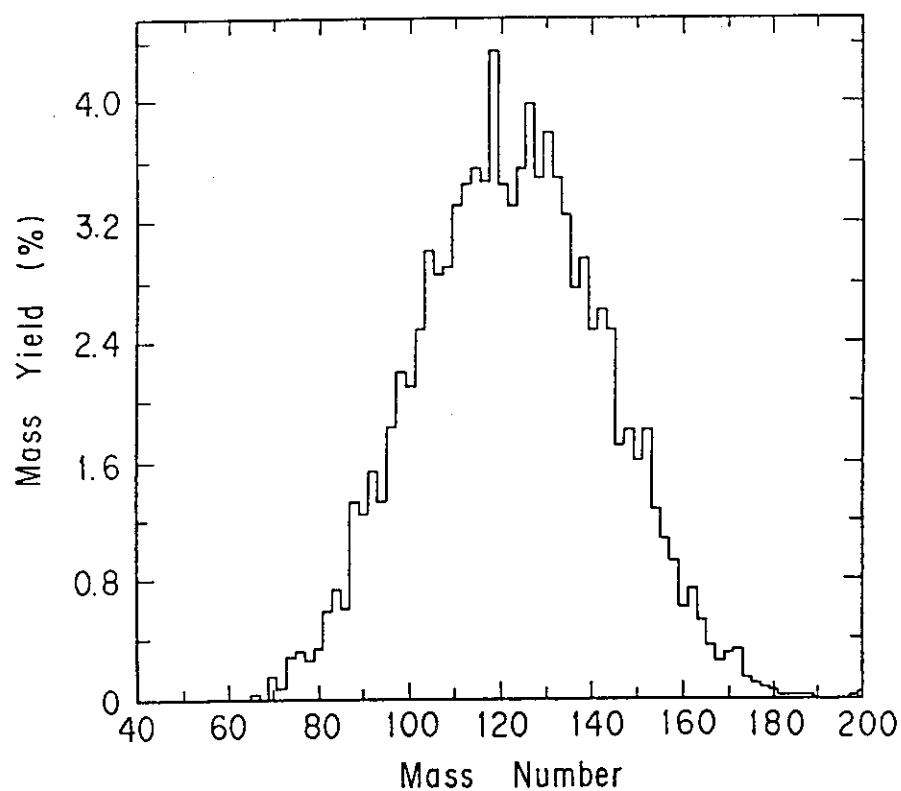


Fig. 1. Mass distribution of fission fragments measured for the reaction induced by ^{35}Cl on ^{209}Bi at $E_{\text{lab}} = 176$ MeV.

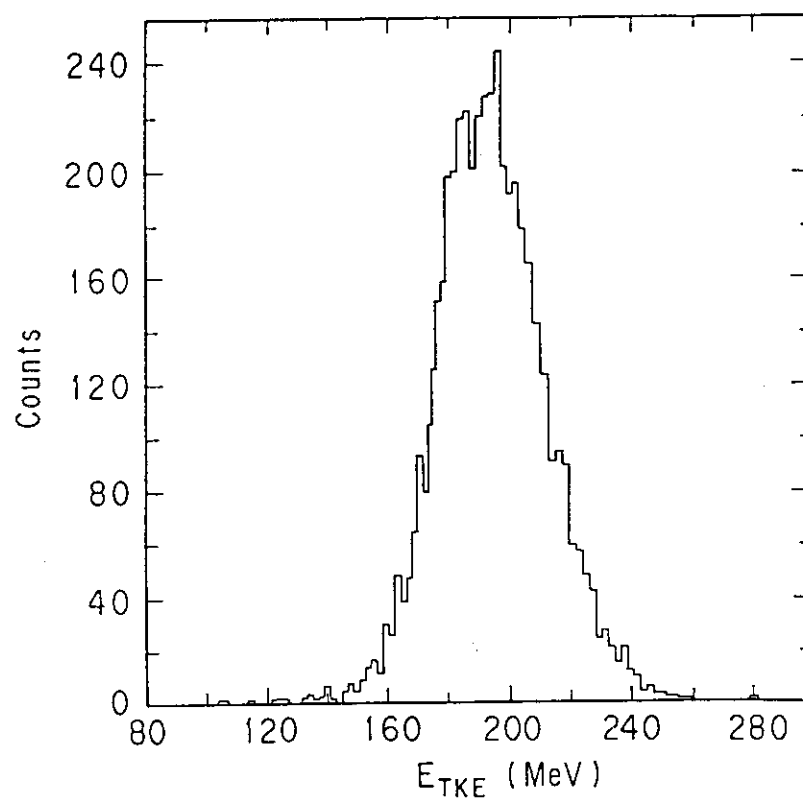


Fig. 2. Total kinetic energy distribution of fission fragments measured for the reaction induced by ^{35}Cl on ^{209}Bi at $E_{\text{lab}} = 176$ MeV.

IV. LIGHT ION NUCLEAR PHYSICS

4.1 Measurement of Double Differential Charged-particle Emission Cross Sections for Reactions Induced by 26 MeV Protons

Yukinobu WATANABE*, Hironori KASHIMOTO*, Hironao SAKAKI*,
Yoshihide KOYAMA*, Hiroyuki SHINOHARA*, Tadahisa
MICHIBATA*, Yukinori KANDA*, Norihiko KOORI**, Satoshi
CHIBA+, Tokio FUKAHORI+, Kazuo HASEGAWA+, Motoharu
MIZUMOTO+ and Shinichirou MEIGO+

*Department of Energy Conversion Engineering, Kyushu University,

**College of General Education, The University of Tokushima,

+Department of Reactor Engineering, JAERI

Double differential charged-particle emission cross sections have been measured for proton-induced reactions on ^{12}C , ^{27}Al , ^{106}Pd , ^{159}Tb , and ^{181}Ta at 26 MeV, in order to investigate preequilibrium process and multiparticle breakup process. The measured (p,xp) and (p, α) energy spectra are compared with those calculated using a code EXIFON based on the statistical multistep direct and compound (SMD/SMC) model.

Introduction

Charged-particle nuclear data at intermediate energies ranging from 20 MeV to a few GeV are required for various fields such as accelerator, medical and space applications. A feature of nuclear reactions in such incident energy range is that the observed energy spectra has a large continuous portion with forward-peaked angular distribution which arises from preequilibrium particle emission. This work has been planned in the extension of the measurements performed using the Kyushu University tandem accelerator in 10 - 20 MeV region^{1,2}. The aim is to investigate the preequilibrium process in nucleon-induced reactions with medium-heavy nuclei and multibody breakup process in those with light nuclei, and to apply the results to nuclear data evaluation in the intermediate energy range.

In the present work, the measurement of double differential charged-particle emission cross sections has been carried out for ^{12}C , ^{27}Al , ^{106}Pd , ^{159}Tb , and ^{181}Ta at 26 MeV, following that of Si and ^{98}Mo at 25.6 MeV in 1991 fiscal year³⁻⁵. The experimental (p,xp) and (p, α) spectra are analyzed using a code EXIFON based on the SMD-SMC model⁶.

Experimental Procedure

The experiment was performed using a 26 MeV proton beam from the JAERI tandem

accelerator. The details of the experimental procedure and the data processing have been reported elsewhere³⁻⁵).

The proton beam was transported in a 50 cm ϕ scattering chamber which was installed in the N1 beam line; its current varied from about 50 nA to 300 nA, depending on the experimental condition. The following targets were chosen: ^{nat}C (0.1 mg/cm²), ^{27}Al (0.303 mg/cm²), ^{106}Pd (1.02 mg/cm²), ^{159}Tb (0.994 mg/cm²), and ^{181}Ta (1.05 mg/cm²). All of them were self-supporting foils with their thickness given in the above parenthesis. A charged particle detecting system consisted of a ΔE -E counter telescope having three silicon surface barrier detectors. Energy spectra of emitted charged particles were measured at intervals of 10° between 30° and 150°.

Experimental results

In Fig.1, the measured double differential (p,xp) cross sections for ^{106}Pd are shown by closed circles. The observed spectra have the continuum region between 10 and 20 MeV and the angular distributions are peaked forward. This indicates that the preequilibrium process or the direct process is dominant in this energy region. Fig. 2 shows the experimental energy spectra of α particles emitted into 40°, 90°, and 150° for ^{106}Pd . Compared with the proton spectra in Fig.1, the α spectrum has a larger contribution from compound process that is seen as an appreciable evaporation peak around 12 MeV. The preequilibrium region with forward peaked angular distributions is also observed at energies above 17 MeV.

Analyses and discussion

The SMD/SMC model⁶), one of quantum-mechanical models, was applied to calculations of double differential cross sections of protons, neutrons and α particles. The code EXIFON, which was modified in part so as to include the correction of recoil energy, was employed. The angular distributions were calculated using the systematics of Kumabe et al.⁷) as an input option. The strength of effective nucleon-nucleon interaction was fixed to be the recommended value of 27.5 MeV. Other input parameters were set to the default values, except a pairing energy and a phonon width; only the pairing energy of a residual nucleus was set to zero in the calculation of SMD process of (p,p') scattering and the phonon width was taken as 0.3 MeV, corresponding to the experimental energy resolution.

The calculated results for the $^{106}\text{Pd}(\text{p},\text{xp})$ reaction are shown by solid lines in Fig. 1 and for the (p, α) reaction in Fig.2. The calculated (p,xp) spectra are in overall good agreement with the experimental ones. However, underestimation of a few tens of percents is seen at low outgoing energies below 15 MeV at forward angles. This may be due to underprediction of the SMD component leading to forward peaked angular distribution, because the experimental angular distributions are still forward peaked. Compared with the

(p,xp) spectra, the calculated (p, α) spectra do not reproduce the experimental ones quite well in shape and in magnitude as shown in Fig.2. Similar results were obtained in comparison between the experimental⁸⁾ and calculated spectra for 15 and 18 MeV (p, α) reactions on ^{106}Pd . The reason remains open at present. Similar analysis is in progress for ^{27}Al , ^{159}Tb , and ^{181}Ta .

Furthermore, simultaneous analysis of (p,p') and (p, α) spectra for ^{12}C has been performed to investigate multibody breakup processes. From the preliminary result, it was found that there is a large contribution from three-body simultaneous breakup process (p + α + ^8Be) in both spectra and the measured (p, α) spectra are reproduced by a Monte Carlo simulation under the assumption of the sequential decay from highly excited resonant and non-resonant states of ^{12}C . More detailed analysis is now in progress.

Summary

We have performed the experiment to measure the double differential cross sections of emitted charged-particles from proton-induced reactions on ^{12}C , ^{27}Al , ^{106}Pd , ^{159}Tb , and ^{181}Ta over a wide range of mass number at 26 MeV. The EXFION calculations with the systematics given by Kumabe et al.⁷⁾ showed overall good agreement with the experimental (p,xp) spectra, although the calculated (p, α) spectra for ^{106}Pd were not in agreement with the experimental ones in both shape and magnitude. Further study about composite particle emission will be necessary to resolve the disagreement.

Finally, the authors wish to thank the members of the accelerator division of JAERI for their kind help during the experiment. One of the authors (Y.W) is also indebted to Dr. H. Kalka for the use of his code EXFION.

References

- 1) Y. Watanabe et al., *Proceedings of the XX th Int. Symp. on Nuclear Physics, Nuclear Reaction Mechanism*, Germany, Nov. 12-16, 1990, pp. 151.
- 2) Y. Watanabe et al., *Proceedings of Intt. Conf. on Nuclear Data for Science and Technology*, May 13-17, 1991, Jülich, Germany, (Springer-Verlag), pp. 1002.
- 3) A. Aoto et al., *Proceedings of the 1991 Seminar on Nuclear Data*, JAERI-M 92-027, (1992), pp. 330.
- 4) Y. Watanabe et al. JAERI tandem annual report 1992.
- 5) Y. Watanabe et al., *Proceedings of the 1992 Seminar on Nuclear Data*, JAERI-M 93-046, (1993) pp. 297
- 6) H. Kalka, *Z. Phys. A341*, 289 (1992); private communication (1991).
- 7) I. Kumabe et al., *Nucl. Scie. & Eng.* **104**, 280 (1990).
- 8) I. Kumabe et al., *Phys. Rev. C* **35**, 467 (1987).

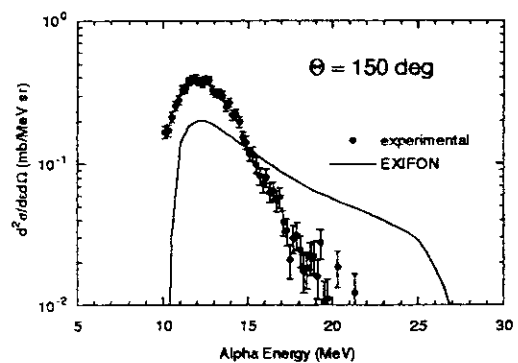
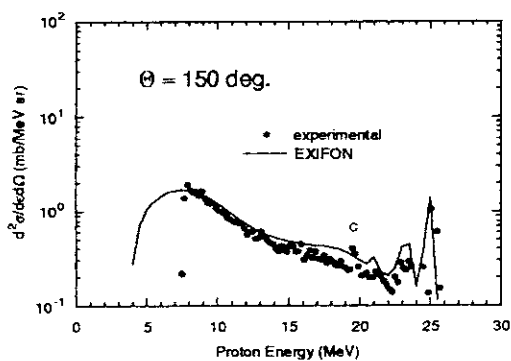
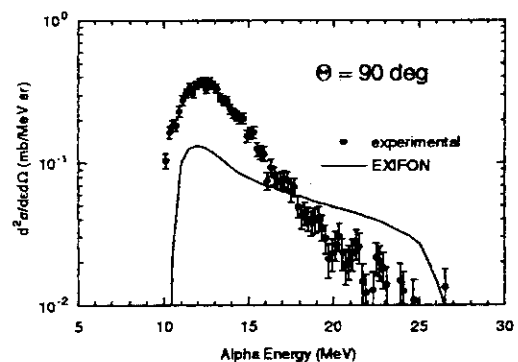
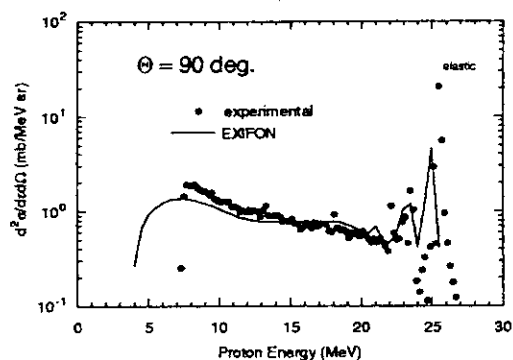
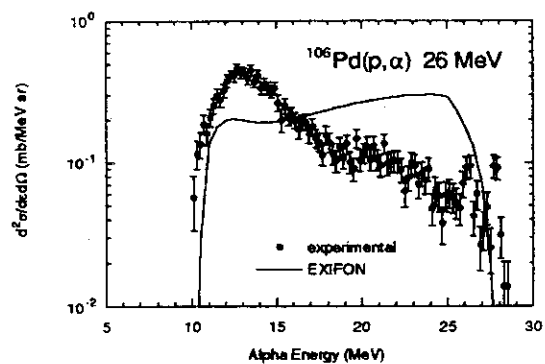
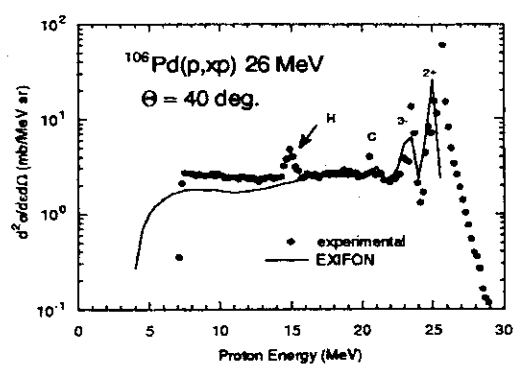


Fig.1 Experimental double differential cross sections of the (p,xp) reaction on ^{106}Pd at 26 MeV and those calculated using the code EXIFON.

Fig.2 Experimental double differential cross sections of the (p,α) reaction on ^{106}Pd at 26 MeV and those calculated using the code EXIFON.

4.2 Measurement of Double-differential α -production Cross Section of Fe and Ni for 7.9 - 10.6 MeV Neutrons

Mamoru BABA, Nobuo ITO, Isamu MATSUYAMA, Shigeo MATSUYAMA
Satoshi CHIBA*, Tokio FUKAHORI*, Motoharu MIZUMOTO*,
Kazuo HASEGAWA* and Sin-ichiro MEIGO*

Faculty of Engineering, Tohoku University,

*Department of Reactor Engineering, JAERI

1. Introduction

Differential cross section data for fast neutron induced α -production reactions are of prime importance for the evaluation of radiation damage, nuclear heating and transmutation in fusion reactors. The data status, however, is not satisfactory as indicated by large discrepancies among the evaluated data files. To improve the situation, systematic experimental data are required to provide practical data base and to supplement theoretical calculations.

We have continued the measurement of energy-angular doubly-differential α -production cross sections (DDXs) at the JAERI tandem accelerator using a very high efficiency α -particle spectrometer, and obtained the data of Fe and Ni for 7.9, 9.0, 9.7 and 10.6 MeV neutrons.

2. Experiment

Primary neutrons were produced by the D(d,n) reaction using a diatomic deuteron beam from the JAERI tandem accelerator and a deuterium gas target.

The α -spectrometer is a gridded-ionization-chamber (GIC)¹⁻²⁾ which was specially developed for study of fast neutron induced α -production reactions. Figure 1 illustrates the schematic view of the GIC. It is a twin GIC with a common cathode and has almost 4π geometry for α -particles emitted from the sample. Besides, the energy and emission angle of α -particles can be determined using the anode and cathode signals, if particles are stopped between the cathode and grid. The present GIC enables α -particle measurements with low backgrounds even for fast neutrons by employing high-Z elements for electrodes (Ta, W) and for counting gas (Kr). For further background reduction, a copper collimator was employed to define incident neutrons within sample diameter.

In the present experiment, the following modification was undertaken to improve the GIC performance: 1) A CH₄(5%) gas was newly employed as the moderating gas for Kr in place of CO₂(3.5%) used in the previous experiment to avoid backgrounds due to the O(n, α) reaction. 2) The data acquisition system was extended to enable simultaneous measurement for both the hemispheres. The pressure of the counting gas was set to make the range of the most energetic

α -particles slightly shorter than the cathode-grid distance to reduce the contribution of lighter particles p, d, t and ^3He . The samples were metallic foils of elemental Ni and Fe, 3- μm , thick and mounted on a sample changer. Backgrounds were measured by replacing the sample foils with a Au foil (1- μm thick). Figure 2 shows an example of anode-cathode two dimensional spectrum. α -particle events are observed clearly within the area expected from the GIC parameters.

The energy and fluence of incident neutrons were determined by a NE213 scintillator and a Si-surface-barrier detector placed behind the GIC. The backgrounds due to break up source neutrons proved to be negligible in the energy range of the present experiment from the measurement with a ^3He gas in the neutron production gas cell.

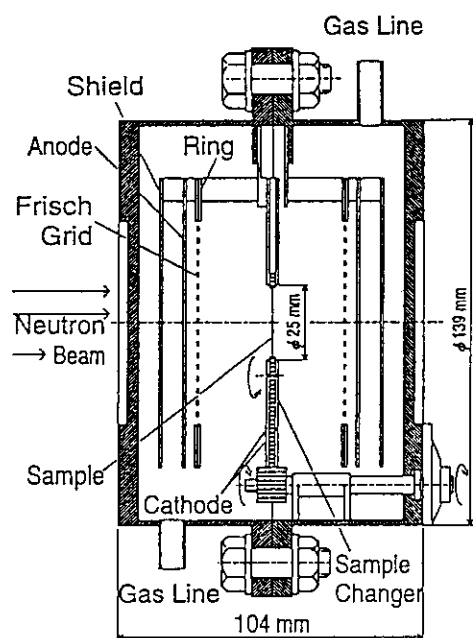


Fig.1: Schematic view of the gridded-ionization-chamber

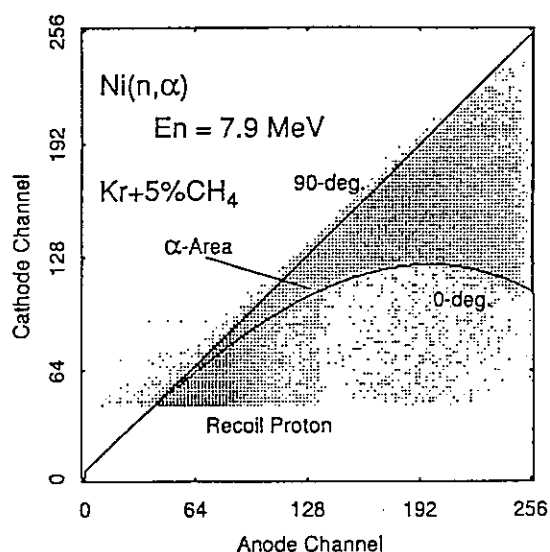


Fig.2: Anode-cathode two-dimensional spectrum in the (n,α) experiment

3. Results and Discussion

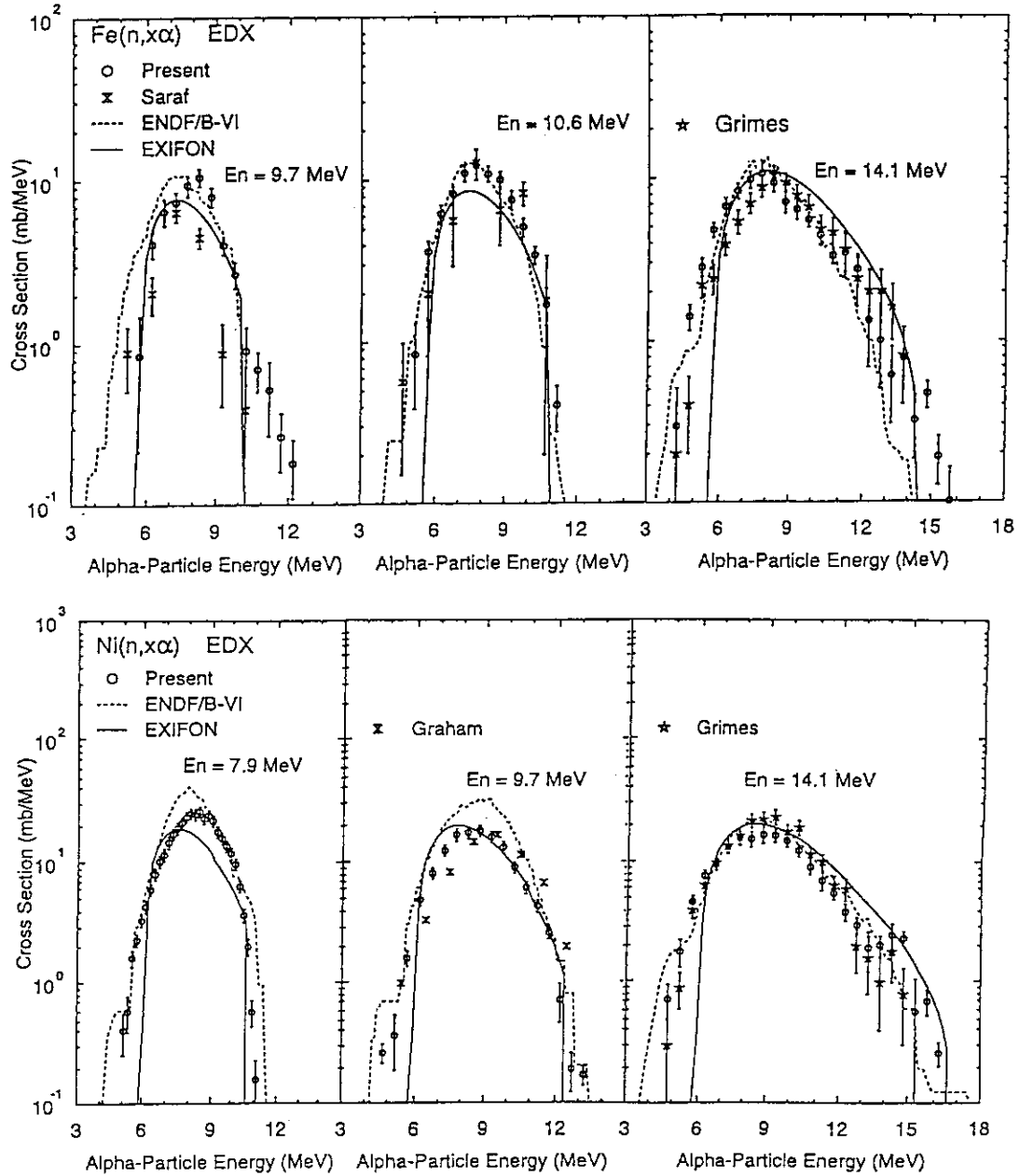
By correcting the experimental data for background particles and energy loss within samples, we deduced the DDXs, angular distributions and angle-integrated cross sections. The cross section was determined relative to the n-p scattering cross section by measuring recoil protons.

The results of angle-integrated α -particle spectra are shown in Fig.3 including 14 MeV data at Tohoku University, together with other experiments^{4,6)}, the evaluation and the calculation by the multi-step statistical model code EXIFON³⁾. The α -particle spectra are nearly free from distinct structures and, combined with almost isotropic angular distributions²⁾, suggest that the reaction

proceeds through the compound reaction. It is noted that the data by Saraf et al.⁶⁾ for Fe at 9.7 MeV are only about one half in magnitude of the present result while their value at 10.5 MeV are fairly close to ours. The ENDF/B-VI data for Ni are systematically higher than the present ones by around 40 % whereas they are similar in shape of α -particle spectrum. It is striking that the α -particle spectra calculated by the EXIFON differ markedly from the present data since the code reproduces very well the experimental data in the cases of neutron emission spectra. The difference in the α -particle spectra will be attributable primarily to the inappropriate optical-model potential for α -particle and/or level-density parameters inherent to (n, α) reactions. This will lead to large uncertainty in the excitation functions of (n, α) reactions calculated by the code. The present results for α -particle spectrum will provide useful information to trace the problem.

References

- 1) M.Baba et al.: Proc.Int.Conf."Nuclear Data for Science & Technol.," (May, 1991 Jülich) p.477,
- 2) N.Ito et al.: JAERI-M 93-045 (1992) p.334
- 3) H.Kalka et al.: Phys. Rev., C40(1989) 1619
- 4) S.M.Grims et al.:Phys. Rev., C19(1979) 2127
- 5) S.L.Graham et al.:Nucl. Sci. Eng., 95(1987) 60
- 6) S.K.Saraf et al.: Nucl. Sci. Eng., 107(1991) 365

Fig.3: Angle-integrated α -emission spectra of Fe and Ni

4.3 Measurement of Neutron Activation Cross Sections at 9.1, 10.1, 11.1 and 11.8 MeV Using $^1\text{H}(^{11}\text{B},n)^{11}\text{C}$ Neutron Source at TANDEM Facility at JAERI

Yujiro IKEDA, Satoshi CHIBA, Tokio FUKAHORI, Kazuo HASEGAWA,
Motoharu MIZUMOTO, Shinichiro MEIGO and Hiroshi MAEKAWA

Department of Reactor Engineering, JAERI

1. Introduction

Continuous program on activation cross section measurements for important dosimetry reactions at an energy range from 9 to 13 MeV has been underway by using a neutron source incorporated with $^1\text{H}(^{11}\text{B},n)^{11}\text{C}$ reaction.¹⁾ The present report gives the most recent results of the cross section measurements for the reactions listed in Table 1 along with associated nuclear data²⁾.

2. Experiment

The neutron energies applied were 9.1, 10.1, 11.1 and 11.8 MeV which corresponded to ^{11}B beams with energies of 55, 57, 60 and 63 MeV, respectively, incident into a $^1\text{H}_2$ gas target. In addition to the irradiation with gas in, separate irradiation with gas out was performed for each energy in order to subtract the parasitic neutrons due to interaction of ^{11}B beam with the target structure. The neutron spectra in the forward direction with respect to the ^{11}B beam direction were measured with the TOF technique incorporated with two NE213 scintillation spectrometers.

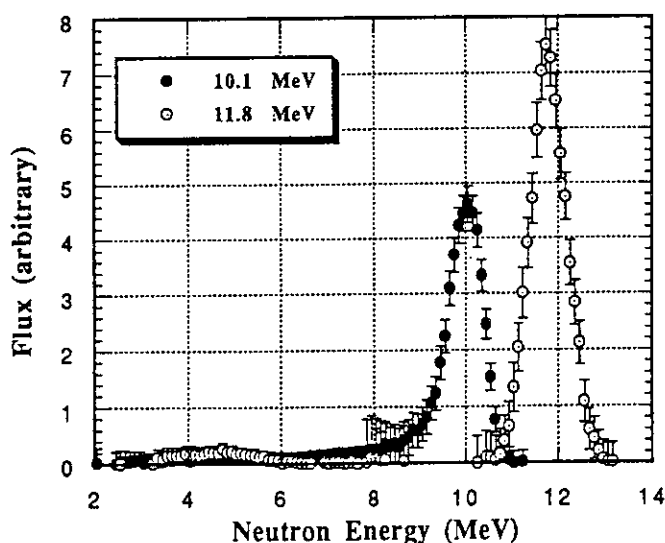


Fig. 1 Neutron spectra at 10.1 and 11.8 MeV.

Figure 1 shows net neutron spectra for 10.1 and 11.8 MeV. Obviously, they look broadened at the peak energy regions. This was attributable to insufficient time resolution in the TOF measurement. Stacked foils of Ti, V, Fe, Co, Zn, Zr and Nb sandwiched with both Al and Au monitor foils were irradiated at a distance of 100 mm from the center of target cell for 11 hours for runs with gas in and for 3 to 4 hours with gas out. After irradiation for each run, activities were measured with Ge detectors and reaction rates were deduced by performing necessary corrections in terms of decay times, natural abundance,

detector efficiency, γ -ray self absorption, and so forth. The neutron flux was determined from the reaction rate of monitor reaction of $^{27}\text{Al}(n,\alpha)^{24}\text{Na}$, the cross section value of which was taken from IRDF-90³⁾. The neutron flux at each foil was derived by interpolating reaction rates of

$^{27}\text{Al}(n,\alpha)^{24}\text{Na}$ on both front and rear sides. The spectra were used not only in the determination of mean reaction energy, but also in the correction for the low energy neutron component to the net reaction rate of interest. Fortunately, the correction for the low energy neutron contribution was not serious because of rather high threshold energy of almost all reactions, except for $^{64}\text{Zn}(n,p)^{64}\text{Cu}$, threshold energy of which is around 1 MeV. Most dominant experimental error arose in the reaction rate due to poor statistics of γ -ray counts. This was simply because of low neutron yields in the present operation of ^{11}B beam.

3. Results

The present results are summarized in Table 2. The presently measured cross sections of $^{56}\text{Fe}(n,p)^{56}\text{Mn}$, $^{59}\text{Co}(n,\alpha)^{56}\text{Mn}$, $^{90}\text{Zr}(n,p)^{90\text{m}}\text{Y}$, $^{93}\text{Nb}(n,\alpha)^{90\text{m}}\text{Y}$, $^{93}\text{Nb}(n,2n)^{92\text{m}}\text{Nb}$ and $^{197}\text{Au}(n,2n)^{196}\text{Au}$ are plotted in Figs. 2.1 to 2.6, along with comprehensive evaluations and experimental data in the literature. Although the experimental errors are large due low activity production by weak $^1\text{H}(^{11}\text{B},n)$ source strength, the new experimental values are of importance in the particular energy region.

References

- 1) Y. Ikeda, et al., Proc. Intl. Conf. on Nucl. Data for Sci. & Technol., Jülich, Germany, 13-17 May 1991 (issued in 1992: Editor S. M. Qaim) pp. 294-296.
- 2) Browne, E. and Firestone, R. B. (Shirley, V. S., Editor): "Table of Radioactive Isotopes" A Wiley-Interscience Publication, John Wiley & Sons (1986).
- 3) KOCHEROV, N. P. and VONACH, H.: "The International Reactor Dosimetry File (IRDF-90)," Proc. of the Seventh ASTM-EURATOM Symp. on Reactor Dosimetry, Strasbourg, France, 27-31 August (1990) pp357-361.

Table 1 Reactions Investigated and Associated Decay Data

Reaction	Half-life	Abundance	γ -Energy	γ -ray branching	Atomic mass
1. $^{48}\text{Ti}(n,p)^{48}\text{Sc}$	1.821 d	0.737	983.5	1.0	47.88
2. $^{51}\text{V}(n,\alpha)^{48}\text{Sc}$	1.821 d	0.9975	983.5	1.0	50.9415
3. $^{56}\text{Fe}(n,p)^{56}\text{Mn}$	2.5785 h	0.9172	846.81	0.989	55.847
4. $^{59}\text{Co}(n,\alpha)^{56}\text{Mn}$	2.5785 h	1.0	846.81	0.989	58.9332
5. $^{64}\text{Zn}(n,p)^{64}\text{Cu}$	12.701 h	0.486	511	0.358	65.39
6. $^{90}\text{Zr}(n,p)^{90\text{m}}\text{Y}$	3.19 h	0.5145	202.5	0.966	91.224
7. $^{93}\text{Nb}(n,2n)^{92\text{m}}\text{Nb}$	10.15 d	1.0	934.53	0.990	92.9064
8. $^{93}\text{Nb}(n,\alpha)^{90\text{m}}\text{Y}$	3.19 h	1.0	202.5	0.966	92.9064
9. $^{197}\text{Au}(n,2n)^{196}\text{Au}$	6.183 d	1.0	355.58	0.87	196.9665
10. $^{27}\text{Al}(n,\alpha)^{24}\text{Na}^*$	15.02 h	1.0	1368.6	1.0	26.98154

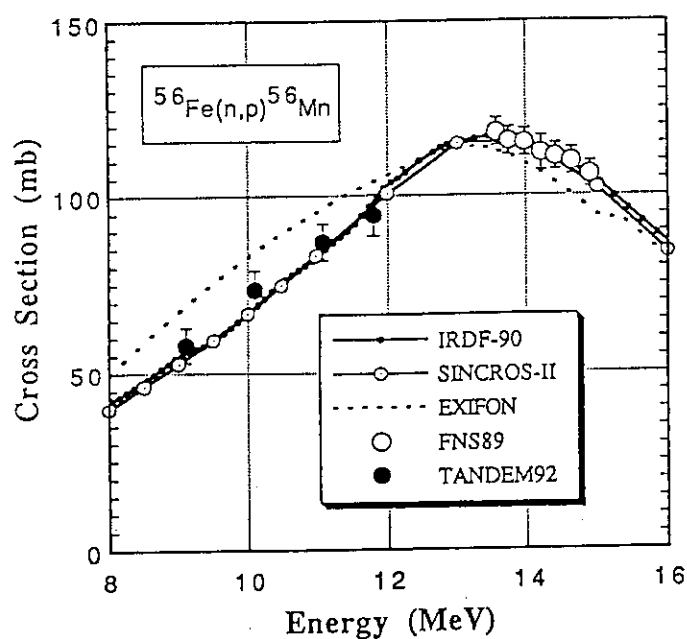
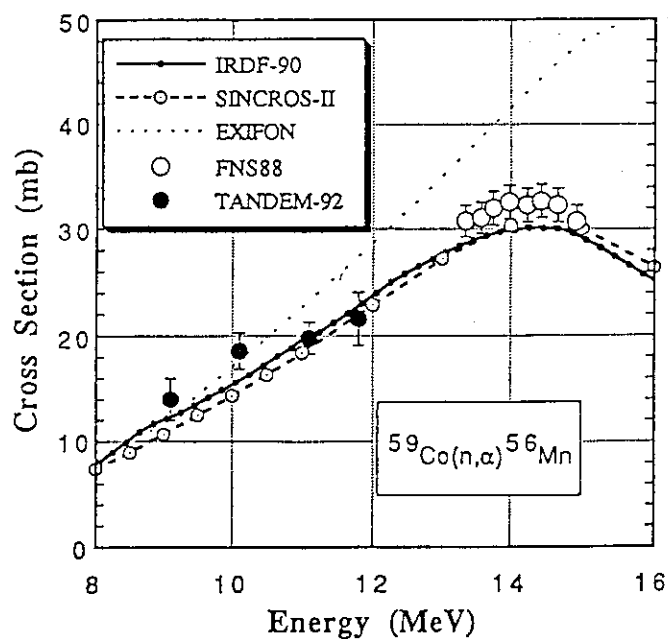
* Monitor Reactions

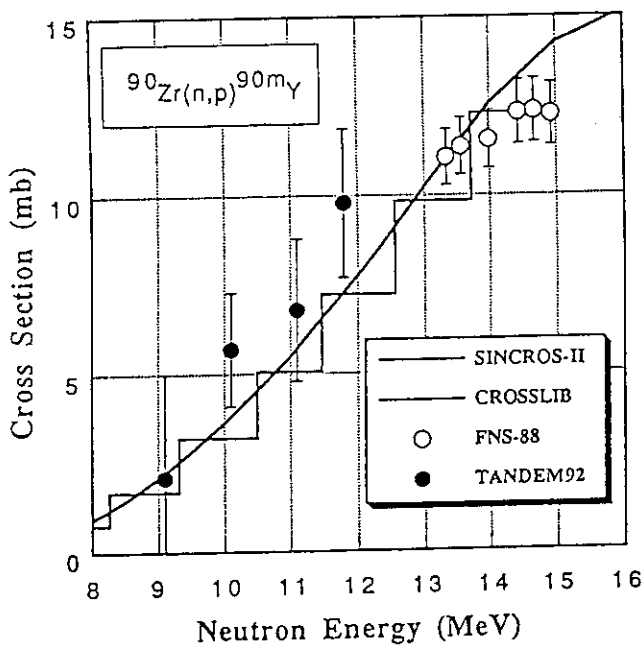
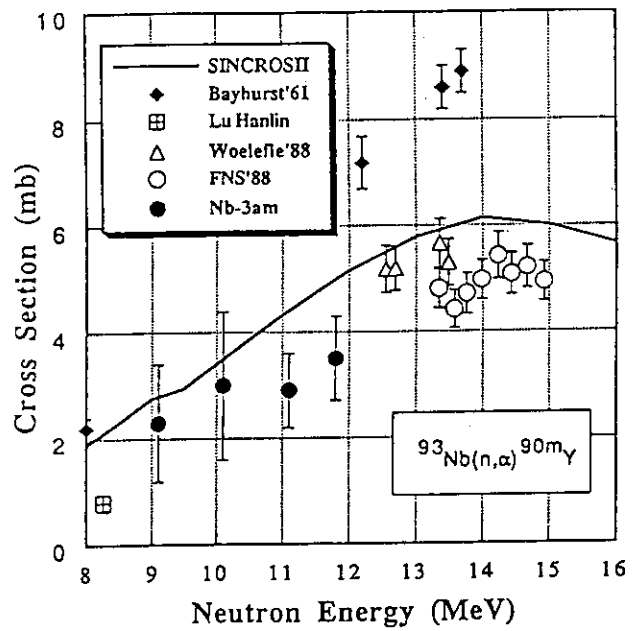
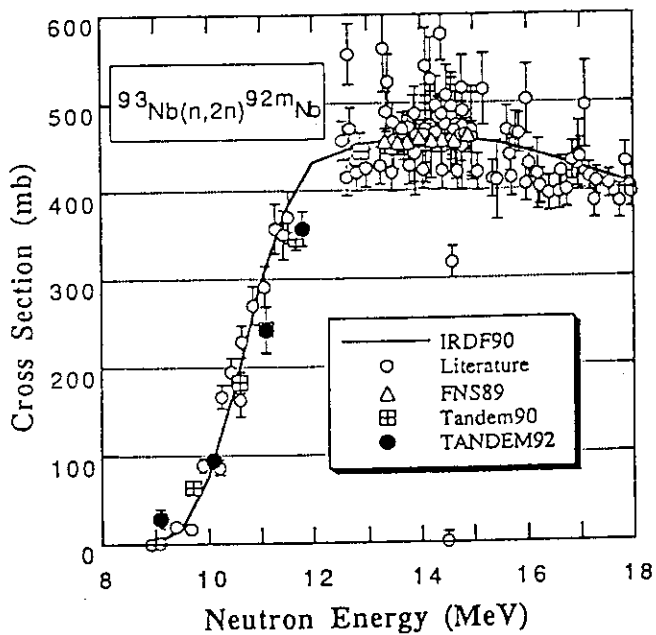
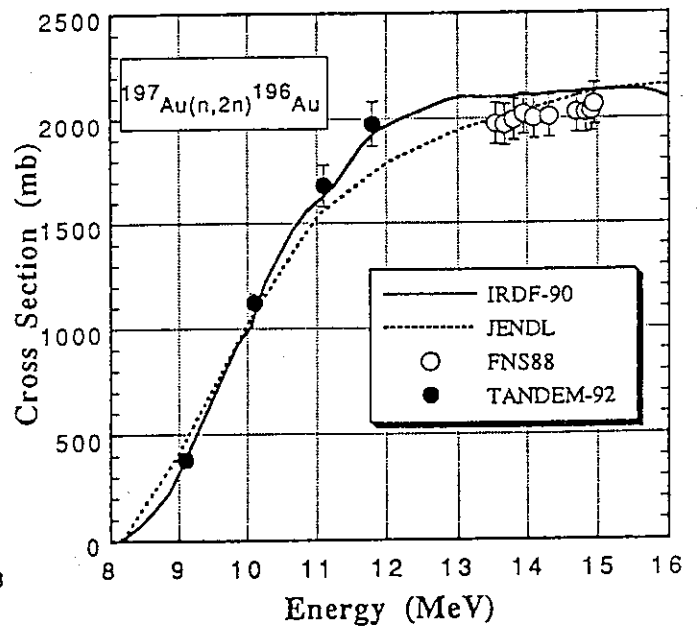
* Data are taken from Table of Radioactive Isotopes.

Table 2 Results of Cross Section Measurements

Reaction	Cross Section (mb)			
	9.1 MeV	10.1 MeV	11.1 MeV	11.8 MeV
$^{48}\text{Ti}(n,p)^{48}\text{Sc}$	26.0 ± 2.1	-----	-----	-----
$^{51}\text{V}(n,\alpha)^{48}\text{Sc}$	4.9 ± 2.0	4.2 ± 1.0	9.1 ± 1.2	
$^{56}\text{Fe}(n,p)^{56}\text{Mn}$	58.0 ± 5.0	73.6 ± 5.4	86.9 ± 5.2	94.5 ± 6.0
$^{59}\text{Co}(n,\alpha)^{56}\text{Mn}$	12.8 ± 1.8	18.6 ± 1.7	19.8 ± 1.5	21.6 ± 2.5
$^{64}\text{Zn}(n,p)^{64}\text{Cu}$	$287. \pm 30.$	$282. \pm 23.$	$288. \pm 18.$	$293. \pm 31.$
$^{90}\text{Zr}(n,p)^{90\text{m}}\text{Y}$	$2.1(+2.9, -1.0)$	5.7 ± 1.6	6.8 ± 2.0	9.8 ± 2.1
$^{93}\text{Nb}(n,2n)^{92\text{m}}\text{Nb}$	$29. \pm 11.$	94.5 ± 8.7	$242. \pm 27.$	$357. \pm 20.$
$^{93}\text{Nb}(n,\alpha)^{90\text{m}}\text{Y}$	2.3 ± 1.1	3.0 ± 1.4	2.9 ± 0.7	3.5 ± 0.8
$^{197}\text{Au}(n,2n)^{196}\text{Au}$	$379. \pm 40.$	$1124. \pm 45.$	$1680. \pm 100.$	$1976. \pm 110.$
$^{27}\text{Al}(n,\alpha)^{24}\text{Na} *$	73.83	89.03	109.06	115.87

* Monitor Reaction; Cross section data are referred from IRDF-90

Fig. 2.1 Cross section of $^{56}\text{Fe}(n,p)^{56}\text{Mn}$ Fig. 2.2 Cross section of $^{59}\text{Co}(n,\alpha)^{56}\text{Mn}$

Fig. 2.3 Cross section of $^{90}\text{Zr}(n,p)^{90m}\text{Y}$ Fig. 2.4 Cross section of $^{93}\text{Nb}(n,\alpha)^{90m}\text{Y}$ Fig. 2.5 Cross section of $^{93}\text{Nb}(n,2n)^{92m}\text{Nb}$ Fig. 2.6 Cross Section of $^{197}\text{Au}(n,2n)^{196}\text{Au}$

V. HEAVY ION NUCLEAR PHYSICS

5.1 Scattering of 115MeV ^{12}C from ^{52}Cr and ^{58}Ni

Yoshimaro YAMANOUTI, Yasuharu SUGIYAMA, Yoshiaki TOMITA
and Kazumi IDENO

Department of Physics, JAERI

The optical model potential plays an extremely important role for the description of heavy-ion scattering. In order to study the systematics of the optical potential for the heavy ion-intermediate nucleus interaction, differential cross sections for elastic and inelastic scattering of 115MeV ^{12}C from ^{52}Cr and ^{58}Ni were measured. The experimental data were analyzed by the coupled-channel formalism with the phenomenological optical potential and the semimicroscopic optical potential calculated with the double folding model, and thus the reaction mechanism of the heavy ion scattering was investigated.

The scattering cross sections were measured using 115MeV $^{12}\text{C}^{6+}$ beam from the tandem accelerator at JAERI. Targets were made by vacuum evaporation onto $\sim 10\mu\text{g}/\text{cm}^2$ carbon foils, and were $216\mu\text{g}/\text{cm}^2$ thick for ^{52}Cr (99.90% enriched metal) and $230\mu\text{g}/\text{cm}^2$ thick for ^{58}Ni (99.76% enriched metal), respectively. Reaction products were detected in a 40cm long hybrid focal plane detector placed in the focal plane of a magnetic spectrograph. The absolute normalization of the cross sections was obtained by comparing with Rutherford scattering at the most forward angle. Angular distribution data were measured for elastic scattering and inelastic scattering to the first 2^+ and 3^- excited states over the angular range from 6° to 45° lab. The experimental cross sections for ^{52}Cr are shown in fig.1 together with theoretical prediction.

The coupled-channel analysis of the elastic and inelastic scattering data was carried out with the phenomenological optical model potentials. The calculations were performed with the computer codes ECIS79 and CHUCK2. The real and volume-imaginary central potentials with the Woods-Saxon form factors and a Coulomb potential were employed in the analysis. Starting potential parameters were obtained from the result¹⁾ of 98MeV ^{12}C scattering from ^{90}Zr . And the deformation parameters were taken from the compila-

tion²⁾ of Raman et al. The coupled-channel calculations well reproduced the experimental cross sections for ^{52}Cr and ^{58}Ni without adjustment of the starting parameters.

The double folding potentials were generated by the folding of an effective nucleon-nucleon interaction with the projectile and target density distributions³⁾. The density distribution for ^{12}C was chosen to be a three parameter Fermi shape. The ground state densities for ^{52}Cr and ^{58}Ni were two parameter Fermi shapes with parameters derived from electron scattering. The densities appearing in the folding model calculations are the matter densities, therefore the charge densities derived from electron scattering were transformed to the matter densities. The neutron density was assumed to be $\rho_n = (N/Z) \rho_p$. The M3Y effective interaction of Bertsch⁴⁾ was used in the folding model calculations.

For the inelastic scattering the ground state densities are replaced by the transition densities. The Tassie type form factor for the transition density was adopted. And the transition densities were normalized to the reduced transition probability $B(E\lambda)$. The folding potentials were calculated using the computer code DFPOT⁵⁾. These potentials were then supplied to the code CHUCK2 for the coupled-channel calculations. The imaginary potential was treated phenomenologically, i.e. the same parameters as the volume imaginary potential¹⁾ for ^{90}Zr were used. Good fits to the experimental data for ^{52}Cr and ^{58}Ni were obtained with the double folding procedure. The calculated result in the case of ^{52}Cr is shown in fig.1. The solid curves represent the calculation with the real folding potential and the real Tassie type form factor. The optimum renormalization factor for the folding potential was 0.8.

References

- 1) S.T.Thornton and D.E.Gustafson, Phys.Rev. C13 (1976) 1502
- 2) S.Raman, C.W.Nestor, Jr., S.Kahane and K.H.Bhatt, Atomic Data and Nucl. Data Tables, 42(1989)1
- 3) G.R.Satchler and W.G.Love, Phys.Rep. 55(1979)183
- 4) G.Bertsch, J.Borysowicz, H.McManus and W.G.Love, Nucl.Phys. A284(1977)399
- 5) J.Cook, Comp.Phys.Comm. 25(1982)125

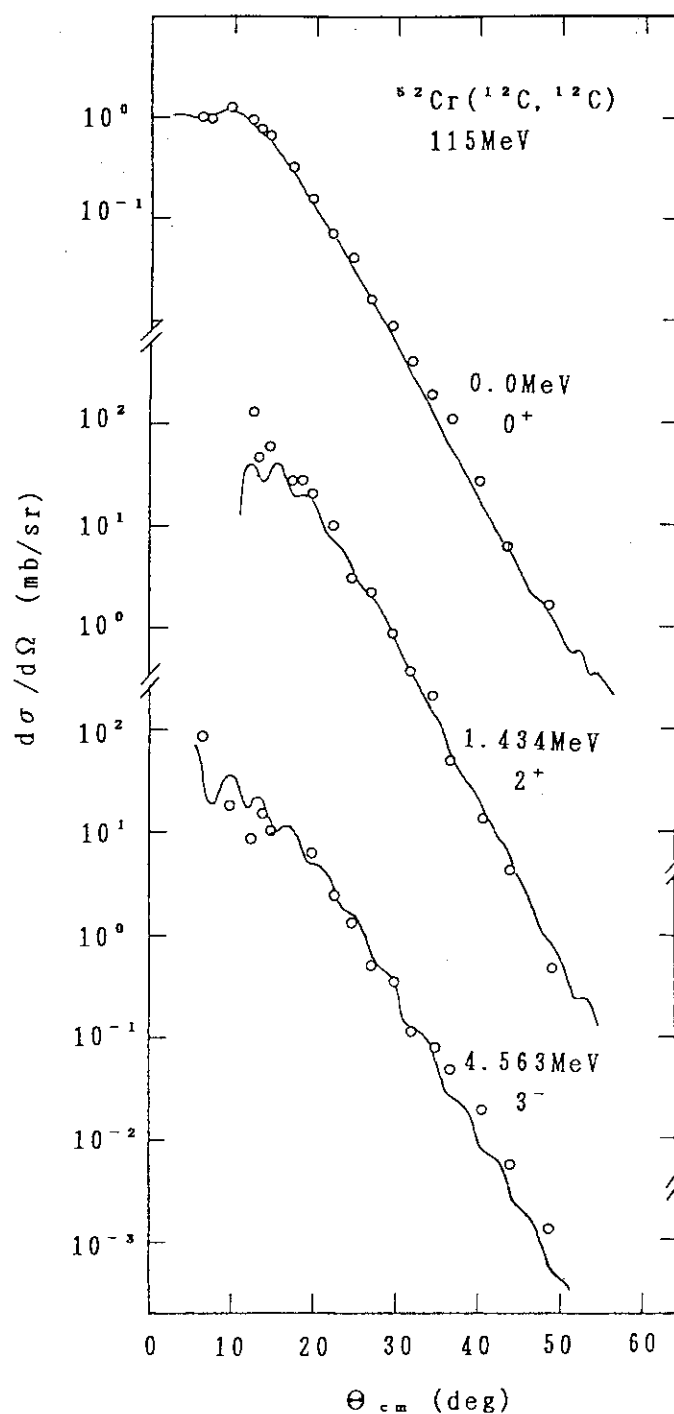


Fig.1 Experimental cross sections (open circles) and the coupled-channel prediction with the double folding model potential and the Tassie type form factor. The cross section divided by Rutherford's cross section is displayed for the elastic scattering.

5.2 Observation of Airy Oscillation for the $^{16}\text{O}+^{16}\text{O}$ System at $E_{\text{lab}}=145\text{MeV}$

Yasuharu SUGIYAMA, Yoshiaki TOMITA, Hiroshi IKEZOE,
Yoshimaro YAMANOUCI, Kazumi IDENO, Singo HAMADA,
Tsuyoshi SUGIMITSU*, Masayuki HIJIIYA* and Yoshio KONDO**

Department of Physics, JAERI, *Department of Physics, Kyushu University, **Department of Natural Science, Kyoto Women's University

Recent observation^{1,2)} of nuclear rainbow scattering in the $^{16}\text{O}+^{16}\text{O}$ system at $E_{\text{lab}}=350\text{MeV}$ has attracted considerable interest in this system, since this phenomenon is believed to provide important information on the depth of the real nucleus-nucleus interaction³⁾. As far as we know, this is the clearest example of rainbow phenomena in heavy ion scattering ($A>6$). Subsequent analyses⁴⁻⁷⁾ of the data show that the wide peak at $\theta_{\text{cm}}\approx 50^\circ$ is likely to be the first Airy maximum rather than the second maximum suggested by the analysis of ref. 1) and that the potential is likely to be the type A of ref. 4). On the other hand, the type X potential of refs. 5,7) and the analysis of ref. 8) do not favor a rainbow interpretation for the scattering data. In this respect, it is interesting to see whether "rainbow" phenomena persist at other energies. In this report, we describe our measurements of the elastic scattering angular distribution for the $^{16}\text{O}+^{16}\text{O}$ system at $E_{\text{lab}}=145\text{MeV}$ and show the existence of the nuclear rainbow phenomenon at this energy.

The measurements have been performed with the ^{16}O beam of 145 MeV at the JAERI tandem accelerator using the heavy ion magnetic spectrograph "ENMA"⁹⁾. A V_2O_5 target of about $200\text{ }\mu\text{g}/\text{cm}^2$ thickness was used. Particles were detected in the focal plane with a hybrid counter¹⁰⁾ which consisted of resistive wire detectors, an ionization detector and a plastic scintillator to enable the simultaneous measurement of position, energy-loss and particle energy. We identified the particle by the $\delta E/E$ measurement. The elastic scattering cross sections from $\theta_{\text{lab}}=5.5^\circ$ to 21.0° were measured in steps of 0.5° with a horizontal opening of 0.5° for the entrance aperture of the spectrograph. For the backward angles from $\theta_{\text{lab}}=21.0^\circ$ to 35.0° , the cross sections were measured in steps of 1° with the horizontal opening of 1° . The absolute zero angle was calibrated

by measuring the elastic yield for ^{16}O on ^{208}Pb at small angles for both sides of the incident beam. The absolute cross sections were obtained for ^{16}O on ^{51}V at small angles from Rutherford scattering and for $^{16}\text{O}+^{16}\text{O}$ from the 2:5 ratio between ^{51}V and ^{16}O in V_2O_5 .

The measured elastic scattering angular distribution is shown in fig.1. The data show strong Fraunhofer oscillations at forward angles followed by a dip at $\theta_{\text{cm}} \approx 54^\circ$ and a modulated gross peak centered at $\theta_{\text{cm}} \approx 62^\circ$. We have performed χ^2 searches on the present data using the following six-parameter optical potential form:

$$U(r) = V_C(R_C^t, R_C^p; r) - \frac{V}{\{1 + \exp[(r - R_R)/a_R]\}^2} - \frac{iW}{\{1 + \exp[(r - R_I)/a_I]\}^2}$$

The Coulomb potential, $V_C(R_C^t, R_C^p; r)$, has been calculated assuming uniform charge distributions of radii R_C^t for the target nucleus and R_C^p for the projectile nucleus¹¹⁾, where $R_C^t = R_C^p = 3.533$ fm is chosen to

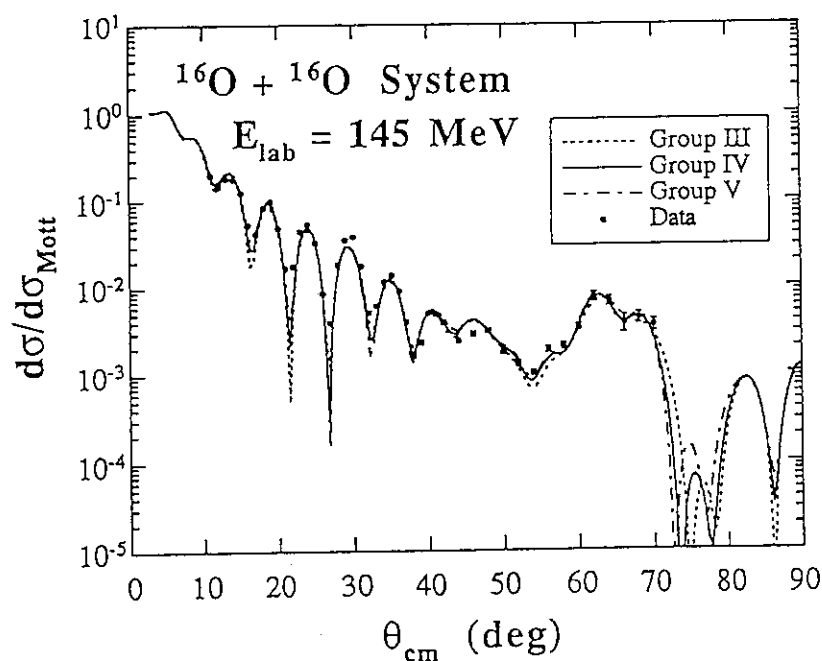


Fig.1 Comparison between the elastic scattering angular distributions, calculated with optical potential III (dotted curve), IV (solid curve) and V (dash-dotted curve), and the present data. The cross sections are shown as Mott ratios.

reproduce the observed value of the root-mean-square radius for the charge density distribution of the ^{16}O nucleus¹²⁾. Following the analysis of ref.⁴⁾, the Woods-Saxon form factor raised to the power 2 has been used for both real and imaginary parts. To obtain better reproduction of the data at large angles, the present χ^2 searches have been performed assuming the same percentage uncertainty at all data points rather than using the experimental error. A similar method has been previously adopted in ref. 5). The value of the constant percentage will produce a different χ^2 value, but the resulting fit will be identical to the fit obtained with the 10% error.

Table 1 lists potential parameters which correspond to six local χ^2 minima (potential I to VI) obtained in the present analysis. These potentials differ mainly in their real depth. Fig.1 compares the calculated elastic scattering angular distributions for the three optical potentials III (dotted curve), IV (solid curve) and V (dash-dotted curve), with the present data for the $^{16}\text{O}+^{16}\text{O}$ system at $E_{\text{lab}}=145\text{MeV}$. The three results provide good fits to the experimental data and have similar χ^2 values (see table 1). These fits are almost identical except for regions of angular minima and $70^\circ \leq \theta_{\text{cm}} \leq 80^\circ$.

We now show a possibility of choosing the proper optical potential at this energy following the discussion of ref.⁴⁾. In ref.⁴⁾, the potential A has been chosen to be the proper potential for $^{16}\text{O}+^{16}\text{O}$ system at $E_{\text{lab}}=350\text{MeV}$, based on the dispersion relation¹³⁾ between the real and imaginary parts of the optical potential and the results of ref.¹⁴⁾ for the successful analyses of the low-energy resonant phenomena in this system. It should be noted that this choice of the optical potential has been achieved before the large angle scattering data²⁾ become available. Subsequent analysis⁵⁻⁷⁾ of the full elastic scattering data^{1,2)} support type A potentials. Fig.2 shows real volume integrals per nucleon pair j_V for the optical potentials of table 1 together with the figure 4 of ref.⁴⁾. The dotted curve shows the energy dependence which is consistent with the dispersion relation. It can be seen that the volume integral for potential IV agrees with the proposed energy dependence very well. All the other potentials of table 1 do not agree with the systematics. The energy dependence of real volume integral j_V shown in fig.2 agrees with the values found for other systems and at other energies¹⁵⁾.

In summary, we have measured the elastic scattering angular distribution at $E_{\text{lab}}=145\text{ MeV}$ for the $^{16}\text{O}+^{16}\text{O}$ system, for which nuclear

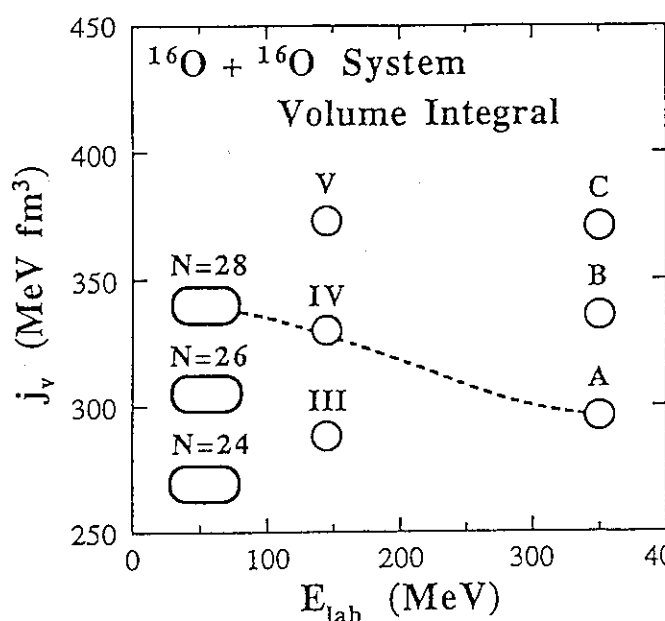


Fig.2 Volume integral per nucleon pair j_v for the real part of the optical potential as a function of the laboratory energy. At $E_{\text{lab}}=145$ MeV, the volume integrals for the potentials III, IV and V of table 1 are shown. Other values and the dotted curve are those of the figure 4 of ref.⁴). It can be seen that the potential IV agrees with the predicted systematics.

rainbow scattering has been observed at $E_{\text{lab}}=350$ MeV. Analysis of the present data shows that the observed dip at $\theta_{\text{cm}} \approx 54^\circ$ and the modulated peak at $\theta_{\text{cm}} \approx 62^\circ$ are an Airy minimum and an Airy maximum, respectively. We found several discrete sets of optical potentials which fit the data. The optical potential IV of table 1 provides a real volume integral which agrees with the previously proposed energy dependence.

References

- 1) E.Stiliaris et al. Phys. Lett. B223(1989)291.
- 2) E.Stiliaris et al., Annual report 1989, HMI-Report 482(1990)50.
- 3) D.A.Goldberg and S.M.Smith, Phys.Rev.Lett.29(1972)500.
- 4) Y.Kondo et al.,Phys. Lett. B242(1990)340.
- 5) M.E.Brandan and G.R.Satchler, Phys.Lett.B256(1991)311.
- 6) D.T.Khoa et al., Phys.Lett. B260(1991)278.
- 7) M.E.Brandan et al., Phys.Lett. B281(1992)185.
- 8) L.J.Allen et al., Phys.Lett.B298(1993)36.
- 9) Y.Sugiyama et al., Nucl. Instrum. Methods A281(1989)512.
- 10) E.Takekoshi et al., Nucl. Instrum. Methods A237(1985)512.
- 11) A.K.Jain et al., Phys. Rev. C12(1975)801.
- 12) H. de Vries et al., At. Data Nucl. Data Tables 36(1987)495.
- 13) M.A.Nagarajan et al., Phys. Rev. Lett. 54(1985)1136.
- 14) Y.Kondo et al., Phys.Lett.B227(1989)310.
- 15) M.E.Brandan et al., Phys. Rev.C41(1990)1520.

Table 1 Potential parameters for the Woods-Saxon squared potentials. The potential form factor of eq. (1) is used. The real volume integral per nucleon pair (j_v) is also listed for each potential.

Group	V (MeV)	R_R (fm)	a_R (fm)	W (MeV)	R_I (fm)	a_I (fm)	j_v (MeV fm ³)	χ^2
I	-120.7	5.313	1.218	-16.42	6.835	1.015	211	461
II	-208.6	4.742	1.333	-17.97	6.709	0.994	264	470
III	-362.0	3.920	1.560	-15.49	6.808	0.896	288	330
IV	-413.0	3.968	1.466	-16.83	6.759	0.931	330	284
V	-469.8	3.989	1.398	-18.22	6.703	0.976	373	282
VI	-532.8	3.993	1.347	-19.63	6.643	1.020	419	291

5.3 Study of ^{164}Dy with Multiple Coulomb Excitation

Hideshige KUSAKARI*, Masanobu KIMURA*, Masumi OSHIMA, Masahiko Sugawara**, Tsuneyasu MORIKAWA***, Shin-ichi ICHIKAWA****, and Takashi INAMURA***

Department of Physics, JAERI, *Faculty of Education, Chiba University, **Chiba Institute of Technology, ***RIKEN, ****Department of Chemistry, JAERI

The nucleus ^{164}Dy seems to have good rotational ground- and gamma-bands^{1,2)}. The excitation energy of the first 2^+ level is 73.4 keV, and the ratio between those of the 2_1^+ and 4_1^+ levels is $E(4^+)/E(2^+) = 3.30$. The ^{164}Dy nucleus does not show the backbending phenomenon in those two bands. The moment-of-inertia of the ground-band is almost constant, but slightly increases with spin I . We intended to investigate experimentally the transition probabilities of ^{164}Dy in order to extract the higher order effect of nuclear collective motion.

We measured intensities of gamma-rays following the multiple-coulomb excitation (MCE) of ^{164}Dy with 60 MeV O, 130 MeV S, 240 MeV Ni beams from the tandem accelerator. The metallic ^{164}Dy target was 1.8 mg/cm^2 in thickness (95% isotopically enriched). Positions of scattered projectiles and recoiled nuclei were detected by four parallel-plate avalanche counters in coincidence with deexcitation gamma-rays following MCE. The scattered projectiles were analyzed in the angular ranges of $\theta=102.9-150.5$ for the S beam and $\theta=102.9-130.5$ for the Ni beam. Energies of measured gamma-rays were corrected for the Doppler shift, event by event. Intensities of transitions were obtained from gamma-ray intensities after correction for conversion electrons. We have simulated the intensities of transi-

tions using the multiple-coulomb excitation code³⁾. Excited members of the ground-band (up to 16^+) and of the gamma-band (up to 12^+) have been included in this simulation. The transition probability of ^{164}Dy was deduced by a fit to the experimental intensities.

The results are shown in figs. 1-3 in comparison with that of the neighboring nucleus ^{168}Er [ref.4]. In fig. 1, the matrix elements for the $I_g=6^+$ and 8^+ states decrease below the rigid-rotor model predictions. This is different from the case of ^{168}Er . However, an obvious increase of the matrix element over the rigid-rotor model prediction can be seen for the higher spin states in the both nuclei. In fig. 2, the reduction of the matrix elements for the transitions from the $I_\gamma=8^+$ and 10^+ states is obvious. A similar phenomenon was reported in ^{168}Er . It is difficult to reproduce such a reduction with recent theoretical models.

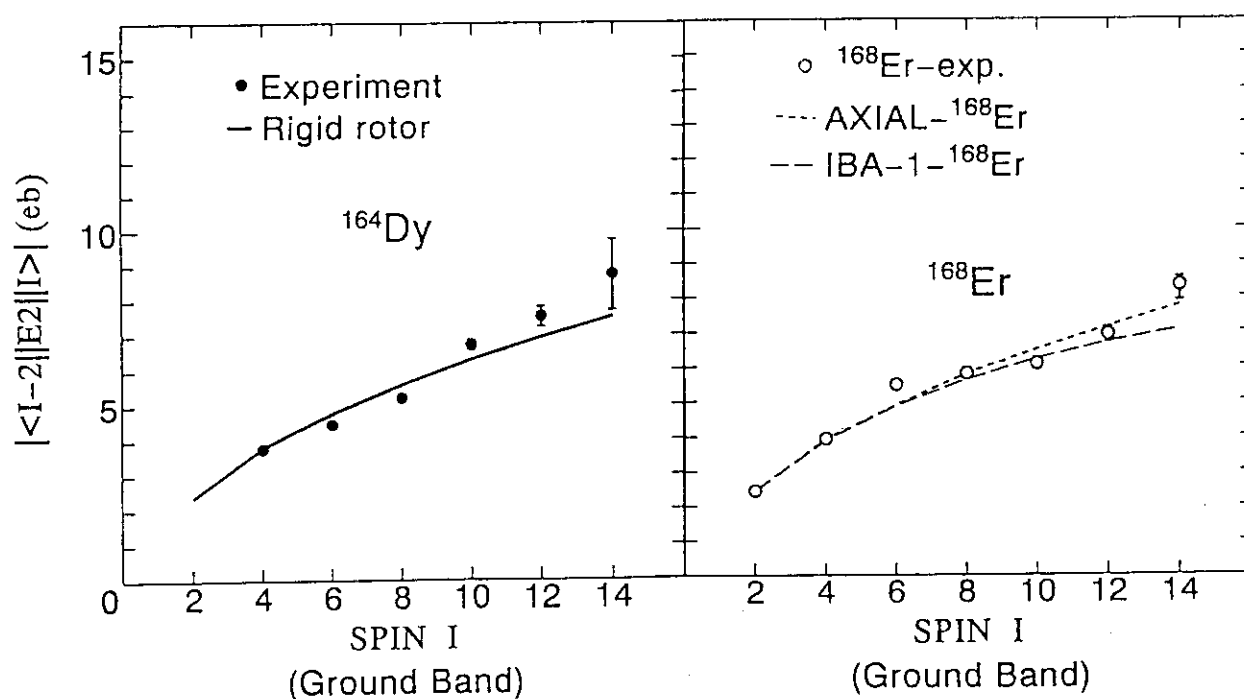


Fig.1 The obtained matrix elements of intraband transitions in the ground-band of ^{164}Dy (left). Those of ^{168}Er are taken from ref. 4 (right).

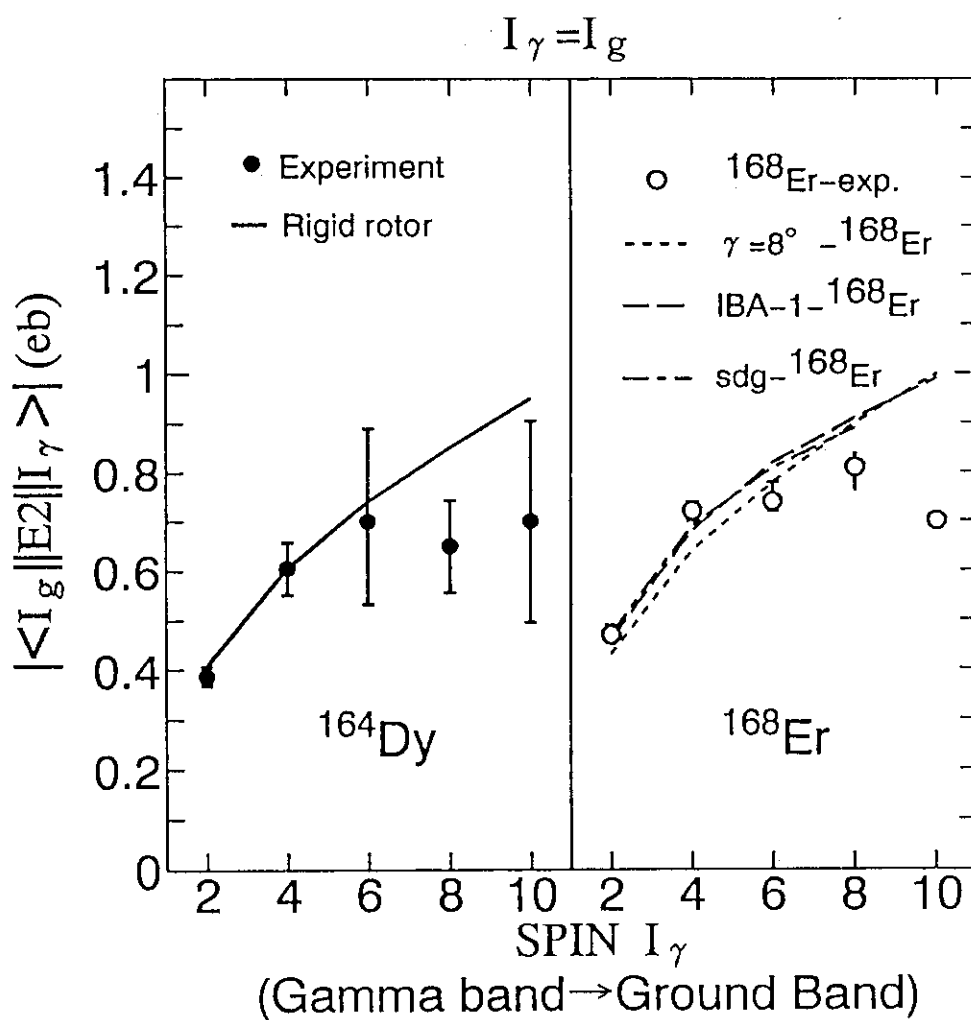


Fig. 2 The obtained matrix elements of $I_\gamma = I_g$ interband transitions between the gamma-band and the ground-band in ^{164}Dy (left). Those of ^{168}Er are taken from ref. 4 (right).

In fig. 3, we can see a drastic reduction of the matrix elements as increasing spin values. It means that the components of the higher-spin states in the gamma-band become much different from those in the ground-band. This phenomenon in ^{164}Dy is similar to that in ^{168}Er . Modern theoretical models do not reproduce this reduction. This is a problem left to be resolved.

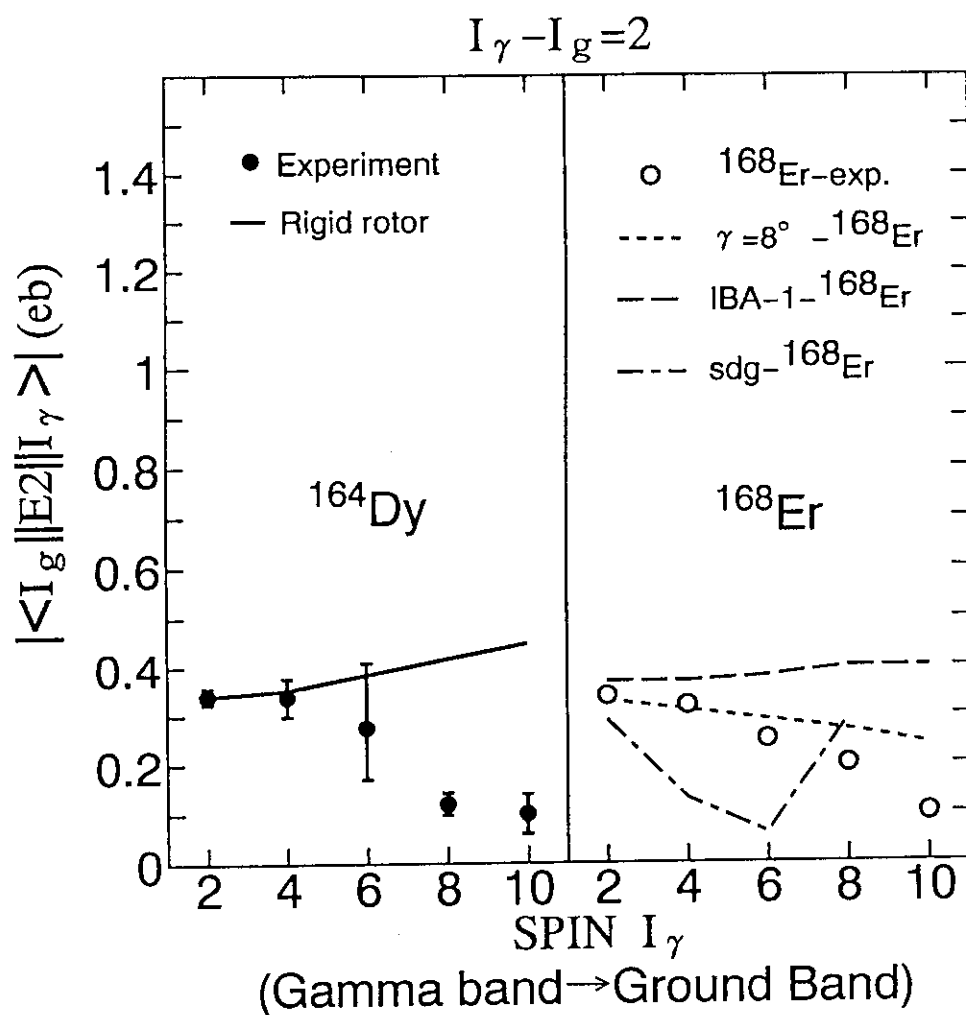


Fig. 3 The obtained matrix elements of $I_\gamma - I_g = 2$ interband transitions between the gamma-band and the ground-band in ^{164}Dy (left). Those of ^{168}Er are taken from ref. 4 (right).

References:

- 1) M. Oshima et al., RIKEN Accel. Prog. Report 1990 vol.24 (1991) p.21
- 2) Nuclear Data Sheets Vol.65 (1992) 388
- 3) A.Winther and J.DeBoer, Calif. Inst. Tech. Report
- 4) B.Kotlinski et al., Nucl. Phys. A517 (1990) 365; D. Cline, Annual Rev. Nucl. Part. Sci. vol.36 (1986) pp.683

5.4 Magnetic Substate Population of Excited $^{12}\text{C}(2^+)$ Nuclei Following Resonant $^{12}\text{C}+^{16}\text{O}$ Inelastic Scattering

Hiroshi FUJITA, Masayuki HIJIYA*, Takashi MUKAE*, Tsuyoshi SUGIMITSU*, Kotaro NAKAMOTO*, Shinichi MITSUOKA*, Kenji UTSUNOMIYA*, Takumi OKAMOTO*, Shunji NIIYA*, Makoto MATSUO*, Norihisa KATO*, Shunpei MORINOBU*, Yasuharu SUGIYAMA**, Yoshiaki TOMITA**, Hiroshi IKEZOE**, Kazumi IDENO** and Yoshimaro YAMANOUCHI**

Daiichi College of Pharmaceutical Sciences, *Department of Physics, Kyushu University, **Department of Physics, Japan Atomic Energy Research Institute

We have been studying some resonance-like structures in the singly excited $^{12}\text{C}(2^+)+^{16}\text{O}(\text{g.s.})$ and mutually excited $^{12}\text{C}(2^+)+^{16}\text{O}(3^-, 0_2^-)$ channels by measuring magnetic substate population of outgoing $^{12}\text{C}(2^+)$ nuclei following $^{12}\text{C}+^{16}\text{O}$ inelastic scattering. The magnetic substate population was extracted from a momentum spectrum broadened by γ -ray emission in flight¹⁾ as described in the preceding reports^{2,3)}.

The experiment was performed by using an ^{16}O beam from the JAERI tandem accelerator. Two ^{12}C targets were used; a $50\text{ }\mu\text{g}/\text{cm}^2$ thick one for observing angular distributions and a $25\text{ }\mu\text{g}/\text{cm}^2$ thick one for excitation function measurements. The outgoing ^{12}C particles were momentum analyzed by the heavy ion magnetic spectrograph "ENMA".

For the single excitation channel, the excitation functions were taken at $\theta_{\text{lab}} = 7^\circ$ ($\theta_{\text{cm}} \approx 165^\circ$) in the energy ranges from 64.3 MeV to 78.2 MeV and from 51.5 MeV to 52.7 MeV in steps of 0.4 MeV in the laboratory system. The angular distributions of the magnetic substate populations were measured in the laboratory angle

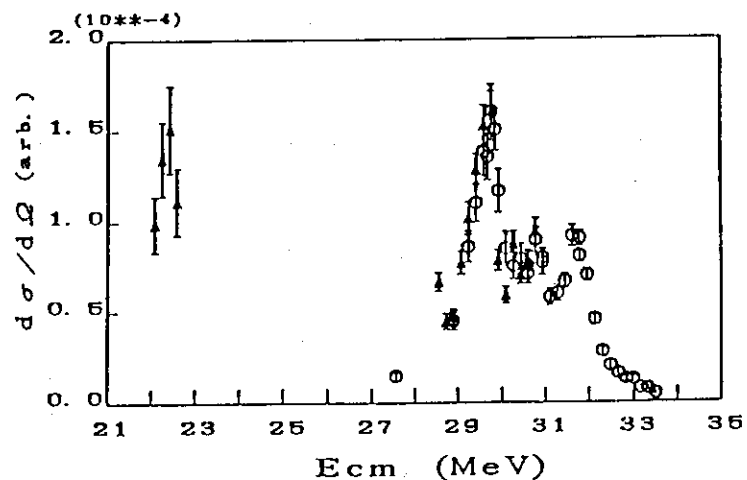


Fig.1 Excitation function for the single excitation channel of the $^{12}\text{C}(2^+)+^{16}\text{O}(0_g^+)$.

range from 4° to 17° in steps of 1° for the beam energies of 52.3, 69.4, 74.2 and 76.9 MeV ($E_{cm} = 22.4, 29.8, 31.8$ and 33.0 MeV, respectively). For the mutual excitation channel, the excitation functions were taken at $\theta_{lab} = 7^\circ$ from 71.4 MeV to 78.2 MeV at steps of 0.4 MeV. The angular distributions were measured in the laboratory angle range from 4° to 17° at steps of 1° for the beam energies of 70.2, 74.2 and 76.9 MeV.

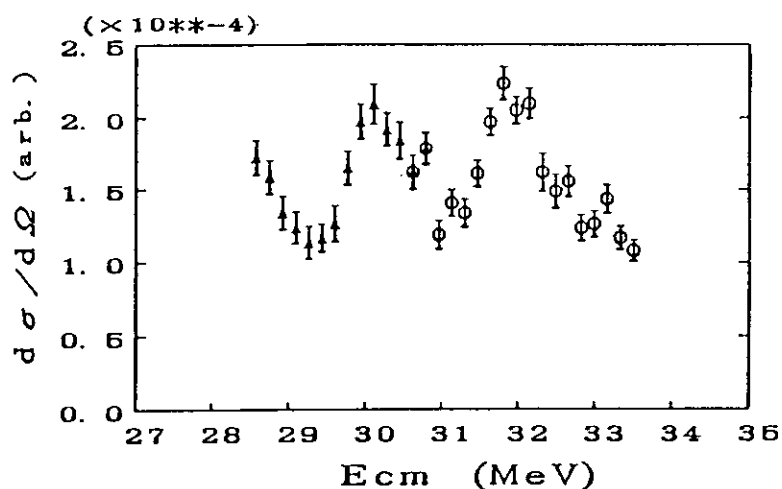


Fig.2 Excitation function for the mutual excitation channels of the $^{12}\text{C}(2^+) + ^{16}\text{O}(0_2^+)/^{16}\text{O}(3^-)$.

The preliminary results of the excitation functions are shown in Figs. 1 and 2. In the single excitation channel, three resonant structures seem to exist at $E_{cm} = 22.4, 29.8$ and 31.8 MeV. In the mutual excitation channel, two resonance-like structures are also seen at $E_{cm} = 30.1$ and 31.8 MeV.

As mentioned above, we tried to measure the magnetic substate population of the 2^+ state of ^{12}C by unfolding the spectrum broadened by γ -ray emission in flight. For this method, Sugiyama et al.¹³ have shown that the broadened line shape can be described only by the diagonal matrix elements of the nuclear density matrix by taking a z-axis pointed into the direction of the center of mass scattering angle of the outgoing particle in the reaction plane. The present analysis was also performed by taking this z-axis. In this coordinate system, the scattering amplitude for single excitation is given as

$$A_M(\theta) = (\sqrt{\pi}/ik) \sum_L \sqrt{2L+1} \exp(i\sigma_L) \sum_{L'} \langle LI-MM | L'0 \rangle \exp(i\sigma_{L'}) S_{L'-L} (-1)^{I+M} Y_{L-M}(\theta, 0) \quad (1)$$

and the cross section is given as

$$(d\sigma/d\Omega)_M = |A_M(\theta)|^2, \quad (2)$$

where L and L' denote the initial and final orbital angular momentum, respectively, and I and M the spin and the magnetic substate, respectively, of the outgoing particle. If only one partial wave contributes, therefore, we can estimate directly the total spin J of the system by comparing the angular

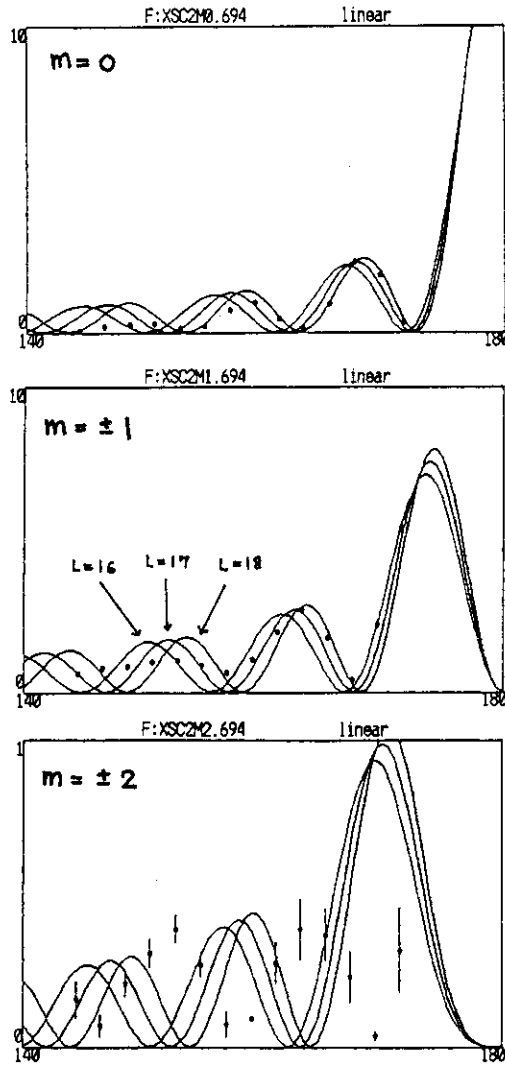


Fig.3 The angular distribution for the single excitation channel at $E_{lab} = 69.4$ MeV ($E_{cm} = 29.8$ MeV).

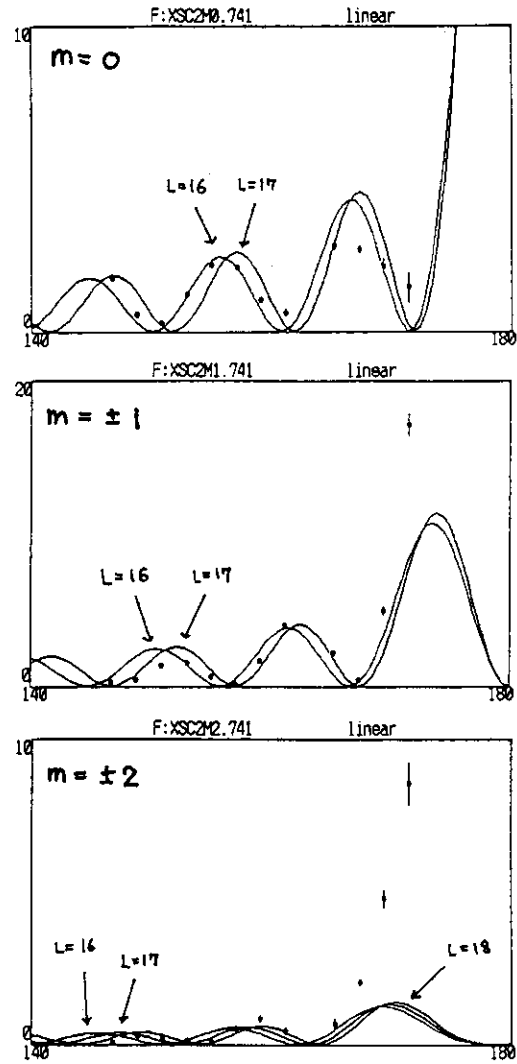


Fig.4 The same as Fig.3 at $E_{lab} = 74.2$ MeV ($E_{cm} = 31.8$ MeV).

distribution with $|Y_L^M(\theta)|^2$, because of $J = L$. Furthermore, we can obtain the information of the spin alignment by the following procedure. If it is assumed that only one S-matrix element $S_{L-1,L}$ (aligned coupling) is not zero, for $I = 2$ and $L \gg 1$, we obtain

$$\frac{(d\sigma/d\Omega)_0}{(Y_L^0)^2} : \frac{(d\sigma/d\Omega)_1}{(Y_L^1)^2} : \frac{(d\sigma/d\Omega)_2}{(Y_L^2)^2} \approx 3 : 4 : 1. \quad (3)$$

If non-aligned coupling (namely, only $S_{L,L}$ is not zero) is assumed to be

dominant, this ratio is 1 : 0 : 3.

For the single excitation channel, the analysis mentioned above was performed. Figs. 3 and 4 show the angular distributions for "on resonance" at $E_{cm} = 29.8$ and 31.8 MeV, respectively, with the calculations of $(Y_L^M(\theta))^2$. Both the angular distributions are well reproduced by the function $(Y_L^M(\theta))^2$ with $L = 17$ or 18 , and the ratio of eq.(3) obtained were 5 : 8 : 1.5 and 5 : 6 : 1 for $E_{cm} = 29.8$ and 31.8 MeV, respectively. This suggests that the total spin of these resonances may be $J = 17$ or 18 and the aligned coupling is dominant for both. Similar analyses were also performed for "on resonance" at $E_{cm} = 22.4$ MeV and for "off resonance" at $E_{cm} = 33.0$ MeV. For the resonance at $E_{cm} = 22.4$ MeV, the importance of the non-aligned coupling was suggested. Further analysis including the mutual excitation channel is now in progress.

References

- 1) Y. Sugiyama, Y. Tomita, H. Ikezoe and N. Shikazono, Z. Phys. A - Atoms and Nuclei **322** (1985) 579
- 2) H. Fujita et al., JAERI TANDEM, LINAC & V.D.G. Annual Report 1990, p.113
- 3) T. Mukae et al., JAERI TANDEM, LINAC & V.D.G. Annual Report 1991, p.154

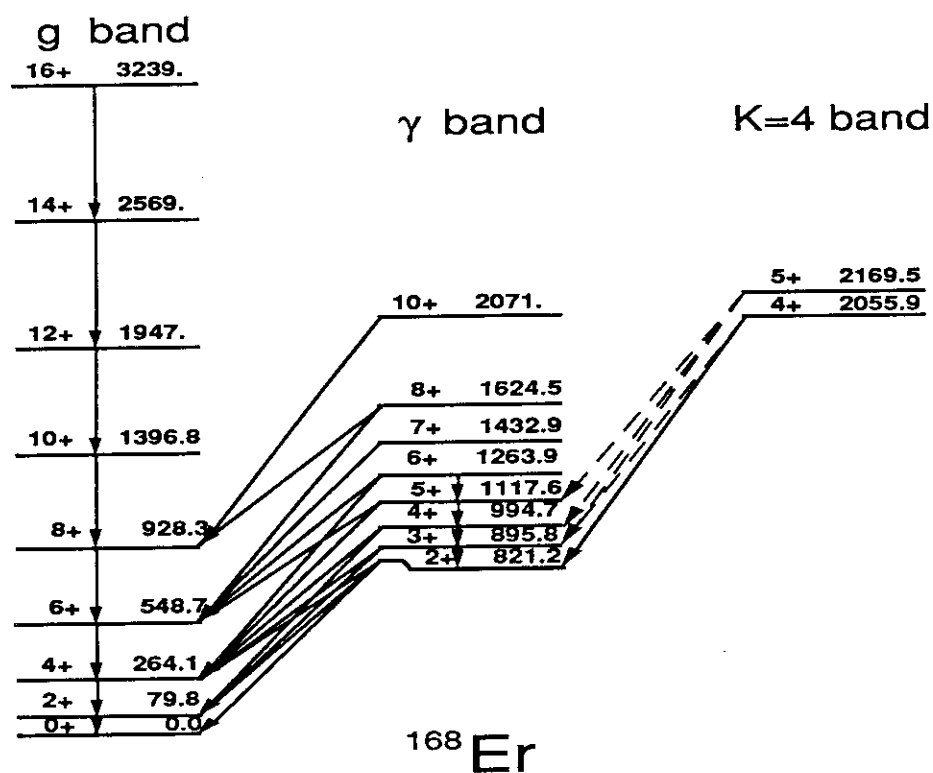
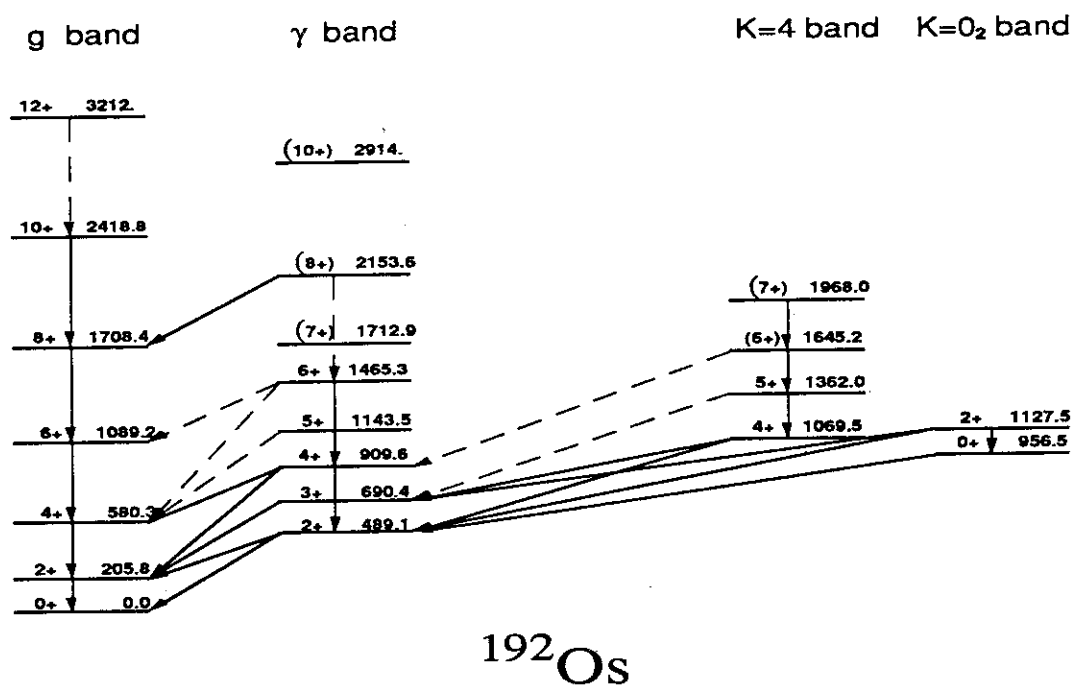
5.5 Double- γ Vibrational States in ^{168}Er and ^{192}Os

Masumi OSHIMA, Tsuneyasu MORIKAWA,* Hideshige KUSAKARI,** Nobuhiko KOBAYASHI,** Masayuki TAKI,** Masahiko SUGAWARA,*** Yu H. ZHANG,* Alain FERRAGUT,* Shin-ichi ICHIKAWA,**** Nobuo SHINOHARA,**** Yuichiro NAGAME,***** Michihiro SHIBATA, Yasuyuki GONO,***** and Takashi INAMURA*

Department of Physics, JAERI, *RIKEN, **Faculty of Education, Chiba University, ***Chiba Institute of Technology, ****Department of Chemistry, *****Department of Radioisotopes, JAERI, *****Department of Physics, Kyushu University

Multi-phonon vibrational excitations are known to be well established in near-spherical region. In deformed or transitional region, however, even the two-phonon state has not been identified definitely. Their existence and collectivity is one of the central problem for elucidating the collective excitation of nuclei.¹⁻⁵⁾ The candidates for the double- γ state in ^{168}Er and ^{192}Os have been reported⁶⁻⁸⁾ but the $B(E2)$ values from these states to one-phonon vibrational state have not been measured definitely. Since the $B(E2)$ value from the two phonon to the one phonon state is a direct measure of collectivity, it is important to derive the $B(E2)$ value for identifying the two phonon state and for discussing the nuclear collectivity and anharmonicity of collective vibration. Because of this we made a Coulomb-excitation experiment for these nuclei exclusively optimized for the observation of the known transitions from the candidates of double- γ states to the single- γ state.

The ^{168}Er and ^{192}Os nuclei were multiply Coulomb-excited with beams of 295-MeV ^{74}Ge and 235-MeV ^{58}Ni , respectively, which were obtained from the tandem accelerator. The target was a self-supporting metallic foil of 1.8 mg/cm² for ^{168}Er and 1.3 mg/cm² for ^{192}Os (95% isotopically enriched). A detailed experimental method can be seen in Ref. 9. Figure 1 shows a partial level scheme of ^{168}Er derived from the present experiment. We observed members of the g band up to 16^+ and of the γ band

Fig. 1. A partial level scheme of ^{168}Er .Fig. 2. A partial level scheme of ^{192}Os .

up to 10^+ ; the 14_g^+ , 16_g^+ and 10_γ^+ states are newly assigned. Most importantly, the 1234-keV transition from the candidate of double- γ vibrational state to the one-phonon γ -vibrational state is observed for the first time in Coulomb excitation. We derived the $B(E2)$ value for the $2_2^+ \rightarrow 4_3^+$ transition as $0.070 \pm 0.016 \text{ e}^2\text{b}^2$. The value agrees with the previously reported one of Ref. [7] within the experimental accuracy.

The ^{192}Os nucleus lies in the transitional region from axially symmetric to γ soft nuclei and the one-phonon γ vibrational state is observed at relatively low excitation energy as shown in Fig. 2. Moreover, candidates for the two phonon states with $K=4$ and 0 have been assigned.

The $E\lambda$ matrix elements have been derived through the analysis based on Coulomb excitation code GOSIA.¹⁰⁾ The observed $B(E2; 2_2 \rightarrow 4_3)$ value for ^{168}Er reveals relatively large collectivity (5.9 single-particle unit) for the 4_3 state. Thus this state is demonstrated to have a dominant double- γ vibrational character. In Table 1 we present the experimental result. Here we used the ratios, $E(4^+)/E(2^+)$ and $B(E2; 2_2 \rightarrow 4_3)/B(E2; 0_g \rightarrow 2_2)$, to compare with theoretical calculations. The values of $E(2^+)$ and $B(E2; 0_g \rightarrow 2_2)$ are 821 keV and $0.132 \pm 0.005 \text{ e}^2\text{b}^2$, respectively. Theoretical $B(E2; 2_2 \rightarrow 4_3)/B(E2; 0_g \rightarrow 2_2)$ ratios are 0.16, 0.40, 0.50, 1.44, and 0.68 based on the Quasiparticle-Phonon Nuclear Model (QPNM),¹⁾ the Multi-Phonon Method (MPM),²⁾ the Dynamic Deformation Model (DDM),³⁾ the extended Interacting Boson Model with s, d and g bosons (sdg-IBM),⁴⁾ and the Selfconsistent Collective Coordinate Method (SCCM),⁵⁾

Table 1. Summary of double- γ state in ^{168}Er and ^{192}Os

Nucleus	K	I	$\frac{E(I)}{E(2^+)}$	$\frac{B(E2; 2_\gamma \rightarrow 4_\gamma)}{B(E2; 0_g \rightarrow 2_\gamma)}$	$\frac{B(E2; 0_\gamma \rightarrow 2_\gamma)}{B(E2; 0_g \rightarrow 2_\gamma)}$	reference
^{168}Er	4	4	2.503	0.53 ± 0.12	-	present
			"	0.38 ± 0.20	-	Ref. [6]
^{192}Os	4	4	2.19	0.54 ± 0.06	-	present
	0_2	0	1.96	-	0.40(4)	present
Harmonic limit			2.00	1.00	1.00	

respectively. The MPM, sdg-IBM and SCCM calculations seem to be consistent with the present result.

The $B(E2)$ values of ^{192}Os derived from the present experiment is also shown in Table 1. The 4_3^+ and 0_2^+ states are located at approximately twice the energy of the 2_γ state and they are candidates for the double- γ states. The $B(E2; 2_2 \rightarrow 4_3)$ value shows relatively large collectivity (9.2 single-particle unit) and the $B(E2; 2_2 \rightarrow 4_3) / B(E2; 0_1 \rightarrow 2_2)$ ratio becomes 0.54 . These facts indicate that the 4_3 state has a dominant double- γ vibrational character. Recently, results for $^{188,190}\text{Os}$ have been reported in Refs. [11,12] and the situation is similar in these isotopes.

The $K=0_2$ band has been also identified in ^{192}Os (Ref. [8]) and the $B(E2)$ values for some of the transitions decaying from the band head are determined as shown in Table 1. We compare the present result with the SCCM calculation by Matsuo et al.⁵⁾ (Results of sd-IBM analysis can be found elsewhere.¹³⁾) The energies of the 0_2^+ and 4_3^+ states indicate small anharmonicity ($E(4_3^+) / E(2_2^+) \approx E(0_2^+) / E(2_2^+) \approx 2$), while SCCM results show large anharmonicity. Nevertheless, the calculation and the experiment reveal similar amount of reduction of collectivity in $B(E2)$. Thus it is hard to state that the experiment and SCCM calculation are consistent with each other. Although the discrepancy is not clear, γ softness of these nuclei may need to be taken into account: for these γ soft nuclei, SCCM calculation based on the expansion around the axially symmetric shape may not be very accurate. Actually, deformation extracted from $B(E2; 0_1 \rightarrow 2_2)$ is small.

References

- 1) V.G.Soloviev and N.Yu.Shirihova, Z. Phys. A301, 263 (1981); and private communication.
- 2) M.K.Jammari and R.Piepenbring, Nucl. Phys. A487, 77 (1988).
- 3) K. Kumar, Nuclear Models and the Search for Unity in Nuclear Physics (Universitetsforlaget, Bergen, Norway, 1984).
- 4) N.Yoshinaga, Y.Akiyama, and A.Arima, Phys. Rev. Lett. 56, 1116 (1986).
- 5) M.Matsuo and K.Matsuyanagi, Prog. Theor. Phys. 76, 93 (1986); *ibid* 78, 591 (1987).
- 6) W.F. Davidson et al., J. of Phys. G7, 455, 843 (1981).

- 7) H.G.Börner et al., Phys. Rev. Lett. 66, 691 (1991).
- 8) V.S. Shirley, Nucl. Data Sheets 64, 205 (1991).
- 9) M.Oshima et al., Proc. of Int. Sympo. on Rapidly Rotating Nuclei in Tokyo
(Oct.26-30, 1993); Nucl. Phys. A (1993) to be published.
- 10) D.Cline, Ann. Rev. Nucl. Part. Sci. 36, 681 (1986); and references therein.
- 11) B. Sinh, Nucl. Data Sheets 61, 243 (1990).
- 12) B. Sinh, Nucl. Data Sheets 59,133 (1990).
- 13) M. Sugita, Nucl. Phys. A (1993) to be published.

5.6 In-beam Study of ^{109}Sb

Tetsuro ISHII, Akiyasu MAKISHIMA^{*}, Michihiro SHIBATA,
Masao OGAWA^{**} and Mitsuhiro ISHII

Department of Physics, JAERI, ^{*}Center for Radioisotope Science,
National Defense Medical College, ^{**}Department of Energy Science,
Tokyo Institute of Technology

High-spin states in ^{109}Sb were studied using the reaction $^{54}\text{Fe}(^{58}\text{Ni}, 3p)^{109}\text{Sb}$ at a bombarding energy of 225 MeV. Experiments included the measurements of γ - γ coincidences, γ -ray angular distribution and γ -ray linear polarization. All the experiments were performed by using the Si box¹⁾. The present study revealed a level scheme shown in Fig. 1. The excited levels were divided into bands (I) to (V).

The proton orbits $\pi d_{5/2}$, $\pi g_{7/2}$ and $\pi h_{11/2}$ are involved in low excitation of ^{109}Sb and the first has the lowest excitation energy among them. The level structure in band (I) bears a close resemblance to that in ^{108}Sn . Band (I) is thus considered to arise from a $\pi d_{5/2}$ proton coupling with the core ^{108}Sn in the 0^+ , 2^+ , \dots states. Band (III) shows a similar energy spectrum as band (I) but comprises negative-parity states. Band (III) may be interpreted as the $\pi h_{11/2}$ band. Band (II) is based on the $\pi g_{7/2}$ orbit. The $7/2^+$ state in ^{109}Sb appears at a rather high excitation energy of 832 keV. As a result admixture of the configuration $\pi d_{5/2} \otimes (^{108}\text{Sn})_4^+$ may take place in the $9/2^+$ and $11/2^+$ states in band (II).

Two collective bands appear in ^{109}Sb ; band (IV) starts from the $17/2^+$ state at 2651 keV and band (V) from the $23/2^-$ state at 4487 keV. Some $\Delta I=1$ transitions in these bands were confirmed to possess the mixing ratios $\delta(E2/M1) > 0$. This indicates that core excitation takes place there and generates the $(\pi g_{9/2})^{-1}$ proton hole; this hole causes a prolate deformation and gives a positive E2 matrix element. Band (IV) may be ascribed to the protons rotationally aligned to the rotor with a hole:

$(\pi d_{5/2})^2_{4^+} \otimes [(\pi g_{9/2})^{-1} \cdot ^{108}\text{Sn}]$. In a similar way band (V) may be interpreted as $(\pi d_{5/2} \cdot \pi h_{11/2})_{7^-} \otimes [(\pi g_{9/2})^{-1} \cdot ^{108}\text{Sn}]$.

The $B(E2)/B(M1)$ ratios for the intraband E2 and M1 transitions in band (IV) were measured to be 0.08(3) for $I=21/2^+$ and 0.014(3) for $I=27/2^+$ in band (IV). The Q_0 moment can be evaluated from this ratio using the following expression:

$$Q_0 = \left[\frac{8(I-1)(2I-1)K^2}{5(I-1-K)(I-1+K)} \frac{B(E2; I-I-2)}{B(M1; I-I-1)} \right]^{1/2} (g_K - g_R),$$

where g_K and g_R are the g -factors for an odd nucleon/hole and for the rotor, respectively, and $g_K = g_R + (g_R - g_K) \frac{\Omega^2}{K(K+1)}$. If $g_R = 0.5$, $g_\Omega = g[(\pi g_{9/2})^{-1}] = 1.50$ and $K = \Omega = 9/2$, then $g_K = 1.32$ is obtained. For the complete alignment in band (IV), the replacement of I to $I-4$ in the above expression gives a good approximation of the branching ratio. Then Q_0 is evaluated to be 3.1–3.5 barns, which is equivalent to $\beta = 0.23$ – 0.26 . Similar Q_0 values are also obtained for band (V). This fact indicates that the core excitation in ^{109}Sb induces enhancement of the nuclear deformation.

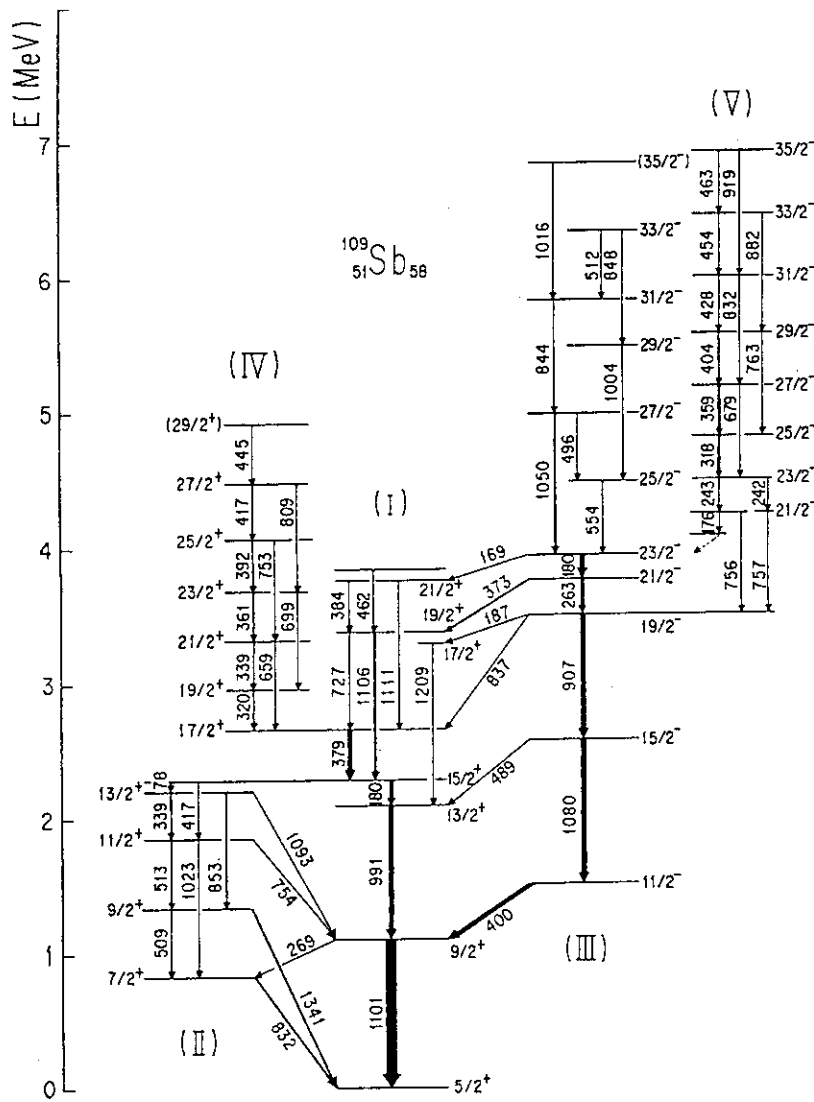


Fig.1

A level scheme of ^{109}Sb

References

- 1) M. Ishii, A. Makishima, M. Hoshi, and T. Ishii: in *Nuclei off the line of stability*, R.A. Meyer and D. S. Brenner(eds.), p350, Washington D.C., American chemical society 1986.

5.7 Level Position Correlations and Partial Radiative Widths for the U-238 Neutron Resonances¹⁾

Kazumi IDENO

Department of Physics, JAERI

Neutron resonance data have been one of rich fields to study chaotic motion in nuclei²⁾. For example, level statistics for the ^{238}U data were shown to be well predicted by a GOE³⁾. However, there may be regularities which are not sensitively reflected in the level statistics. There observed cases where a dominant periodic level sequence is merged in the complex spectrum⁴⁾. For the purpose of clarifying the physical origin of such structure, we have analyzed the ^{238}U data where a dominant correlation period of 14.4 eV is observed in the level distribution⁵⁾. We searched for the positions of 14.4-eV periodic level sequences and compared this result with the correlation analysis of partial radiative widths by Wasson et al.⁶⁾. We obtained the following results:

a) As Fig. 1 shows, all the observed s-wave levels below 600 eV are located with a good accuracy within the two 14.4-eV periodic level sequences, one starting from a point of zero energy and the other from a point shifted by a half of 14.4 eV.

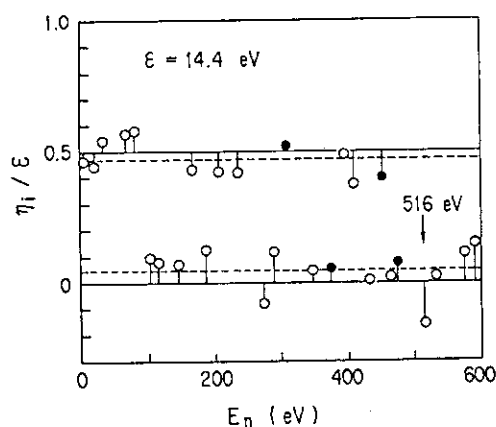


Fig. 1 Deviation of ^{238}U s-wave resonance energy E_i from a near point of integral multiple of $\epsilon = 14.4$ eV.

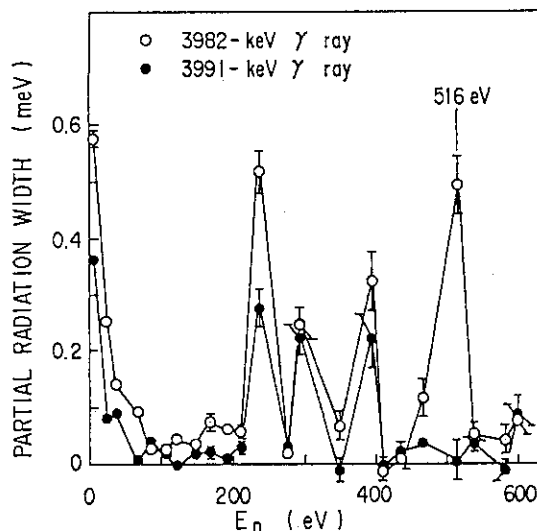
Here the deviations η_i are normalized to ϵ . Open and full points denote the levels for which partial radiative widths were measured or not. The dashed lines represent the average values of η_i/ϵ in the upper and lower bands.

b) Similar band structure is found for the levels between 600 and 1200 eV, but in this case the period is 3/4 times the previous one.

c) Wasson et al. showed from the measurements of partial radiative widths that the

transition intensities from the capturing states to two low-lying states at 815 and 823 keV, which were assigned to be members of the band built on the octupole vibrational state⁷⁾, had a strong correlation with each other and varied from resonance to resonance in a similar manner except at the 516 eV resonance. The correlated behavior for the two γ -ray transitions can be seen in Fig. 2. It is interesting to note that this 516 eV resonance

Fig. 2 Distribution of partial radiative widths from the capturing states of $^{238}\text{U} + n$ to the two low-lying states of 815 and 823 keV⁶⁾.



has the largest deviation from the average value of η_i/ϵ in the lower band in Fig. 1.

It seems that in the periodic structure an average value of η_i , which is called a *shift*, plays an important role as well as its period ϵ .

References

- 1) K. Ideno: Contributions to the 21st INS Int. Symp. on Rapidly Rotating Nuclei 1992 (INS, Univ. of Tokyo, 1992).
- 2) H.A. Weidenmüller: Nucl. Phys. **A520** (1990) 509c.
- 3) F. Rahn et al.: Phys. Rev. **C6** (1972) 1854.
- 4) K. Ideno: Nuclear Data for Science and Technology (1988, Mito) 783.
- 5) K. Ideno: J. Phys. Soc. Jpn. **37** (1974) 581.
- 6) O.A. Wasson et al.: Phys. Rev. **C4** (1971) 900.
- 7) H.G. Börner et al.: Z. Physik **A286** (1978) 31.

5.8 Measurements of Charged Particle Multiplicities in the Fission Process of ^{178}W

Hiroshi IKEZOE, Yuichiro NAGAME, Tsutomu OHTSUKI,
Ichiro NISHINAKA, Yasuharu SUGIYAMA, Yoshiaki TOMITA,
Kazumi IDENO
Department of Physics, JAERI

Recently we have reported the measurements of the pre-scission charged particles emitted in the fission process of the heavy compound nuclei, whose fissilities χ are 0.7 – 0.85, produced in the $^{16}\text{O} + ^{197}\text{Au}$, $^{19}\text{F} + ^{181}\text{Ta}$, ^{197}Au and ^{208}Pb , and $^{28}\text{Si} + ^{197}\text{Au}$ and ^{208}Pb reactions. It was found that a transient time, during which the fission width increases from zero to an equilibrium value at the saddle point, was less than $1 \times 10^{-20}\text{sec.}^1)$. This time scale is shorter than $3.5 \pm 1.5 \times 10^{-20}\text{sec.}^2)$, which has been obtained from the pre-scission neutron measurements. We concluded in Ref.[1] that the cause of the disagreement may be due to extra neutrons emitted during the descent from saddle to scission, while charged particles are mainly emitted in the region before saddle, not from the saddle-to-scission region.

In order to study this problem, we measured light charged particles emitted from lighter compound nucleus ($\chi \approx 0.6$) than the previously studied nuclei. Since the saddle shape of such lighter nucleus is close to its scission shape, it is expected that the saddle-to-scission times in the fission process of lighter nuclei are short and a minor part of the total fission time scale. In this situation we can directly compare the results obtained from the pre-scission neutron data with those from the charged particle data and then get information about the transient time in the fission process.

The compound nucleus ^{178}W ($\chi = 0.637$) was produced in the $^{19}\text{F} + ^{159}\text{Tb}$ reaction using ^{19}F beams from the JAERI tandem accelerator. In order to separate the fission events from those originated from the other reaction processes, both fission fragments were simultaneously detected by using a solid state detector and a position-sensitive avalanche counter. Charged particles (proton and α particles) were measured in coincidence with both fission fragments at the backward angles ($\theta = 110, 145$ deg.) and the out-of-plane angles ($\varphi = 0, 25, 50, 75$ deg.). Measured energy spectra of proton and α particles were decomposed into the pre-scission and the post-scission components as described in Ref.[1]. Fig.1 shows the pre-scission multiplicities of proton and α particles as a function of the excitation energy U of the compound nucleus ^{178}W . These data are compared with the calculated results using the statistical model. The obtained multiplicities increase as U more rapidly than those of the statistical model predictions. This energy dependence of the pre-scission multiplicities of proton and α particles is drastically different from our

previous results, but qualitatively similar to those of Ref.[3], where the multiplicities of proton and α particles are enhanced at high excitation energy region. The present results are rather consistent with the pre-scission neutron data observed in the fission process of low fissile nuclei²⁾. The detailed analysis taking into account the transient time in the fission process is still underway.

References

- 1) H. Ikezoe, et al., Phys. Rev. C46 (1992) 1992.
- 2) D.J. Hinde, et al., Nucl. Phys. A452 (1986) 550.
- 3) P. Lestone, et al., Phys. Rev. Lett. 67 (1991) 1078.

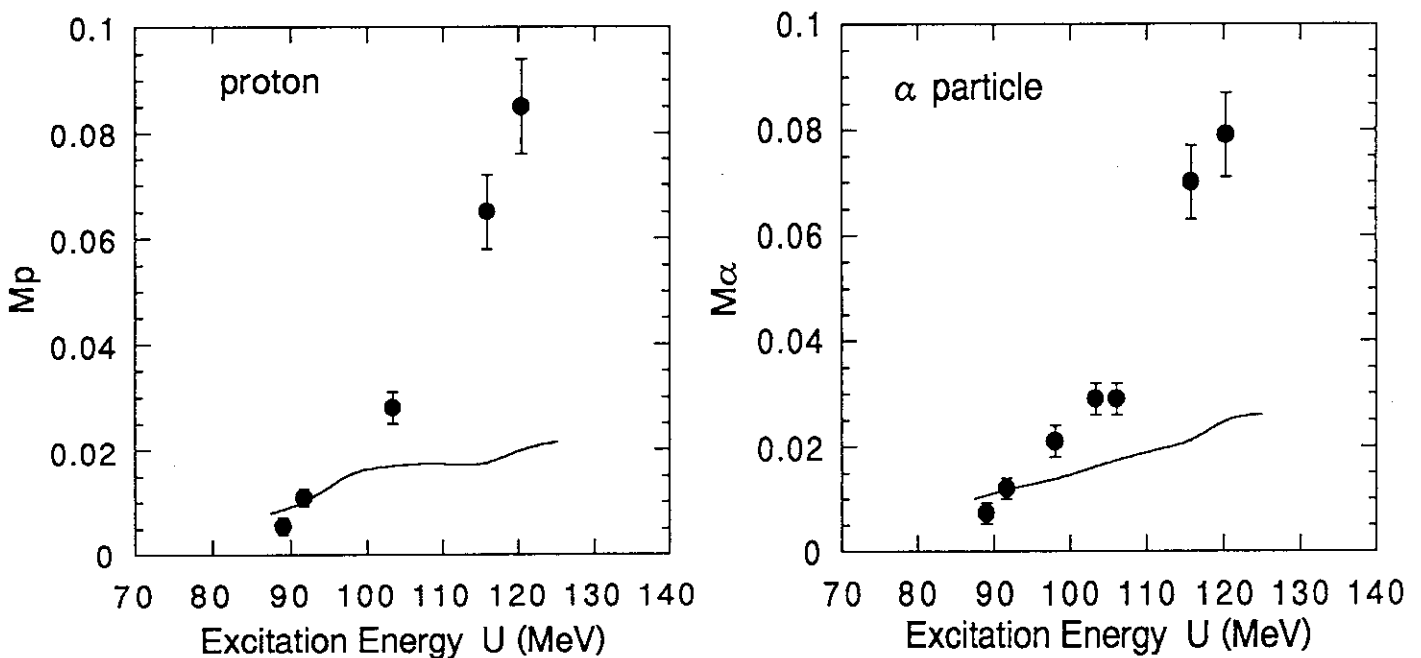


Fig.1 Pre-scission proton and α particle multiplicities as a function of the excitation energy of the compound nucleus ^{178}W . The calculated results are shown as lines.

5.9 Light Charged Particle Identification with CsI(Tl) Scintillators for Heavy Ion and Fission Reactions

Tsutomu OHTSUKI, Masumi SUGAWARA, Jirota KASAGI,
Hiroshi IKEZOE*, Yuishiro NAGAME**,
Kazuaki TSUKADA***, Masaaki MAGARA***
Ichiro NISHINAKA****

Laboratory of Nuclear Science, Tohoku University

*Department of Physics, **Department of Radioisotopes,

Department of Chemistry, JAERI, *Department of Chemistry,
Tokyo Metropolitan University

The detection of light charged particles provides a precious tool to study different processes involved in heavy ion reactions and fission. Recently, the multiplicity and energy of the light charged particle to be detected have lead to a greater number of detectors and to larger thickness of those detectors. As a consequence standard solid state Si telescopes have been gradually replaced by scintillators such as CsI(Tl), BaF₂, NaI(Tl) and BGO.¹⁾⁻³⁾

In order to investigate, a correlation between the light charged particle emission and heavy ion collisions or fission, cristal scintillator CsI(Tl) with two light decay components was tested.

The scintillation decay shape of CsI(Tl) crystal is a combination of exponentials of different time constants:

$$L(t) = L_s \exp(-t/\tau_s) + L_f \exp(-t/\tau_f) \quad (1)$$

where $L(t)$ is the light pulse amplitude at time t , L_s and L_f are the each light amplitudes, τ_s and τ_f are the constant time decays for the slow and fast components, respectively.

Two CsI(Tl) scintillators (1 inch ϕ x 1 inch height) covered with Al-mylar foil were situated at $\pm 20^\circ$ with respect to the beam direction. ²⁷Al and ²⁰⁹Bi of about 100 $\mu\text{g}/\text{cm}^2$ and 300 $\mu\text{g}/\text{cm}^2$ thickness were used for the target, respectively, and a beam of 145 MeV ¹⁶O from the JAERI tandem accelerator was provided for the bombardment.

The signal produced by a particle going through the scintillator was obtained from the anode output of the photomultiplier whereas the output of the last dynode was used for timing to trigger the data acquisition. The anode signal was gated for the fast component(S_f :main component) and the slow component(S_s : delayed component). Two QDCs (LeCroy 2249W) were used for the partial charge integration of S_f and S_s .

Fig.1 displays a bidimensional plot measured with CsI(Tl) scintillator for the reaction $^{16}\text{O}+^{27}\text{Al}$. A good mass identification for p, d, t, ^3He , ^4He , and Li group particles can be appreciated. The light particle events for the $^{16}\text{O}+^{209}\text{Bi}$ were rather scarce. The energy of each emitted particles was estimated by detecting energy losses in $30\text{ }\mu\text{m}$ ΔE Si-surface barrier detector placed in front of the CsI(Tl). However, energy resolution was worse compared with the standard solid state Si telescopes. Further improvement is needed to achieve higher energy resolution for detecting the charged particles.

References

- 1)E. Valtonen, J. Peltonen and J.J. Torsti, Nucl. Instr. Meth. **A286**, (1990)169.
- 2)F. Benrachi, B. Chambon, B. Cheynis, D. Drain, C. Pastor, D. Seghier, K. Zaid, A. Giorni, D. Heuer, A. Lleres, C. Morand, P. Stassi, and J.B. Viano, Nucl. Instr. Meth. **A281**, (1989)137.
- 3)G. Lanzano, A. Pagano, S. Urso, E.De Filippo, B. Berthier, J.L. Charvet, R. Dayras, R. Legrain, R. Lucas, C. Mazur, E. Pollacco, C. Beck, B. Djerroud and B. Heusch, Nucl. Instr. Meth. **A312**, (1992)515.

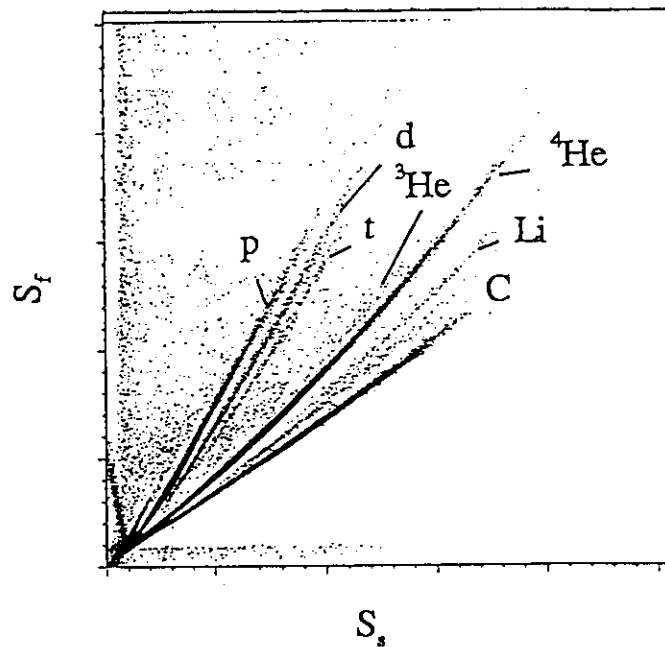


Fig.1 Bidimensional fast vs slow component spectrum for the light charged particles measured in the $^{16}\text{O}+^{27}\text{Al}$ reaction at bombarding energy 145 MeV and at detection angle of 20° .

VI. PUBLICATION IN JOURNALS AND PROCEEDINGS

Publication in Journals and Proceedings

1. Baba, M., Ito, N., Matsuyama, S. and Hirakawa, N.
 A High Efficiency Charged-Particle Spectrometer Using Gridded Ionization Chamber for Fast-Neutron Induced Reactions
 Proc. Int. Conf. on Nuclear Data for Science and Technology (May 1991 Jülich)
 S.M. Qaim(ed.), Springer-Verlag (1992) p.477
2. Buchinger, F., Schuessler, H.A., Benck, E.C., Iimura, H., Li, Y.F., Bingham, C. and Carter, H.K.
 Isotope Shift Measurements on the Neutron-Deficient Thallium Isotopes Hyperfine Interactions 75 (1992) 367
3. Duh, M.-C., Baba, H., Takahashi, N., Yokoyama, A., Saito, T., Baba, S. and Hata, K.
 Charge and Mass Characteristics of the Fragments in the Fission of Uranium Isotopes Induced by ^{12}C Ions
 Nucl. Phys. A550 (1992) 281
4. Haruna, K., Maeta, H., Ohashi, K. and Koike, T.
 Thermal Expansion Coefficient of Synthetic Diamond Single Crystal at Low Temperatures
 Jpn. J. Appl. Phys. 31 (1992) 2527
5. Haruna, K. and Maeta, H.
 Thermal Expansion of Synthetic Diamond Single Crystal at Low Temperatures
 Diamond and Related Materials. 2 (1993) 859
6. Ikezoe, H., Shikazono, N., Nagame, Y., Ohtsuki, T., Sugiyama, Y., Tomita, Y., Ideno, K., Nishinaka, I., Qi, B.J., Kim, H.J. and Iwamoto, A.
 Charged Particle Multiplicities in Heavy-ion Induced Fission
 1st Joint Italian-Japanese Meeting within the INFN-RIKEN Agreement
 "Perspective in Heavy Ion Physics", Catania, 29 September - 3 October 1992, p.119
7. Imai, M., Sataka, M., Naramoto, H., Yamazaki, Y., Komaki, K., Kawatsura, K. and Kanai, Y.
 Dynamical Behaviour of Angular Momentum Distributions of Autoionizing $1s^2 2p 9l$ States of S^{12+} Ions Excited through Carbon Foils
 Nucl. Instr. and Meth. B67 (1992) 142

8. Ishii, T., Makishima, A., Nakajima, M., Ogawa, M., Ishii, M., Saito, Y. and Garnsomsart, S.
In-beam Study of ^{105}In and ^{103}In
Z. Phys. A343 (1992) 261
9. Ishii, T., Shibata, M. and Takeuchi, S.
Construction of the JAERI Tandem Booster
Nucl. Instr. and Meth. A328 (1993) 231
10. Ito, N., Baba, M., Matsuyama, S., Hirakawa, N., Chiba, S., Fukahori, T., Mizumoto, M. and Hasegawa, K.
Measurement of Double-differential α -Particle Production Cross Sections of Fe and Ni using Gridded Ionization Chamber
Proc. 1992 Symposium on Nuclear Data; JAERI-M 93-046 (JAERI 1993) p.334
11. Ideno, K.
Level Position Correlations and Partial Radiative Widths for the U-238 Neutron Resonances
21st INS Int. Symp. on Rapidly Rotating Nuclei 1992 (Tokyo, 1992) Abstract p.91
12. Kashimoto, H., Watanabe, Y., Koyama, Y., Shinohara, H. and Chiba, S.
Study of ^{12}C Breakup Processes and Carbon Kerma Factors
Proceedings of the 1992 Symposium on Nuclear Data, Nov. 26-27, 1992, JAERI, Tokai JAERI-M 93-046 (1993) pp.287
13. Kazumata, Y. and Okayasu, S.
Radiation Effects of High Tc Superconducting Materials
The 5th US/Japan Workshop on High Tc Superconductors (Tsukuba, November 9-10)
14. Kikuchi, S. and Sugiyama, Y.
Calibration for the Beam Energy and the Terminal Voltage of the JAERI Tandem Accelerator
JAERI-memo 05-077 (1993)
15. Kumakura, H., Kitaguchi, H., Togano, K., Maeda, H., Shimoyama, J., Okayasu, S. and Kazumata, Y.
Flux Pinning Characteristics in 180MeV Cu^{11+} -Irradiated $\text{Bi}_2\text{Sr}_2\text{CaCu}_2\text{O}_x$
Jpn. J. Appl. Phys. 31 (1992) L1408
16. Kusakari, H., Oshima, M., Ichikawa, S., Iimura, H., Inamura, T., Hashizume, A., Sugawara, M. and Matsuzaki, M.
Electromagnetic Transition Probabilities in the Natural-Parity Rotational Band of $^{155,157}\text{Gd}$
Phys. Rev. C46 (1992) 1257

17. Maeta, H. and Haruna, K.
X-ray Diffraction Studies of Self-ion Irradiated Synthetic Single
Crystal Diamond
Nuclear Instruments and Methods in Physics Research, in print
18. Makishima, A., Ishii, T., Ogawa, M. and Ishii, M.
IBM-2 Parameters for Proton-rich Rare-earth Nuclei
J. Phys. Soc. Jpn 61 (1992) 3409
19. Matsumoto, N., Bang, Lu., Maeta, H., Jakubonovics, J.P., Haruna, K.
and Ono, F.
Effect of Ion Beam Irradiation in Amorphous Ferromagnetic Alloys
Nuclear Instruments and Methods in Physics Research, in print
20. Morikawa, T., Oshima, M., Sekine, T., Hatsukawa, Y., Ichikawa, S.,
Iimura, H., Osa, A., Shibata, M. and Taniguchi, A.
Lifetime Measurement of the First 2^+ State in $^{122,124,126}\text{Ba}$
Phys. Rev. C46 (1992) R6
21. Murakami, T., Gono, Y., Ferragut, A., Zhang, Y.H., Morita, K.,
Yoshida, A., Ogawa, M., Nakajima, M., Min, B.J., Kumagai, H., Oshima,
M., Morikawa, T., Sugawara, M. and Kusakari, H.
High-spin Isomeric State in ^{144}Pm
J. Phys. Soc. Jpn 60 (1991) 1424
22. Nagame, Y., Ikezoe, H. and Ohtsuki, T.
Symmetric Mass Division Process in Nuclei with Mass Numbers around
 $A_{\text{CN}}=100$
Phys. Rev. C47 (1993) 1586
23. Nakae, T., Mitamura, T., Terasawa, M., Uchida, H., Koterazawa, K.,
Iwasaki, H., Sataka, M., Imai, M., Maeta, H., et al.
Channeling Study of Radiation Effect in Single Crystal of 304
Austentic Stainless Steel
Proceedings of International Conference on Evolution in Beam
Applications (1992) 205
24. Ogawa, M., Koganemaru, K., Nakajima, M., Makishima, A., Ishii, T. and
Ishii, M.
In-beam Gamma-ray Study of ^{104}In
Proceedings of 6th Int. Conf. on Nuclei Far from Stability,
Bernkastel-Kues, 1992, pp.655
25. Ogawa, M., Koganemaru, K., Nakajima, M., Makishima, A., Ishii, T. and
High-spin States in $^{107,105}\text{Sn}$
Proceedings of 6th Int. Conf. on Nuclei Far from Stability,
Bernkastel-Kues, 1992, pp.659

26. Ono, F., Matsumoto, N., Bang, L., Maeta, H., Jakubovics, J.P. and Haruna, K.
Ion Beam Irradiations in Amorphous Ferromagnetic Materials
Proc. 2nd International Symposium on Physics of Magnetic Materials
(International Academic Publishers, Beijing, 1992) 492
27. Oshima, M., Morikawa, T., Kusakari, H., Kobayashi, N., Sugawara, M., Zhang, Y.H., Ferragut, A., Ichikawa, S., Shinohara, N., Nagame, Y., Shibata, M., Gono, Y. and Inamura, T.
Double- γ Vibrational States in ^{168}Er and ^{192}Os
Nucl. Phys. A (1993) to be published
28. Sakata, M., Kawatsura, K., Naramoto, H., Nakai, Y., Yamazaki, Y., Komaki, K., Kuroki, K., Kanai, Y., Kambara, T., et al.
High-Resolution L-Shell Auger Spectroscopy of Mg-like Scandium produced in 89-MeV Sc^{8+} + He Collisions
Phys. Rev. A 44 (1991) 7290
29. Shimatani, N., Mitamura, T., Terasawa, M., Uchida, H., Koterazawa, K., Iwasaki, H., Sataka, M., Imai, M., Maeta, H., et al.
Lattice Disorder and Recrystallization in Ni Single Crystal Induced by Low Energy P Implantation and High Energy Ni Irradiation
Proceedings of International Conference on Evolution in Beam Applications (1992) 200
30. Shinohara, N., Ichikawa, S., Baba, S., Tsukada, K., Ohtsuki, T. and Alstad, J.
Gamma Rays of Short-lived Ruthenium Nuclides Produced in the Spontaneous Fission of ^{252}Cf
Radiochim. Acta, 56 (1992) 127
31. Sugiyama, Y., Tomita, Y., Ikezoe, H., Ideno, K., Sugimitsu, T. and Fujita, H.
Transfer Reactions for $^{16}\text{O}+^{144,152}\text{Sm}$ near the Coulomb Barrier
Proc. Riken Int. Workshop with Neutron-Rich Beams, Riken (1993)
32. Sugiyama, Y., Tomita, Y., Ikezoe, H., Yamanouchi, Y., Ideno, K., Hamada, S., et al.
Spin and Spin Alignments in Resonant $^{12}\text{C}+^{16}\text{O}$ Inelastic Scattering
Proc. of Int. Winter Meeting on Nuclear Physics at Bormio, Italy (1993)
33. Takeuchi, S.
Superconducting RF Activities at JAERI
Proc. of the 5th Workshop on RF Superconductivity, Hamburg, (August 19-23, 1991) p.76

34. Takeuchi, S., Ishii, T. and Shibata, M.
Superconducting Resonators for Heavy Ion Acceleration at JAERI
Proc. of the 5th Workshop on RF Superconductivity, Hamburg, (August
19-23, 1991) p.395
35. Takeuchi, S.
Acceleration of Heavy Ions by Superconducting Booster
Genshiryoku Kogyo 39-1 (1993) p.67
36. Watanabe, Y., Aoto, A., Kashimoto, H., Hane, H., Sakaki, H., Koyama,
Y., Koori, N., Yamanouti, Y., Sugimoto, M., Chiba, S., Fukahori, T.,
Hasegawa, K. and Mizumoto, M.
Measurement of Double Differential Charged-particle Emission Cross
Sections for Reactions Induced by 20-40 MeV Protons (II)
Proceedings of the 1992 Symposium on Nuclear Data, Nov. 26-27, 1992,
JAERI, Tokai JAERI-M 93-046 (1993), pp.297

Contributions to Scientific and Technical Meetings

1. Amornkitbanrung, V., Tomimitsu, H. and Aizawa, K.
XDT of Defects Induced by High Dose Ion-Irradiation in Si Single Crystals
Fall Meeting of Phys. Soc. Japan in Niigata (Oct. 2-5, 1992)
2. Baba, M., Ito, N., Matsuyama, S. Matsuyama, I. and Hirakawa, N.
Application of Gridded Ionization Chamber for Secondary Charged Particle Spectrum Measurement
Fall Meeting of Japan Atomic Energy Society in Nagoya (Oct. 20-23, 1992)
3. Chenevier, B., Ikeda, S., Kumakura, H., Togano, K., Okayasu, S. and Kazumata, Y.
High Resolution Electron Microscopy Study of 180MeV Cu^{11} Ion-Irradiated Crystals of $\text{Bi}_2\text{Sr}_2\text{CaCu}_2\text{O}_y$
Fall Meeting of The Japan Society of Applied Physics in Osaka (Sept. 16-19, 1992)
4. Fujita, H., Sugiyama, Y., Tomita, Y., Ikezoe, H., Ideno, K. et al.
Inelastic Scattering of $^{19}\text{F}+^{28}\text{S}$ (II)
Fall Meeting of Physical Society of Japan in Niigata (Oct. 2-5, 1992)
5. Fujita, H., Mukae, T., Hijiya, M., Nakamoto, K., Utsunomiya, K., Okamoto, T., Niiya, S., Mitsuoka, S., Sugimitsu, T., Kato, N., Morinobu, S., Sugiyama, Y., Tomita, Y., Ikezoe, H., Ideno, K. and Yamanouchi, Y.
Measurement of Spin Alignment of $^{12}\text{C}(2^+)$ State in $^{16}\text{O}+^{12}\text{C}$ Inelastic Scattering II
Spring Meeting of the Physical Society of Japan in Sendai (Mar. 29 - Apr. 1, 1993)
6. Fujita, H., Sugiyama, Y., Tomita, Y., Ikezoe, H., Ideno, K. et al.
Spin Alignment of the 2^+ , 4.44MeV State in ^{12}C in $^{16}\text{O}+^{12}\text{C}$ Inelastic Scattering
Spring Meeting of Physical Society of Japan in Sendai (Mar. 29 - Apr. 1, 1993)
7. Gono, Y., Mitarai, S., Ideguchi, E., Shizuma, T., Odawara, A., Morikawa, T., Zhang, Y.H., Ferragut, A., Morita, K., Yoshida, A., Murakami, T., Ogawa, M., Nakajima, M., Oshima, M., Kusakari, H. and Sugawara, M.
A High-spin Isomer in ^{145}Sm

- Spring Meeting of the Physical Society of Japan in Niigata
(Oct. 2-5, 1992)
8. Haruna, K. and Maeta, H.
Thermal Expansion of Synthetic Diamond Single Crystal at Low Temperatures
DIAMOND FILMS '92 3rd European Conference on Diamond, Diamond-like and Relating Coatings in Heidelberg (August 1992)
 9. Hayashi, K., Kikuchi, H., Akabori, M. and Fukuda, K.
Radiation Damage of UO_2 by Ion Implantation (I)
- 100 MeV Iodine Ion Implantation -
Fall Meeting of Atomic Energy Soc. Japan in Nagoya
(Oct. 20-22, 1992)
 10. Ikeda, Y., Chiba, S., Fukahori, T., Mizomoto, M., Hasegawa, K., Meigo, S. and Maekawa, H.
Measurement of Neutron Activation Cross Sections at an Energy Region from 9 to 13 MeV using $^1H(^{11}B, n)^{11}C$ Neutron Source
Annual Meeting of Japan Atomic Energy Association in Kyoto
(Mar. 27-29, 1993)
 11. Imai, M. and Sataka, M.
Charge Distribution of Neon Recoil Ions by Carbon Ions Impact in Coincidence with Projectile Final Charges
Fall Meeting of the Physical Society of Japan in Tokyo (September 25)
 12. Ito, N., Baba, M., Matsuyama, S., Matsuyama, I., Hirakawa, N., Chiba, S., Fukahori, T., Mizumoto, M. and Hasegawa, K.
Measurement of α -Production Cross Section of Ni and Fe using Gridded Ionization Chamber
Fall Meeting of Japan Atomic Energy Society, in Nagoya
(Oct. 20-23, 1993)
 13. Kanzaki, Y., Sekimura, N., Okada, S., Masuda, T., Arai, Y., Ishino, S., Iwata, T. and Iwase, A.
Cascade Damage in Gold by Self-Ion Irradiation
Spring Meeting of the Atomic Energy Society of Japan in Kyoto
(Mar. 31 - Apr. 2, 1993)
 14. Kasuga, R., Yamaguchi, T., Yano, D., Takahashi, N., Yokoyama, A., Baba, H. and Shinohara, N.
Fission of the $^{238}U + p$ System near the Excitation Energy 14 MeV
The 65th Spring Annual Meeting of the Chemical Society of Japan in Tokyo (Mar. 28-31, 1993)

15. Kawatsura, K., Nakae, T., Mitamura, T., Terasawa, M., Sataka, M.,
Imai, M. and Maeta, H.
PIXE and RBS Study of Radiation-Induced Segregation in Single
Crystal Austenitic Stainless Steel SUS304
The 11th Int. Conf. on Particle Induced X-Ray Emission and its
Analytical Applications in Tokyo (July 20)
16. Kazumata, Y., Okayasu, S. and Michigami, O.
Radiation Effects of High Tc Materials (II)
(September 25, 1992)
17. Kazumata, Y., Okayasu, S. and Michigami, O.
Radiation Effects of High Tc Materials (III)
Spring Meeting of Physical Society of Japan
(April 1, 1993)
18. Koganemaru, K., Ogawa, M., Nakajima, M., Ishii, T., Makishima, A. and
Ishii, M.
Lifetime and γ -ray Linear Polarization Measurement of $^{105,107}\text{Sn}$
Autumn Meeting of Physical Society of Japan in Niigata
(Oct. 2-5, 1992)
19. Kumakura, H., Chenevier, B., Kitaguchi, H., Ikeda, S., Togano, K.,
Maeda, H., Shimoyama, J., Okayasu, S. and Kazumata, Y.
Radiation Effects on c-axis Grain Oriented $\text{Bi}_2\text{Sr}_2\text{CaCu}_2\text{O}_8$ Tape
Fall Meeting of The Japan Institute of Metals in Toyama
(Oct. 6-8, 1991)
20. Kumakura, H., Kitaguchi, H., Togano, K., Maeda, H., Shimoyama, J.,
Okayasu, S. and Kazumata, Y.
Flux Pinning in Cu Ion Irradiated $\text{Bi}_2\text{Sr}_2\text{CaCu}_2\text{O}_8$
Fall Meeting of The Japan Society of Applied Physics in Osaka
(Sep. 16-19, 1992)
21. Maeta, H., Haruna, K., Bang, Lu., Aizawa, H., Ono, F. and Sugai, H.
Study of Radiation Effects on Diamond Crystals by X-ray Diffraction
Spring Meeting of Physical Society of Japan in Sendai (Mar. 31, 1992)
22. Maeta, H., Haruna, K., Bang, Lu. and Ono, F.
X-ray Diffraction Studies of Self-ion Irradiated Synthetic Diamond
Single Crystal at Low Temperatures
Eighth International Conference on ION BEAM MODIFICATION of MATERIALS
in Heidelberg (September 1992)

23. Maeta, H., Bang, Lu., Haruna, K. and Ono, F.
Study of Radiation Effects on Diamond Crystals by X-ray Diffraction
Fall Meeting of Physical Society of Japan in Tokyo (Sep. 25, 1992)
24. Magara, M., Shinohara, N., Tsukada, K., Oshima, M. and Ichikawa, S.
Decay Properties of ^{245}Cf
The 36th Symposium on Radiochemistry in Tokyo (Oct. 26-28, 1992)
25. Matsumoto, N., Bang, Lu, Maeta, H., Jakubonovics, J.P., Haruna, K.
and Ono, F.
Magnetic Properties of Ion Beam Irradiated Amorphous Ribbons
Spring Meeting of Physical Society of Japan in Sendai (Mar. 31, 1992)
26. Matsumoto, N., Bang, Lu, Maeta, H., Jakubonovics, J.P., Haruna, K.
Irradiation Induced High Permeability in Amorphous Materials II
Fall Meeting of Physical Society of Japan in Tokyo (Sep. 25, 1992)
27. Matsumoto, N., Bang, Lu., Maeta, H., Jakubonovics, J.P., Haruna, K.
and Ono, F.
Effect of Ion Beam Irradiation in Amorphous Ferromagnetic Alloys
Eighth International Conference on ION BEAM MODIFICATION of MATERIALS
in Heidelberg (September 1992)
28. Nishinaka, I., Tanikawa, M., Miyamoto, S., Sueki, K., Nakahara, H.,
Ohtsuki, T., Tsukada, K., Magara, M., Sekine, T., Hatsukawa, Y.,
Nagame, Y. and Ikezoe, H.
Nuclear Fission in $^{18}\text{O}+^{209}\text{Bi}$ Reaction
The 36th Symposium on Radiochemistry in Tokyo (Oct. 26-28, 1992)
29. Nitani, N., Yamaguchi, T., Yano, D., Takahashi, N., Saito, T.,
Yokoyama, A., Baba, H. and Shinohara, N.
Fission of the $^{238}\text{U} + p$ System in the Giant Dipole Resonance Region
The 36th Symposium on Radiochemistry in Hachioji (Oct. 26-28, 1992)
30. Ohtsuki, T., Kasagi, J., Sugawara, M., Ikezoe, H., Nagame, Y.,
Shinohara, N., Magara, M., Tsukada, K., Nishinaka, I., Tanikawa, K.
and Sueki, K.
Light Charged Particles Identification with Scintillators and
Application
The 36th Symposium on Radiochemistry in Tokyo (Oct. 26-28, 1992)
31. Oshima, M., Morikawa, T., Kusakari, H., Kobayashi, N. Sugawara, M.
Gono, Y., Zhang, Y.H. and Ferragut, A.
Search for Two-phonon States in ^{164}Dy and ^{168}Er
Spring Meeting of the Physical Society of Japan in Niigata
(Oct. 2-5, 1992)

32. Oshima, M., Morikawa, T., Kusakari, H., Kobayashi, N., Sugawara, M.
Zhang, Y.H., Ferragut, A., Ichikawa, S., Shinohara, N., Nagame, Y.,
Shibata, M., Gono, Y. and Inamura, T.
Double- γ Vibrational States in ^{168}Er and ^{192}Os
The 21st Intern. Symp. on Rapidly Rotating Nuclei in Tokyo
(Oct. 26-30, 1992)
33. Sataka, M.
Incident Ion q-dependence of Binary Peak at 0 Degree
Annual Meeting of the Society for Atomic Collision Research in Wako
(Aug. 25, 1992)
34. Sataka, M.
Binary Peak Electrons Observed at 0 degree of 2-4 MeV/u Fq^+ , Siq^+ ,
 Niq^+ Ions in Collisions with He Target
XIIth Int. Conf. on the Application of Accelerators in Research and
Industry in Denton (Nov. 4, 1992)
35. Sakata, M., Imai, M., Yamazaki, Y., Komaki, K., Kawatsura, K., Kanai,
Y. and Tawara, H.
Projectile Charge State Dependence of Binary Electrons in Heavy-ion
Collisions
Spring Meeting of the Physical Society of Japan in Sendai
(Mar. 30, 1993)
36. Sekimura, ., Masuda, N., Kanzaki, Y., Okada, S. and Ishino, S.
Cascade Damage Formation under Self-ion Irradiation
Spring Meeting of the Japan Institute of Metals in Yokohama
(Mar. 27-29, 1993)
37. Shinohara, N., Tsukada, K., Ichikawa, S., Magara, M. and Ohtsuki, T.
A Study on Heavy-ion Induced Fission of Actinides by Means of Rapid
Solvent Extraction Technique "SISAK"
205th American Chemical Society National Meeting in Denver
(Mar. 28 - Apr. 2, 1993)
38. Sugiyama, Y.
Elastic Scattering of $^{28}\text{Si}+^{58,64}\text{Ni}$ near the Coulomb Barrier
Int. Symp. on the Present and Future of Nuclear Dynamics in Seoul,
(May 15-16, 1992)
39. Sugiyama, Y.
Elastic Scattering of $^{16}\text{O}+^{16}\text{O}$ at $E=145\text{MeV}$
RCNP Symposium on Heavy-ion Interaction in RCNP (1992)

40. Sugiyama, Y.
Recent Results on Heavy-Ion Reactions at JAERI Tandem Seminar at
Hahn-Meitner Institute, Berlin, Germany (Jan. 19, 1993)
41. Sugiyama, Y.
Spins and Spin Alignments for Resonances in $^{16}\text{O}+^{12}\text{C}$ Inelastic
Scattering
Int. Winter Meeting on Nuclear Physics, Bormio, Italy
(Jan. 25-30, 1993)
42. Sugiyama, Y.
Transfer Reactions for $^{16}\text{O}+^{144,152}\text{Sm}$ near the Coulomb Barrier
Riken Int. Symp. on Heavy-Ion Reactions with Neutron-Rich Beams,
Riken (Feb. 18-20, 1993)
43. Sugiyama, Y., Tomita, Y., Ikezoe, H., Ideno, K. Yamanouchi, Y. et al.
Extended Optical Model Approach to Elastic Scattering of $^{28}\text{Si}+^{58,64}\text{Ni}$
near the Coulomb Barrier
Fall Meeting of Physical Society of Japan in Niigata (Oct. 2-5, 1992)
44. Tsukada, K., Shinohara, N., Magara, M., Ichikawa, S., Nagame, Y.,
Sueki, K., Nishinaka, I., Tanikawa, M. and Nakahara, H.
Extremely Asymmetric Mass Division Produced on Proton-Induced Fission
of Actinides (2).
The 36th Symposium on Radiochemistry in Tokyo (Oct. 26-28, 1992)
45. Yamanouti, Y., Sugiyama, Y., Tomita, Y. and Ideno, K.
Elastic and Inelastic Scattering of 115MeV ^{12}C from ^{58}Ni
Fall Meeting of the Physical Society of Japan in Niigata
(Oct. 5, 1992)
46. Yamanouti, Y., Sugiyama, Y., Tomita, Y. and Ideno, K.
Elastic and Inelastic Scattering of 115MeV ^{12}C from ^{52}Cr
Spring Meeting of the Physical Society of Japan in Sendai
(Mar. 30, 1993)
47. Yamazaki, Y., Komaki, K., Sataka, M., Imai, M., Kanai, Y., Kawatsura,
K., Tawara, H. and Schultz, D.R.
Electron Emission in Energetic Heavy Ion-Atom Collisions
The IV China-Japan Seminar and 1st East-Asian Int. Seminar
on Atomic and Molecular Physics in Tokyo (October 12)

VII. PERSONNEL AND COMMITTEES

(April 1992—March 1993)

(1) Personnel

Department of Physics

Mitsuhiko	Ishii	Deputy Director
Tatsuo	Numata	Administrative Manager
Yuuki	Kawarazaki	Principle Scientist

Accelerators Division

Scientific Staff	Chiaki	Kobayashi *
	Shiro	Kikuchi
	Suehiro	Takeuchi
	Susumu	Hanashima
	Michihiro	Shibata
Technical Staff (Tandem, V.D.G)	Tadashi	Yoshida **
	Isao	Ohuchi
	Susumu	Kanda
	Katsuzo	Horie
	Yoshihiro	Tsukihashi
	Shinichi	Abe
	Shuhei	Kanazawa

Nuclear Physics Laboratory

Scientific Staff	Akira	Iwamoto *
	Yasuharu	Sugiyama
	Yoshiaki	Tomita
	Hiroshi	Ikezoe
	Masumi	Ohshima
	Kazumi	Ideno
	Yoshimaro	Yamanouchi
	Tetsuro	Ishii
	Michiaki	Sugita
	Shingo	Hamada
	Koji	Niita

* Head

** Leader, Technical Staff

Solid State Physics Laboratory I

Scientific Staff	Yukio	Kazumata*
	Hiroshi	Naramoto
	Hiroshi	Tomimitsu
	Satoru	Okayasu
	Kazunari	Aizawa

Solid State Physics Laboratory II

Scientific Staff	Tadao	Iwata*
	Akihiro	Iwase
	Norito	Ishikawa

Nuclear Data Center

	Yasuyuki	Kikuchi*
	Satoshi	Chiba
	Tokio	Fukabori

Atomic and Molecular Physics Laboratory

Scientific Staff	Hiroshi	Maeta*
	Masao	Sataka
	Makoto	Imai

Department of Chemistry

Nuclear Chemistry Laboratory 2

Scientific Staff	Michio	Hoshi*
	Shin-ichi	Ichikawa
	Nobuo	Shinohara
	Hideki	Iimura
	Kazuaki	Tsukada

Physical Chemistry Laboratory

Scientific Staff	Mutsuhide	Komaki
	Jiro	Ishikawa

* Head

Laser Chemistry Laboratory

Scientific Staff	Shin-ichi	Ohno *
	Katsutoshi	Furukawa

Department of Radioisotopes

Isotope Research and Development Division

Scientific Staff	Yuichiro	Nagame
	Hiroyuki	Sugai
	Yuichi	Hatsukawa

Department of Fuels and Materials Research

Radiation Effects and Analysis Laboratory

Scientific Staff	Akimichi	Hishinuma *
	Takeo	Aruga
	Shozo	Hamada
	Tomotsugu	Sawai
	Katsumaro	Fukai

Material Processing and Qualification Laboratory

Scientific Staff	Kenji	Noda *
	Yoshinobu	Ishii
	Tetsuya	Nakazawa

Department of Reactor Engineering

Fusion Reactor Physics Laboratory

Scientific Staff	Hiroshi	Maekawa *
	Yujiro	Ikeda

Thermal Reactor Physics Laboratory

Scientific Staff	Tsuyoshi	Yamane
	Shinichiro	Meigo
	Kazuo	Hasegawa

* Head

Accelerator Engineering Laboratory

Scientific Staff Motoharu Mizumoto *

Department of Health Physics

Radiation Control Division II

Technical Staff	Yasunori	Harada
	Akira	Endo
	Masamitsu	Kikuchi

* Head

VIII. CO-OPERATIVE RESEARCHES

Title	Contact person Organization
1. Gamma-Ray Spectroscopy in the Neighbour Nuclei of ^{100}Sn	Masao OGAWA Tokyo Institute of Technology
2. Mass Division Processes in Fissions of Actinide Elements	Hiromichi NAKAHARA Faculty of Science, Tokyo Metropolitan University
3. Study of Nuclear Interactions in Heavy-Ion Reaction	Takao NAKAJIMA Department of Physics, Kyushu University
4. Atomic Collision Research Using Highly Charged Ions	Ken-ichiro KOMAKI Institute of Physics, College of Arts and Sciences, University of Tokyo
5. Study of Formularlism for Radiation Damage by Heavy Ion-Irradiation	Shiori ISHINO Faculty of Engineering, University of Tokyo
6. Study of Single Event Phenomenon on High Energy Heavy Ion- Irradiation	Sumio MATSUDA National Space Development Agency of Japan
7. Study of Higher-Order Effect in Nuclear Collective Motion through Coulomb Excitation	Hideshige KUSAKARI Faculty of Education, Chiba University
8. A Research for the Production of Transuranium Elements	Ichiro FUJIWARA Faculty of Economy, Otemon Gakuin University
9. Irradiation Enhanced Diffusion Process in Li_2O Irradiation with Heavy Ions	Hisayuki MATSUI Faculty of Engineering, Nagoya University

- | | |
|------------------------------------------------------------------------------------------------------------|-------------------------------------------------------------------------------------|
| 10. Radiation Damage of Materials
for Environment Resistance
Devices | Kazutoshi OHASHI
Faculty of Engineering,
Tamagawa University |
| 11. Irradiation Effect on Electrical
Property of LiAl with Li and
Other Heavy Ions | Kazuo KURIYAMA
Research Center of Ion Beam
Technology, Hosei University |
| 12. Study of Phase Transition on
Nuclear Fission Phenomenon | Hiroshi BABA
Faculty of Science,
Osaka University |
| 13. Radiation Effects of High T_c
Materials | Hiroaki KUMAKURA
National Research Institute
for Metals |
| 14. Study on Continuous Spectra
of Emitted Particles Induced
by 20-40 MeV Protons | Yukinori KANDA
Department of Energy Conversion
Engineering, Kyushu University |
| 15. Study on Total Kinetic Energy
Distributions in the Fission
Process of the Lead-Bismuth
Region | Masumi SUGAWARA
Faculty of Science
Tohoku University |

(2) Tandem Steering Committee

(Chairman)	Masashi	Iizumi	(Deputy Director General, Tokai Research Establishment)
	Toru	Hiraoka	(Director, Department of Reactor Engineering)
	Tatuo	Kondo	(Director, Department of Fuels and Materials Research)
	Mitsuhiko	Ishii	(Director, Department of Physics)
	Enzo	Tachikawa	(Director, Department of Chemistry)
	Hirokazu	Umezawa	(Director, Department of Radioisotopes)
(Secretary)	Chiaki	Kobayashi	(Head, Accelerators Division)
(Secretary)	Tatsuo	Numata	(Administrative Manager, Department of Physics)

(3) Tandem Consultative Committee

(Chairman)	Takumi	Asaoka	(Director General, Tokai Research Establishment)
(Vice Chairman)	Masashi	Iizumi	(Deputy Director General, Tokai Research Establishment)
(Vice Chairman)	Mitsuhiko	Ishii	(Director, Department of Physics)
	Hiromichi	Kamitsubo	(Director, Institute of Physical and Chemical Research)
	Koji	Nakai	(Professor, National Laboratory for High Energy Physics)
	Hiroyasu	Ejiri	(Professor, Osaka University)
	Shiori	Ishino	(Professor, University of Tokyo)
	Hiroyuki	Tawara	(Associate Professor, Institute of Plasma Physics, Nagoya University)
	Kohzoh	Masuda	(Professor, University of Tsukuba)
	Nobutsugu	Imanishi	(Professor, Kyoto University)
	Ichiro	Fujiwara	(Professor, Otomon Gakuin University)
	Akito	Takahashi	(Professor, Osaka University)
	Naohiro	Hirakawa	(Professor, Tohoku University)
	Hirosuke	Yagi	(Professor, University of Tsukuba)
	Syunpei	Morinobu	(Professor, Kyushu University)
	Hiromichi	Nakahara	(Professor, Tokyo Metropolitan University)
	Sadaei	Yamaguchi	(Professor, The Research Institute for Iron, Steel and Other Metals, Tohoku University)
(Secretary)	Nobutsugu	Imanishi	(Professor, Kyoto University)
	Mamoru	Akiyama	(Professor, University of Tokyo)
	Yasuo	Ito	(Associate Professor, University of Tokyo)
(Secretary)	Chiaki	Kobayashi	(Head, Accelerators Division)
(Secretary)	Tatsuo	Numata	(Administrative Manager, Department of Physics)
(Secretary)	Hirokazu	Umezawa	(Director, Department of Radioisotopes)

(Secretary)	Tadao	Iwata	(Head, Solid State Physics Laboratory II)
(Secretary)	Kenji	Noda	(Head, Material Processing and Qualification, Department of Fuels and Materials Research)
(Secretary)	Hiroshi	Maeta	(Head, Atomic and Molecular Physics Labotatory)

(4) Tandem Program Advisory Committee

(Chairman)	Mitsuhiko	Ishii	(Director, Department of Physics)
	Shoji	Izawa	(Chief, Radiation Control Group, Department of Health Physics)
	Kenji	Noda	(Head, Material Processing and Qualification Laboratory)
	Satoshi	Chiba	(Nuclear Data Center, Department of Physics)
	Akira	Iwamoto	(Head, Nuclear Physics Laboratory)
	Yukio	Kazumata	(Head, Solid State Physics Laboratory I)
	Toshiaki	Sekine	(Department of Radioisotopes)
(Secretary)	Chiaki	Kobayashi	(Head, Accelerators Division, Department of Physics)
(Secretary)	Shiro	Kikuchi	(Accelerators Division, Department of Physics)
(Secretary)	Tadashi	Yoshida	(Accelerators Division, Department of Physics)